MODELING AND MIGRATION OF HIBERNIA SEISMIC DATA

IRENE G. KELLY

MODELING AND MIGRATION OF HIBERNIA SEISMIC DATA

by

Irene G. Kelly

A thesis submitted to the

School of Graduate Studies

in partial fulfillment of the

requirements for the degree of

Master of Science

Department of Earth Sciences

Memorial University of Newfoundland

April 1998

Abstract

The reservoirs of the Hibernia oil field are located within the complexly faulted Hibernia rollover structure. The accurate positioning of faults and sedimentary boundaries is especially important for the successful extraction of available hydrocarbons. Seismic migration is a valuable processing tool in the accurate imaging of such complex geologic features. Frequency-wavenumber domain, phase-shift, and reverse-time poststack migrations are tested for their ability to image Hibernia seismic data. Reverse-time migration is tested as both a 2-D and 3-D migration, and offers particular advantages due to its generality and lack of dip limitations. This migration comparison is initially done using synthetic seismic data generated from 3-D finite-difference models of the Hibernia oil field. Successful finite-difference modeling requires consideration of numerical stability, grid dispersion, and available computational facilities.

Successful poststack migration requires an accurate input velocity model, and a complete inversion may be achieved by performing a velocity sensitivity analysis on the input seismic data. This analysis requires available well formation tops so that the migration layer depths may be least-squares fitted to the well tops by adjusting the velocities. This method assumes that the layers intersect the well and are easily identifiable on the seismic section. Reverse-time migrations of model data, and well lines from the Hibernia seismic data set, are optimized in this manner.

Dedication

To my family, especially my grandfather, Thomas Nolan, for always being there for me, and for reminding me that there is more to life than books.

Acknowledgments

This analysis of migration and modeling of Hibernia data would not have been possible without the help of many people, and I would like to take this opportunity to thank them for their assistance.

The Natural Sciences and Engineering Research Council (NSERC) for their funding of this project in the form of a NSERC Industrial Postgraduate Scholarship.

The Hibernia management and development corporation (HMDC) for supplying the seismic data, velocity information, modeling horizons, and for partially funding the NSERC Industrial Postgraduate Scholarship. I would particularly like to thank Denis Coutourier, Larry Sydora, John Evans, and Iain Sinclair of HMDC for their help in obtaining the above data sets.

Phillip Bording for providing access to his 3-D modeling and reverse-time migration codes, and for discussions on finite-difference modeling.

Andrew Burton for computer assistance with the Hibernia seismic data set and invaluable discussions regarding the nature of this data set.

Tony Kocurko for helping to solve the computer problems facing this project, and for providing plotting algorithms for the model data.

My supervisor, Dr. Larry Lines, for suggesting the project and providing abundant knowledge and patience throughout the course of the project.

My friends and family who encouraged me along the pathway to success.

CONTENTS

1 Introduction **12**

1.1 Outline of this study 12

1.2 Hibernia geology 14

1.3 Background geophysical information 21

2 Seismic Modeling **23**

2.1 3-D finite-difference modeling 23

2.2 Approximations to the 3-D acoustic wave equation 25

2.3 Model parameters and exploding reflector modeling 27

2.4 Stability and boundary conditions 28

2.4.1 Numerical stability 28

2.4.2 Grid dispersion 29

2.4.3 Boundary conditions 30

2.5 3-D Hibernia models 31

3 Post-stack migration of Hibernia data **44**

3.1 Poststack migration algorithms 44

3.1.1 Frequency-wavenumber domain migration 45

3.1.2 Phase-shift migration 46

3.1.3 Reverse-time migration 47

3.1.4 3-D reverse-time migration 49

3.2 Poststack migration of Hibernia model data 50

3.3 Poststack migration of Hibernia seismic data 67

4 Optimization of Poststack migration **79**

4.1 Sensitivity of poststack migration to input velocities 79

4.2 Migration optimization based on well top information 93

4.2.1 Migration optimization of Hibernia model data 95

4.2.2 Optimization of Hibernia seismic data 101

5 Discussion and conclusions **105**

5.1 Three-dimensional finite-difference modeling 105

5.2 Analysis of poststack migration for Hibernia seismic data 106

Figure List of Tables Page

Table 4.1	Velocity models containing errors for the three layer Hibernia model	82
Table 4.2	Average fractional discrepancies for crossline 30 from the 3 layer Hibernia model	86
Table 4.3	Velocity models containing errors for the seven layer Hibernia model	87
Table 4.4	Average fractional discrepancies for crossline 30 from the seven layer Hibernia model	91
Table 4.5	Poststack migration optimization results for crossline 30 from the three layer Hibernia model	97
Table 4.6	Poststack migration optimization results for crossline 30 from the seven layer Hibernia model	99
Table 4.7	Edge solution velocity parameter results	103

Figure	List of Figures	Page
Figure 1.1	Location map of the Jeanne d'Arc sub-basin	16
Figure 1.2	Location map of the Hibernia oil field	17
Figure 1.3	Lithostratigraphic column for the Jeanne d'Arc sub-basin	18
Figure 1.4	Seismic grid and well location map for the Hibernia field	22
Figure 2.1(a)	Structure map of the Base of Tertiary unconformity	33
Figure 2.1(b)	Structure map of the Petrel Member	34
Figure 2.1(c)	Structure map of the Ben Nevis Formation	35
Figure 2.1(d)	Structure map of the Avalon Formation	36
Figure 2.1(e)	Structure map of the "A" Marker Member	37
Figure 2.1(f)	Structure map of the Catalina Member	38
Figure 2.1(g)	Structure map of the Lower Hibernia zone	39
Figure 2.1(h)	Structure map of the Murre Fault	40
Figure 2.2	Three layer Hibernia model	41
Figure 2.3	Seven layer Hibernia model	42
Figure 3.1	Synthetic seismic data for inline 30 from the three layer Hibernia model	53
Figure 3.2(a)	Stolt migration of inline 30	54
Figure 3.2(b)	Phase-shift migration of inline 30	54
Figure 3.2(c)	2-D reverse-time migration of inline 30	55
Figure 3.2(d)	3-D reverse-time migration of inline 30	55
Figure 3.3	Synthetic seismic data for crossline 30 from the three layer Hibernia model	57
Figure 3.4(a)	Stolt migration of crossline 30	58
Figure 3.4(b)	Phase-shift migration of crossline 30	58
Figure 3.4(c)	2-D reverse-time migration of crossline 30	59
Figure 3.4(d)	3-D reverse-time migration of crossline 30	59
Figure 3.5	Synthetic seismic data for inline 60 from the seven layer Hibernia model	61

Figure	List of Figures	Page
Figure 3.6(a)	Stolt migration of inline 60	62
Figure 3.6(b)	Phase-shift migration of inline 60	62
Figure 3.6(c)	2-D reverse-time migration of inline 60	63
Figure 3.6(d)	3-D reverse-time migration of inline 60	63
Figure 3.7	Synthetic seismic data for crossline 60 from the seven layer Hibernia model	64
Figure 3.8(a)	Stolt migration of crossline 60	65
Figure 3.8(b)	Phase-shift migration of crossline 60	65
Figure 3.8(c)	2-D reverse-time migration of crossline 60	66
Figure 3.8(d)	3-D reverse-time migration of crossline 60	66
Figure 3.9	Location map of the migration area of interest for the 1991 Hibernia seismic data	68
Figure 3.10	Seismic data for inline 170	69
Figure 3.11(a)	Stolt migration of inline 170	69
Figure 3.11(b)	Phase-shift migration of inline 170	70
Figure 3.11(c)	2-D reverse-time migration of inline 170	70
Figure 3.12	Seismic data for crossline 210	72
Figure 3.13(a)	Stolt migration of crossline 210	72
Figure 3.13(b)	Phase-shift migration of crossline 210	73
Figure 3.13(c)	2-D reverse-time migration of crossline 210	73
Figure 3.14(a)	Seismic data for inline 100	75
Figure 3.14(b)	2-D reverse-time migration of inline 100 using coarse grid spacing	76
Figure 3.14(c)	3-D reverse-time migration of inline 100 using coarse grid spacing	76
Figure 3.15	3-D reverse-time migration of inline 100 using finer grid spacing	77
Figure 3.16(a)	2-D reverse-time migration of an inline from the 1991 seismic data	78

Figure	List of Figures	Page
Figure 3.16(b)	3-D reverse-time migration of an inline from the 1991 seismic data	78
Figure 4.1(a)	2-D reverse-time migration of crossline 30 from the 3 layer model using the correct velocity model	83
Figure 4.1(b)	2-D reverse-time migration of crossline 30 from the 3 layer model using the v1 velocity model	83
Figure 4.1(c)	2-D reverse-time migration of crossline 30 from the 3 layer model using the v2 velocity model	84
Figure 4.1(d)	2-D reverse-time migration of crossline 30 from the 3 layer model using the v3 velocity model	84
Figure 4.2(a)	2-D reverse-time migration of crossline 30 from the 7 layer model with the correct velocity model	88
Figure 4.2(b)	2-D reverse-time migration of crossline 30 from the 7 layer model with the v1 velocity model	88
Figure 4.2(c)	2-D reverse-time migration of crossline 30 from the 7 layer model with the v2 velocity model	89
Figure 4.2(d)	2-D reverse-time migration of crossline 30 from the 7 layer model with the v3 velocity model	89
Figure 4.2(e)	2-D reverse-time migration of crossline 30 from the 7 layer model with the v4 velocity model	90
Figure 4.2(f)	2-D reverse-time migration of crossline 30 from the 7 layer model with the v5 velocity model	90
Figure 4.3	Flowchart of poststack migration optimization	94
Figure 4.4(a)	2-D poststack migration result for crossline 30 from the first model with the starting velocity model	98
Figure 4.4(b)	Migration optimization result for crossline 30	98
Figure 4.5(a)	2-D poststack migration result for crossline 30 from second model with the starting velocity model	100
Figure 4.5(b)	Migration optimization result for crossline 30	100
Figure 4.6(a)	2-D poststack migration result for an inline from the 1991 seismic data using the starting velocity model	102
Figure 4.6(b)	Migration optimization result for Hibernia inline	102

Figure | List of Figures | Page

Figure 4.7 Edge solution migration optimization result for inline 30 from the first model 104

Chapter 1. Introduction

1.1. Outline of this study

The geologic features associated with petroleum reservoirs are often three-dimensional structures such as salt diapirs, reefs, deltaic sands, and over-thrusts. Typical seismic reflection acquisition parameters result in data acquired in 2-D lines over a grid in the area of interest. Seismic data processing is usually done on individual lines using the assumption that the stacked seismic section does not contain any energy from outside the plane of recording (sagittal plane). Two-dimensional migration algorithms are based upon this assumption, and use of these algorithms in complex geological areas may result in inaccurate images of the subsurface. The presence of signal from outside the plane of recording can cause 2-D migrated sections to mistie in areas of common signal. This leads to the requirement of 3-D migration for detailed subsurface imaging in complex geologic areas. This concept was initially presented by French (1974) who determined that 3-D migration of processed reflection data over 3-D models eliminates many of the correlation uncertainties caused by sideswipes and blind structures.

The geologic area of interest for this project is the Hibernia oil field, which is located in the western sector of the Jeanne d'Arc sub-basin in the northern Grand Banks region of offshore Newfoundland. The primary feature of the Hibernia field is a north-northeast trending rollover anticline which is bounded by a series of promi-

nent faults. Hydrocarbon accumulations occur mainly in stacked sequences of Lower Cretaceous sediments. Subsequent salt diapirism has deformed the rollover structure. and complex transverse fault patterns divide it into a number of separate fault blocks (Benteau and Sheppard. 1982).

Reservoir characterization of the Hibernia field requires an accurate knowledge of the sedimentary boundaries and fault locations which are primary controls on the distribution of hydrocarbons throughout the field. Seismic depth migration is a valuable processing tool in the task of accurately imaging these features. The focus of this research was to determine the relative merits of 2-D and 3-D poststack migration techniques in imaging the Hibernia field. This involved a comparison of different time and depth poststack migrations using both 2-D and 3-D algorithms. The dependence of accurate subsurface imaging on seismic velocity estimates was also resolved. Velocity sensitivity analysis was performed by optimizing 2-D reverse-time migration results through a least-squares inversion fitting of the layer depths to formation tops (Lines. 1993b). Initially. the approach to this research involved creating a computer model representative of the Hibernia geology which was then used to construct synthetic seismic data sets. A three layer and a seven layer model were created which enabled any 3-D effects introduced by the structure and faulting of the Hibernia field to be determined. The results of Wu et al. (1996) seem to indicate the superiority of 3-D migration in imaging the Hibernia data set. This research project confirmed those results through the use of model data where the true positions of subsurface reflectors were known. The migration comparisons using

synthetic seismic data provided insight as to the best migration techniques to use on the Hibernia seismic data that has been provided by the Hibernia Management and Development Company (HMDC).

The migration algorithms used in this project include frequency-wavenumber time migration (Stolt, 1978), and phase-shift (Gazdag, 1978) and reverse-time (McMechan (1983) and Baysal et al. (1983)) depth migrations. The time migration is computationally faster than the depth migrations, but is not appropriate in areas of significant lateral velocity variations. The migration algorithm of choice for this project is reverse-time migration as described by McMechan (1983), Baysal et al. (1983), and Chang and McMechan (1989). This technique is preferred over other algorithms due to its generality and lack of dip limitations. Reverse-time migration uses finite-difference solutions to the wave equation, and has previously been used on Hibernia data (Lines et al. (1995) and Wu et al. (1996)) with appreciable success. As well, Mufti et al. (1996) have made convincing use of 3-D poststack reverse-time migration in the imaging of Gulf Coast data.

1.2. Hibernia geology

The Grand Banks is the name given to the broad continental shelf that extends more than 450 km seaward from Newfoundland. This region contains a geologic record of approximately 225 m.y. of basin formation and subsidence. The largest basin in this region is the East Newfoundland basin which covers an area of 155,400 sq. km. The Bonavista platform forms the western boundary of the basin, while the Flemish

cap and Orphan Knoll are the eastern boundaries. The Cartwright (Belle Isle) arch bounds the northern edge, and the Avalon uplift is to the south. The southwestern extension of the East Newfoundland basin is called the Jeanne d'Arc sub-basin. Figure 1.1 displays the location of the Jeanne d'Arc sub-basin. This northward plunging sub-basin narrows from a 100 km width in the north to a 42 km width in the south. The Hibernia oil field is located within this sub-basin, approximately 315 km east southeast of St. John's, Newfoundland. Figure 1.2 is a location map showing the position of the field.

Von der Dick and Meloche (1986) interpret the homogeneous composition of the Hibernia oils, regardless of stratigraphic occurrence, as representing a locally derived source and fault-controlled migration. An understanding of the geologic events leading to the emplacement of hydrocarbons within the Hibernia field must therefore begin with a consideration of the geologic history of the region. Figure 1.3 is a stratigraphic column showing the geologic relationships for the Hibernia field.

Rifting of the Grand Banks region began during the late Triassic in response to periodic extensional forces (Hurley et al., 1992). The breakup at the end of the first rift cycle occurred 180 m.y. ago, with seafloor spreading being initiated between Africa and North America (C-NOPB, 1992). Fault growth occurred during the deposition of the clastic/evaporite dominated synrift sediments of the Eurydice, Argo, and Iroquois formations. Thermal subsidence occurred during the deposition of the carbonate/shale dominated postrift sediments of the Downing, Voyager, and Rankin formations. The onset of the second rifting cycle occurred 140 m.y. ago in

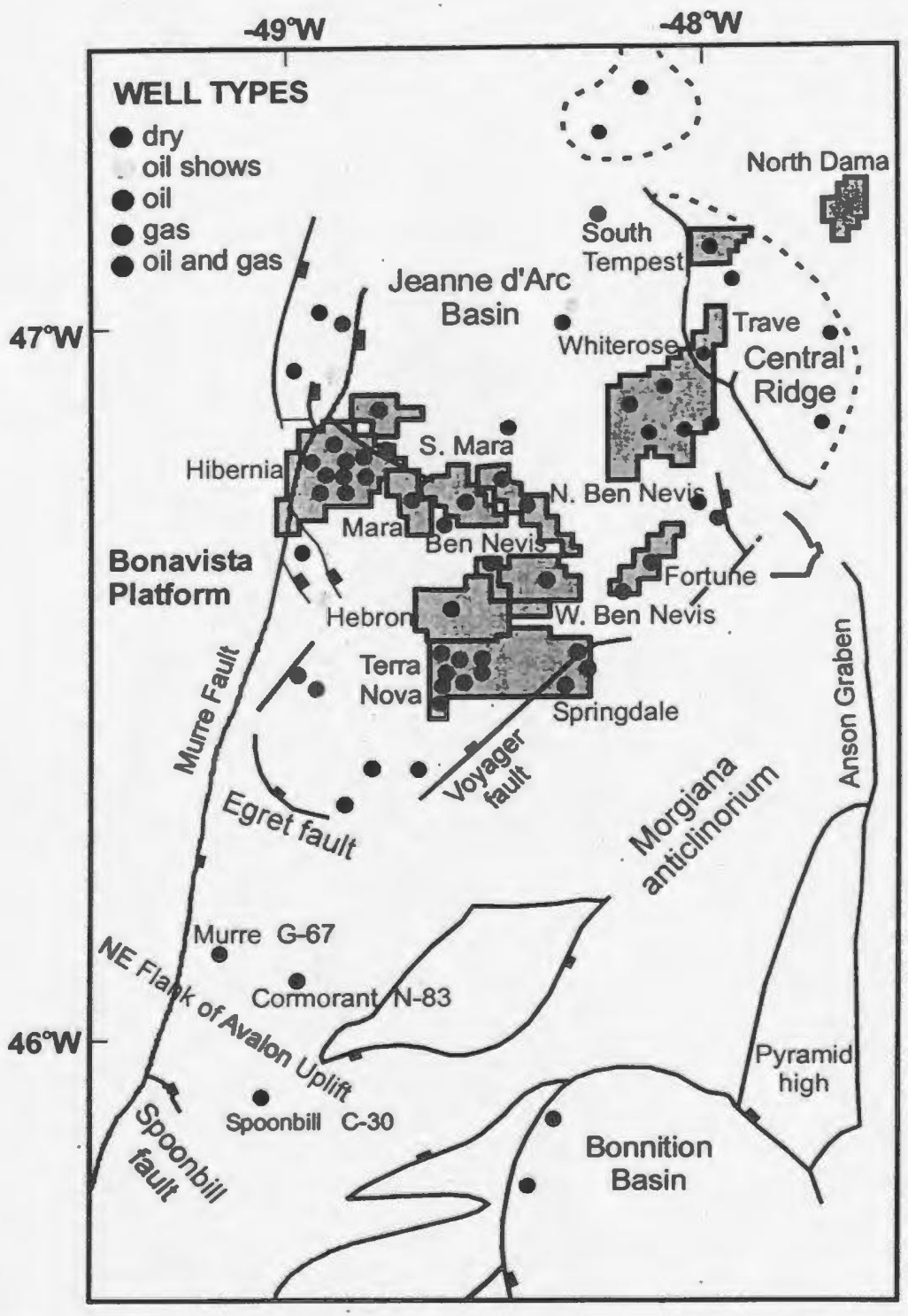

Figure 1.1 shows the location of the Hibernia field in the Jeanne d'Arc sub-basin. The listric, normal Murre fault passes through the western portion of the field, and extends beneath it at depth. (figure from Sinclair, 1994)

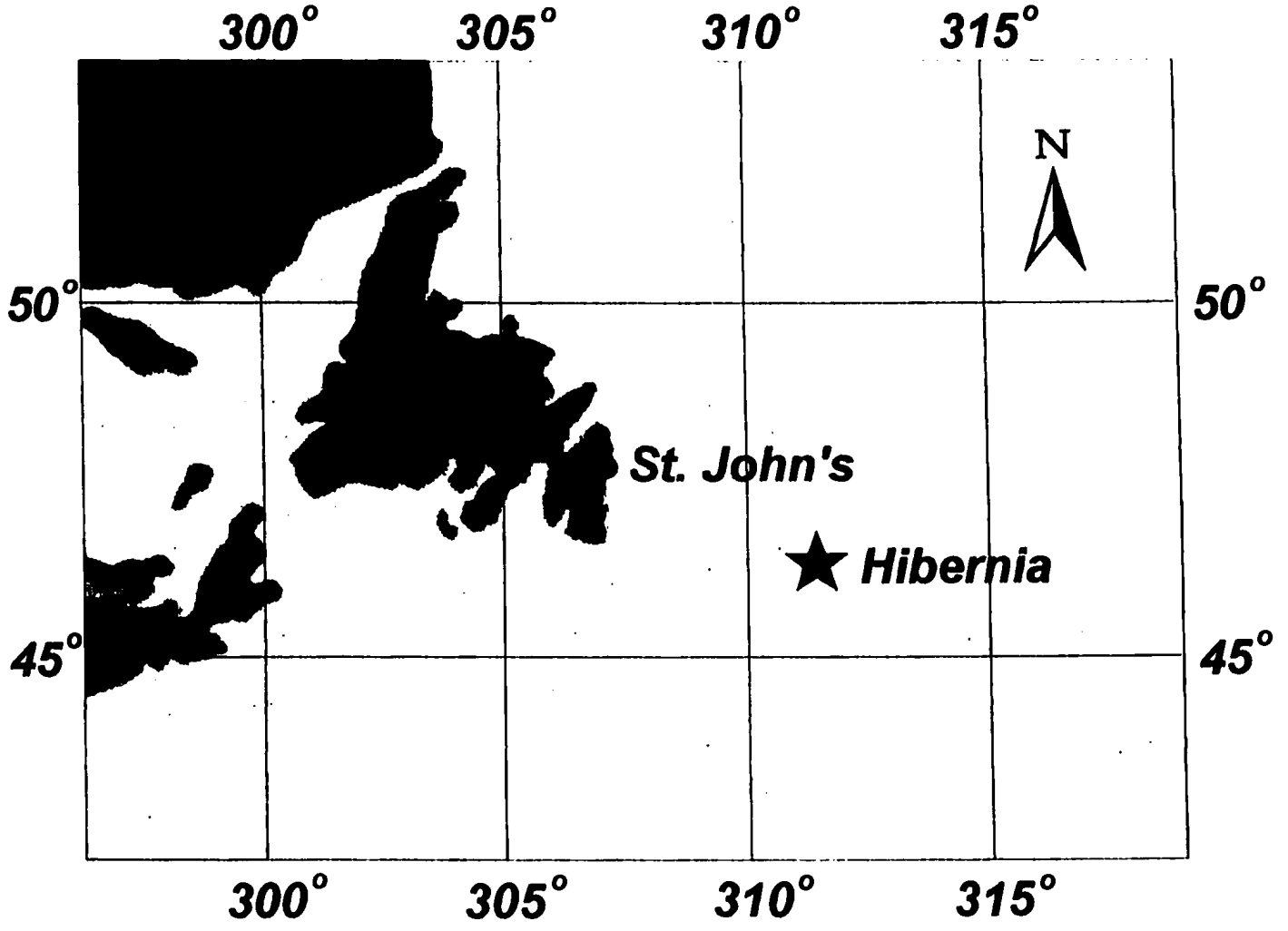

Figure 1.2 shows the location of the Hibernia oil field, approximately 315 km east-southeast of St. John's, Newfoundland. (figure adapted from Lines et al, 1995)

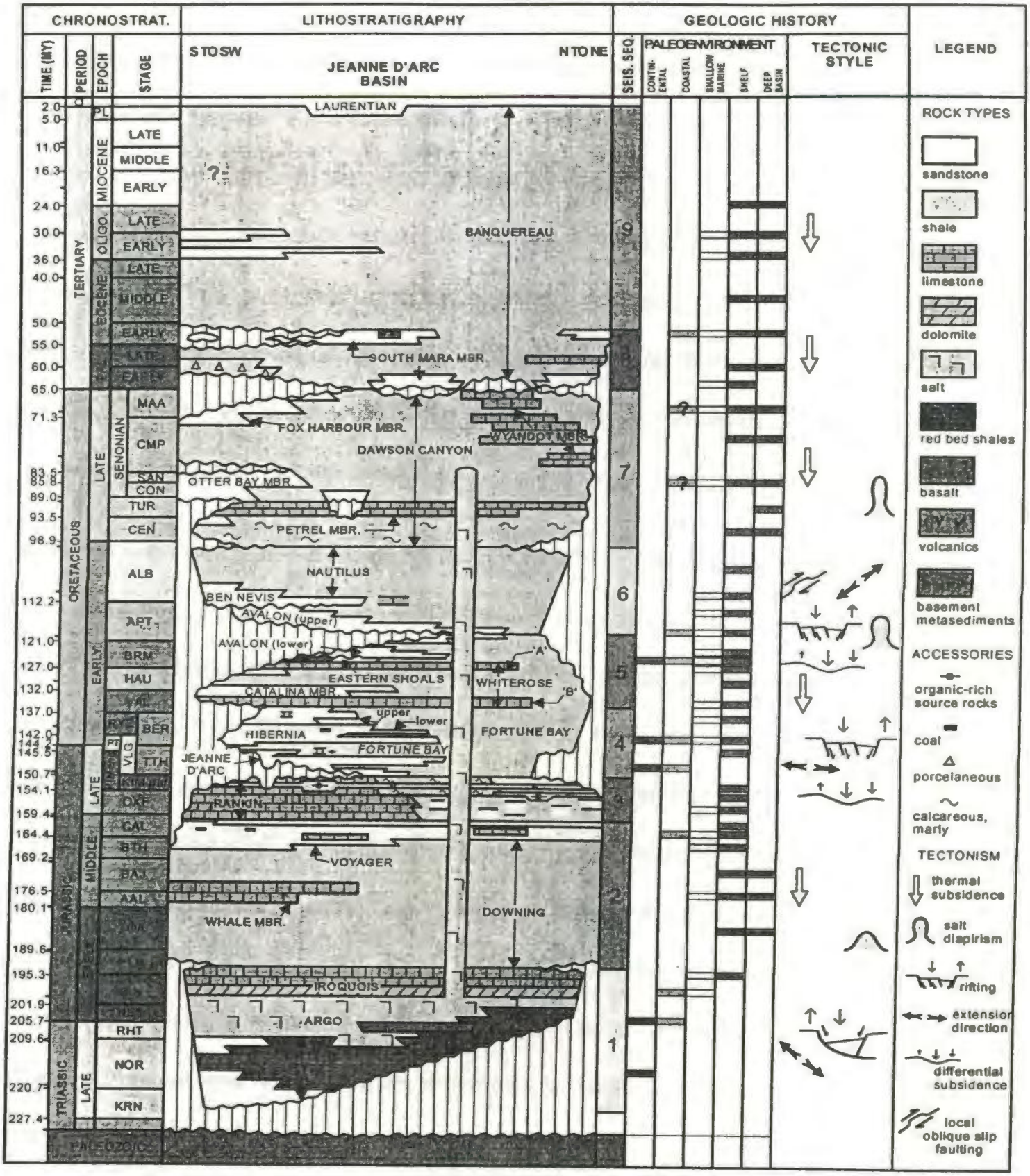

Figure 1.3. Lithostratigraphic section from Sinclair (1994) of the Jeanne d'Arc basin.

conjunction with renewed extension between Europe and North America (C-NOPB. 1992). Clastic dominated deposition of the synrift sediments resulted in the Jeanne d'Arc. Fortune Bay, and Hibernia formations. Thermal subsidence occurred during the deposition of the carbonate/shale postrift sediments of the Whiterose formation. The breakup at the end of the third rifting cycle occurred 100 m.y. ago, after deposition of the clastic dominated synrift sediments of the Ben Nevis and Nautilus formations, and the carbonate/shale dominated postrift sediments of the Dawson Canyon and Banquereau formations (C-NOPB. 1992).

Basement fracture and extension, and the resulting halokinesis of the evaporite deposits of the Argo formation, produced the variety of structural traps present in the Jeanne d'Arc sub-basin (Tankard and Welsink, 1987). The source rock for the field has been determined by Creaney and Allison (1987) to be the Egret Member shale. This unit is Kimmeridgian in age and exceeds 200 m in thickness in the central part of the sub-basin. Thermal maturation of this unit resulted from burial due to the deposition of sediments during the final passive subsidence phase in the sub-basin's history (Bell and Campbell, 1990). The hydrocarbons migrated into the available structural traps during the late Cretaceous and Tertiary, with the complex patterns of faulting providing one of the major structural controls on the migration process (von der Dick and Meloche, 1986).

There are four sandstone reservoirs within the Hibernia field. The uppermost reservoir is the Avalon Formation, which is defined as lying below the Petrel Member limestone and above the "A" marker Member carbonate. Avalon sands are inter-

preted as being shallow marine shoreface sandstones that were deposited adjacent to Lower Cretaceous deltaic systems (Benteau and Sheppard, 1982). The gross thickness is variable ranging from 16 m in the Mobil et al. Hibernia B-08 well to an anomalously thick sequence in the Mobil et al. Hibernia G-55 well. The average depth of the unit is -2345 m subsea, and it is primarily an oil reservoir. The Catalina Member is the next deepest reservoir, lying stratigraphically beneath the Avalon zone and directly overlying the "B" marker Member carbonate which is locally arenaceous. This reservoir consists of at least two discrete calcareous sand units, separated by a shale horizon (Benteau and Sheppard, 1982). The Catalina sands are dominantly composed of shallow marine shoreface sandstones to deeper offshore-to-shoreface transition sandstones (Sinclair, 1994). This zone is severely faulted, and is primarily an oil reservoir.

The Hibernia zone is the primary reservoir for the field and is expected to contain 85 percent of the recoverable hydrocarbons. The unit is divided into three major layers, with layers two and three separated by the Medial Shale. The Hibernia Formation contains several distinct sand packages, each separated by shale barriers, and consisting predominantly of fluvial channel facies (Benteau and Sheppard, 1982). The average depth of the Hibernia sands is 3700 m subsea, with several major faults totally offsetting the main reservoir segment. The deepest reservoir is the Jeanne d'Arc zone, which is located stratigraphically beneath the Hibernia sands. This oil reservoir is in the Lower Cretaceous/Upper Jurassic transition zone.

1.3. Background geophysical information

The Hibernia field was discovered in 1979 with the drilling of the P-15 discovery well by Chevron Canada Resources and Petro-Canada. The field was then delineated and appraised through the drilling of nine additional wells. Eight of the nine wells encountered oil. All ten of the wells penetrated the Avalon reservoir, with drill depths to the top of the interval ranging from 2048 m to 2342 m subsea. Seven of the wells penetrated the Hibernia sandstone, with drill depths to the top of the interval ranging from 3477 m to 3913 m subsea.

Exploration activity has resulted in hundreds of thousands of kilometres of seismic reflection data, including a 3-D survey over the field in the spring - early autumn of 1991. This survey was 21 by 28 km in size, and was completed to ensure that seismic data for the field was obtained with the latest technology before emplacement of the development platform. The record length of the seismic data set was 6 s with a 2 ms sampling rate. The data were thirty fold with a 25 m cmp spacing. Figure 1.4 is a plot of the well locations and the seismic grid for the data obtained in the 1991 survey. The Hibernia Management and Development Corporation has provided depth coordinates for several of the Hibernia geologic horizons. This information was obtained by outputting the picks from the appropriate seismic horizons as they were interpreted on a workstation. This information will serve as the basis for creating the horizon depths in the computer models of the Hibernia field. As well, average velocity and interval velocity data are available from the checkshot surveys that were conducted on the wells within the field.

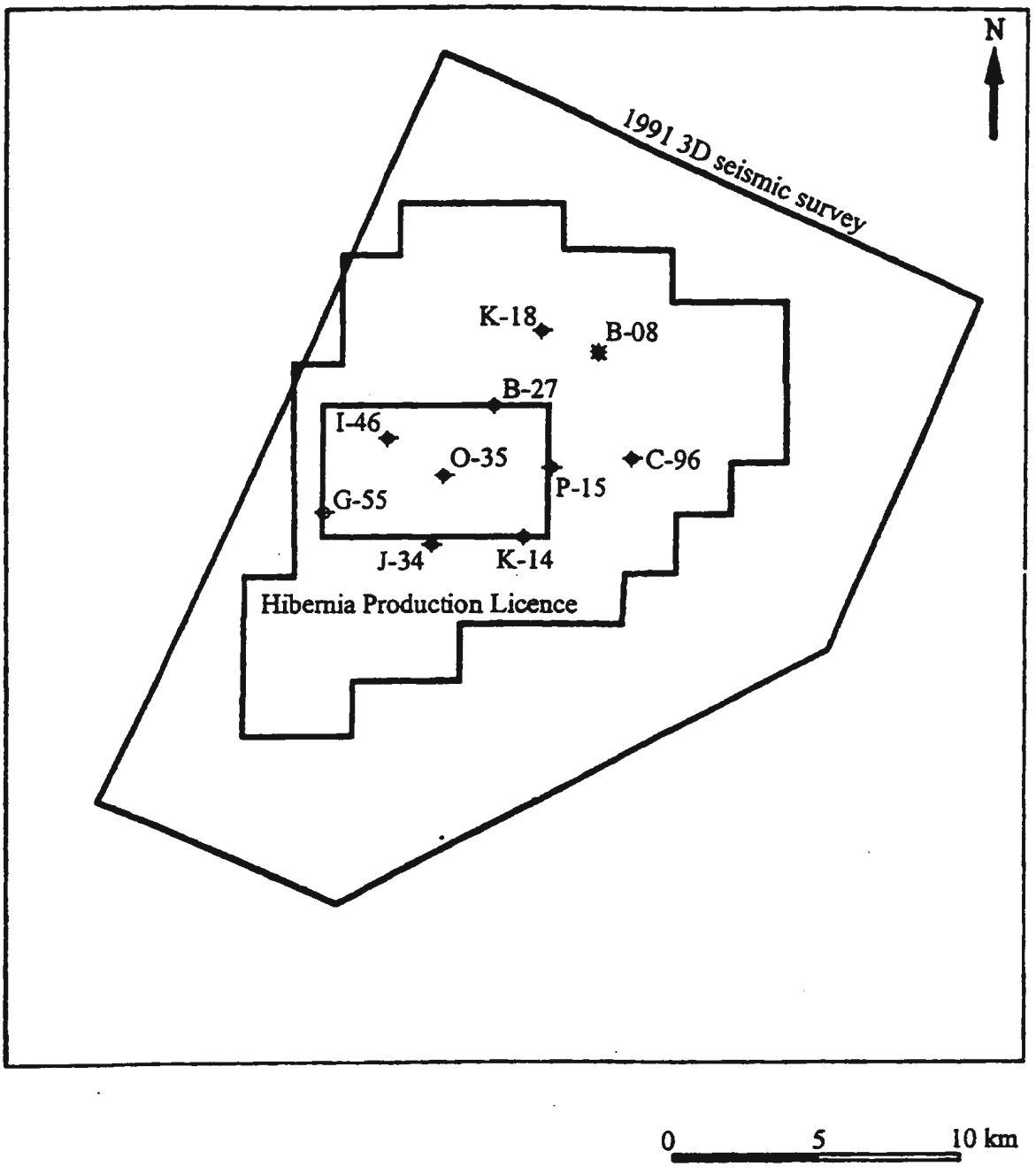

Figure 1.4 shows the well locations and the extent of the 1991 3-D seismic survey for the Hibernia field. This figure has been adapted from one provided by the Hibernia Management and Development Company.

Chapter 2. Seismic Modeling

2.1. 3-D finite-difference modeling

The generation of synthetic seismic data requires the propagation of waves through a specific reflectivity model that is associated with a certain velocity-depth arrangement. Modeling techniques may be based upon ray theory approximations or computed using the 2-D or 3-D wave equations. Ray theory approximations are the most obvious and efficient method of modeling seismic data, but such methods are based upon the assumption that all geometric dimensions in the model are large with respect to the wavelength of the incident wave (Kelly et al., 1982). This assumption results in the method being unable to provide necessary information such as diffractions and interference patterns that result from rapid changes in the curvature of geological features. Two-dimensional models based on the wave equation often yield incorrect arrival times in a structurally complex environment, and they do not incorporate out-of-plane events into their solutions. As well, a 2-D model must be excited by a line source which leads to different amplitudes than those in the real data commonly generated from a point source (Mufti and Fou, 1989).

The best choice to model 3-D features such as the Hibernia rollover structure would be 3-D models based upon the 3-D acoustic wave equation

$$\frac{\partial^2 u}{\partial x^2} + \frac{\partial^2 u}{\partial y^2} + \frac{\partial^2 u}{\partial z^2} = \frac{1}{v(x,y,z)^2}\frac{\partial^2 u}{\partial t^2} \tag{2.1}$$

where $u(x, y, z, t)$ is the wavefield and $v(x, y, z)$ is the velocity of the medium. This equation may be approximated for the purposes of mathematical modeling using finite-difference methods. Diffractions, interference phenomena, and the generation of multiple reflections are accounted for in the finite-difference modeling technique (Myczkowski et al. 1991), and the acoustic wave equation is appropriate for situations where the generation of accurate traveltimes is the primary goal (Yilmaz, 1988). The basic strategy in producing useful 3-D models requires diminishing the computational work while maintaining accuracy. Computational efficiency may be obtained using the theory of exploding reflectors (Loewenthal et al., 1976), and thereby eliminating the need to evaluate the wavefield at individual shot locations (Mufti, 1990).

The velocity-depth model required for finite-difference algorithms is based upon dividing the area of interest into a large number of blocks, with the velocity of the medium defined for each block. Lateral and vertical variations in velocity are permitted since the velocity must be defined at every grid point within the three-dimensional model cube. Layer boundaries are thus defined by the surface that is created between differing velocities. The intrinsic anisotropy of the layers is assumed to be zero. In most applications, the earth is assumed to behave like an acoustic medium in which differences in density are ignored. The heterogeneous wave equation formulation described by Kelly et al. (1982) may be used if density variations are desired in the seismic model.

There are several advantages associated with the modeling of a particular geological area. Model studies may aid in the planning of data acquisition parameters

and processing techniques for future field work, and may facilitate the interpretation of the existing seismic data for the area. Model data may aid in velocity analysis and amplitude variation studies, and help lead to a better understanding of wave propagation phenomena.

2.2. Approximations to the 3-D acoustic wave equation

The 3-D acoustic wave equation may be approximated using Taylor series in a central explicit finite-difference relation. The second-order partial derivatives in the wave equation may be expressed in terms of the value of the wavefield at neighboring grid points (Abramowitz and Stegun, 1965: p.884). The number of neighboring grid points to involve in the calculation is determined by the order of spatial and temporal sampling that is chosen for the finite-difference relation. The computational resources needed for finer spatial sampling increase geometrically, while the resources needed for finer temporal sampling increase only linearly (Alford et al., 1974). Higher-order differencing allows a reduction in the necessary computer memory, which is especially important in large scale 3-D problems. Alford et al. (1974), Dablain (1986), and Mufti (1990) recommend a differencing scheme which is second-order in time and fourth-order in space. For each new time step, the value of the wavefield is determined from the previous values. Appendix A contains a derivation of this central finite-difference relation which uses the indices i, j, k, and n (Wu et al., 1996). If the grid spacing is assumed to be equal in all three dimensions, then:

$$x = (i-1)h \qquad i = 1.2.\ldots.I \tag{2.2}$$

$$y = (j-1)h \qquad j = 1.2.\ldots.J$$

$$z = (k-1)h \qquad k = 1.2.\ldots.K$$

$$t = (n-1)\Delta t \qquad n = 1.2.\ldots.N$$

$$\begin{aligned} u^{n+1}_{i.j.k} &= \frac{v(i.j.k)^2\Delta t^2}{12h^2}\Big[16(u^n_{i+1.j.k} + u^n_{i.j+1.k} + u^n_{i.j.k+1} + u^n_{i-1.j.k} + u^n_{i.j-1.k} \\ &+ u^n_{i.j.k-1}) - (u^n_{i+2.j.k} + u^n_{i.j+2.k} + u^n_{i.j.k+2} + u^n_{i-2.j.k} + u^n_{i.j-2.k} \\ &+ u^n_{i.j.k-2}) - 90u^n_{i.j.k}\Big] - u^{n-1}_{i.j.k} + 2u^n_{i.j.k} \end{aligned} \tag{2.3}$$

In equation (2.3), $u^n_{i.j.k}$ represents the discrete value of the wavefield at time n and grid point $(i.j.k)$. This finite-difference relation uses wavefield information from grid points that are two samples away in all of the three directions. If the grid spacing in the z-direction is different than the spacing in the x- and y-directions, then equation (2.3) may be rewritten as follows (Bording, 1995):

$$\begin{aligned} u^{n+1}_{i.j.k} &= \frac{v(i.j.k)^2\Delta t^2}{12h_x^2}\Big[16(u^n_{i+1.j.k} + u^n_{i-1.j.k}) - (u^n_{i+2.j.k} + u^n_{i-2.j.k}) + \\ &16(u^n_{i.j+1.k} + u^n_{i.j-1.k}) - (u^n_{i.j+2.k} + u^n_{i.j-2.k}) + \frac{16}{R^2}\left(u^n_{i.j.k+1} + u^n_{i.j.k-1}\right) \\ &- (u^n_{i.j.k+2} + u^n_{i.j.k-2})\Big] + \left[2 - \left(\frac{v(i.j.k)^2\Delta t^2}{12h_x^2}\left(60 + \frac{30}{R^2}\right)\right)\right] u^n_{i.j.k} \\ &- u^{n-1}_{i.j.k} \end{aligned} \tag{2.4}$$

$$R = \frac{z\ gridspacing}{x.y\ gridspacing} = \frac{h_z}{h_x} \tag{2.5}$$

Equations (2.3) and (2.4) are valid for $3 \leq i \leq I-2$, $3 \leq j \leq J-2$, and $3 \leq k \leq K-2$. The advantage of using equation (2.4) lies in the fact that a coarser grid spacing may be used in the x- and y-directions. The coarser sampling in the x- and y- directions is justified in the commonly occurring case in which seismic waves travel predominantly in the vertical direction. This allows a reduction in the number of grid points needed to define the model and satisfy stability conditions.

2.3. Model parameters and exploding reflector modeling

The geological model is a simplified representation of a naturally occurring structure. As such, the structure is modeled as a lesser number of layers, and averages of the interval velocities are used. It is necessary to specify several parameters to create synthetic seismic data, including the maximum frequency of the wavelet, the time length of the records, and the time sampling interval. The maximum frequency of the wavelet must be chosen with some care as this will control the overall resolution of the data (Baysal, 1982). It is also necessary to choose a total size for the model in the x, y, and z directions, and to choose a grid spacing for each of these directions. The grid spacing may be the same for all three directions, or may vary. However, the values chosen for both the temporal and spatial sampling must satisfy both dispersion and stability criteria, as is discussed in the next section. Appropriate boundary conditions, as discussed in section 2.4.3, are also necessary to avoid reflections from the sides and base of the model.

Seismic sections may be evaluated much more efficiently using the method of ex-

ploding reflectors (Mufti. 1990). This technique involves placing a source at every grid point which occurs on a subsurface interface, and exciting them all simultaneously. The data are recorded along the level $z = 0$ which acts as the surface of the earth. Only the computation of the upgoing wavefield is required in exploding reflector modeling, which may be accomplished using half the layer velocity (Claerbout. 1985: p.2). The wave equation may therefore be rewritten in terms of this half-velocity.

$$\frac{\partial^2 u}{\partial x^2} + \frac{\partial^2 u}{\partial y^2} + \frac{\partial^2 u}{\partial z^2} = \frac{4}{v(x,y,z)^2} \frac{\partial^2 u}{\partial t^2} \tag{2.6}$$

The seismic section obtained in this manner approximates the stacked section without the need to compute individual shot records. One major difference between the stacked section and the data created through exploding reflector modeling lies in the fact that the loss of energy attributed to spreading wavefronts is only computed for one-way wave propagation (Mufti. 1990). The one-way wave propagation model also leads to incorrect arrival times for multiples on the exploding reflector data.

2.4. Stability and boundary conditions

The generation of synthetic seismic data using finite-difference relations is subject to certain conditions in order to maintain numerical stability. Grid dispersion, and unwanted reflections from the sides and base of the model, must also be avoided.

2.4.1. Numerical stability

The finite-difference relation given in equation (2.4) is stable if the difference between the theoretical and numerical solutions remains bounded as n increases for

fixed Δt and all i, j, and k (Mitchell, 1969, p.34). In order for a three-dimensional fourth-order finite-difference relation such as equation (2.4) to be numerically stable, the following relation must be satisfied (pers. comm., L. Lines, 1997) :

$$\frac{v_{max}\Delta t}{h_z} \leq \sqrt{\frac{\sum |time\ weights|}{\sum_{i=1}^{n} \left(\sum |spatial\ weights|\right)}} \tag{2.7}$$

In this equation, n is the number of spatial directions, v_{max} is the maximum velocity present in the model, Δt is the time sampling interval, and h_z is the grid spacing in the z-direction (Lines (1997), pers. comm.). The time weights and spatial weights refer to the numerical coefficients found in the derivation of a finite-difference relation for the second-order partial derivatives with respect to x, y, z and t . These values may also be obtained from mathematical handbooks such as Abramowitz and Stegun (1965), and consist of 1, -2 and 1 for the second-order time weights, and $\frac{-1}{12}$, $\frac{16}{12}$, $\frac{-30}{12}$, $\frac{16}{12}$, and $\frac{-1}{12}$ for the fourth-order spatial weights. This stability relation determines the maximum value of Δt for a given set of model parameters.

2.4.2. Grid dispersion

Grid dispersion is a phenomenon which must be taken into consideration whenever a continuous medium is approximated by a finite grid. In the case of seismic modeling, the calculated seismic responses are dispersed if the grid sampling interval is made too coarse. Grid dispersion causes the phase speed to become a function of the sampling interval, and different frequencies therefore travel at different speeds through the grid (Alford et al., 1974). In order to limit the effects of grid dispersion, the number of grid points per wavelength must be chosen based on the following relation:

$$h \leq \frac{v_{min}}{w f_{max}} \tag{2.8}$$

In this equation, h is the maximum allowed grid spacing, v_{min} is the minimum velocity present in the model, w is the number of grid points per wavelength, and f_{max} is the maximum frequency content present in the data. Alford et al. (1974) recommend 5 or more grid points per wavelength for a 2-D fourth-order finite difference scheme. Mufti et al. (1996) use 3.5 grid points per wavelength for a 3-D fourth-order finite difference scheme.

In equation (2.8) the maximum frequency content controls the temporal variations of the seismic field, which change much faster in the vertical direction than in the horizontal direction (Mufti et al., 1996). The grid spacing determined by this dispersion condition must therefore necessarily apply to vertical wavelengths, but some leniency is allowed for the grid spacing in the horizontal plane which may be taken to be twice the size of h_z without noticeable deleterious effects to the quality of the seismogram. This action assumes that the reflected seismic energy is predominantly traveling in the vertical direction, and the horizontal wavelengths are therefore much greater than the vertical wavelengths.

2.4.3. Boundary conditions

The finite capacity of computers necessitates the introduction of side and bottom boundaries to computer models used for wave propagation problems. In order to avoid reflections from these model boundaries, it is necessary to introduce boundary

conditions at the sides and base of the model. Methods of avoiding these unwanted reflections have been proposed by Clayton and Enquist (1977), Reynolds (1978), and Keys (1985). Clayton and Enquist (1977) introduce absorbing boundary conditions based on paraxial approximations of the acoustic wave equation, while Keys (1985) develops absorbing boundary conditions which eliminate reflections based on their direction of propagation. Reynolds (1978) proposes reducing edge reflections by developing boundary conditions based on reflection coefficient analysis. Another approach to reducing edge reflections involves placing a numerical damping zone, or "sponge", in the region near the boundary which will decrease the wave strength in this area (Bording, 1995). It is this damping zone method which is used to reduce the strength of boundary reflections when generating synthetic seismic data for this project.

2.5. 3-D Hibernia models

The finite memory capacity of computers, in conjunction with the computation time required for finite-difference modeling, meant that only a small portion of the area covered by the 1991 Hibernia seismic survey could actually be used to generate synthetic seismic data. The model area was chosen based on the availability of well data in this region, and the fact that this area of the Hibernia field is where the Avalon reservoir is concentrated. The rectangular area outlined in figure 1.4 shows the location of the model area relative to the 1991 seismic survey. The model area is 7420 m in extent in the east-west direction, and extends to 5460 m in the north-

south direction. Depth information was provided by the Hibernia Management and Development Corporation for seven horizons within the field. and also for the major basin-bounding fault (the Murre fault). The depth information was provided for the Base of Tertiary unconformity. Petrel Member (a strong seismic marker throughout the field). Ekt3 horizon (the base of the Ben Nevis Formation). Aan7 horizon (base of the Lower Avalon). Am2 horizon (top of the A-marker Member limestones) . Catalina Member. top of the Lower Hibernia zone. and the Murre fault. The relative locations of these horizons may be seen by referring back to the lithostratigraphy section in figure 1.3. Figures 2.1(a) to 2.1(h) contain plots of the structure of the various horizons. The regional dip on the Base Tertiary unconformity and Petrel Member is to the northeast . and the deepest area for the other Early Cretaceous horizons is to the southwest. Figures 2.2 and 2.3 are plots showing the front. top. and side view of a cube for a three layer Hibernia model and a seven layer Hibernia model. Synthetic seismic data sets were generated from both of these models using a 3-D fourth-order explicit finite-difference modeling algorithm. The velocities between the different layers were obtained using the checkshot information for wells in the area to calculate average velocities between the horizons. The minimum velocity in the 3 layer Hibernia model was 2221 m/s and the maximum velocity was 5500 m/s. The minimum velocity in the 7 layer Hibernia model was 2035 m/s and the maximum velocity was 5500 m/s. The maximum frequency generated in the modeling algorithm was 30 Hz and w is set to 3.5 for a 3-D model. Substituting these values. along with the minimum velocity. into equation 2.8 results in $h_z \leq 9.69$ m. The actual value

Base of Tertiary Unconformity

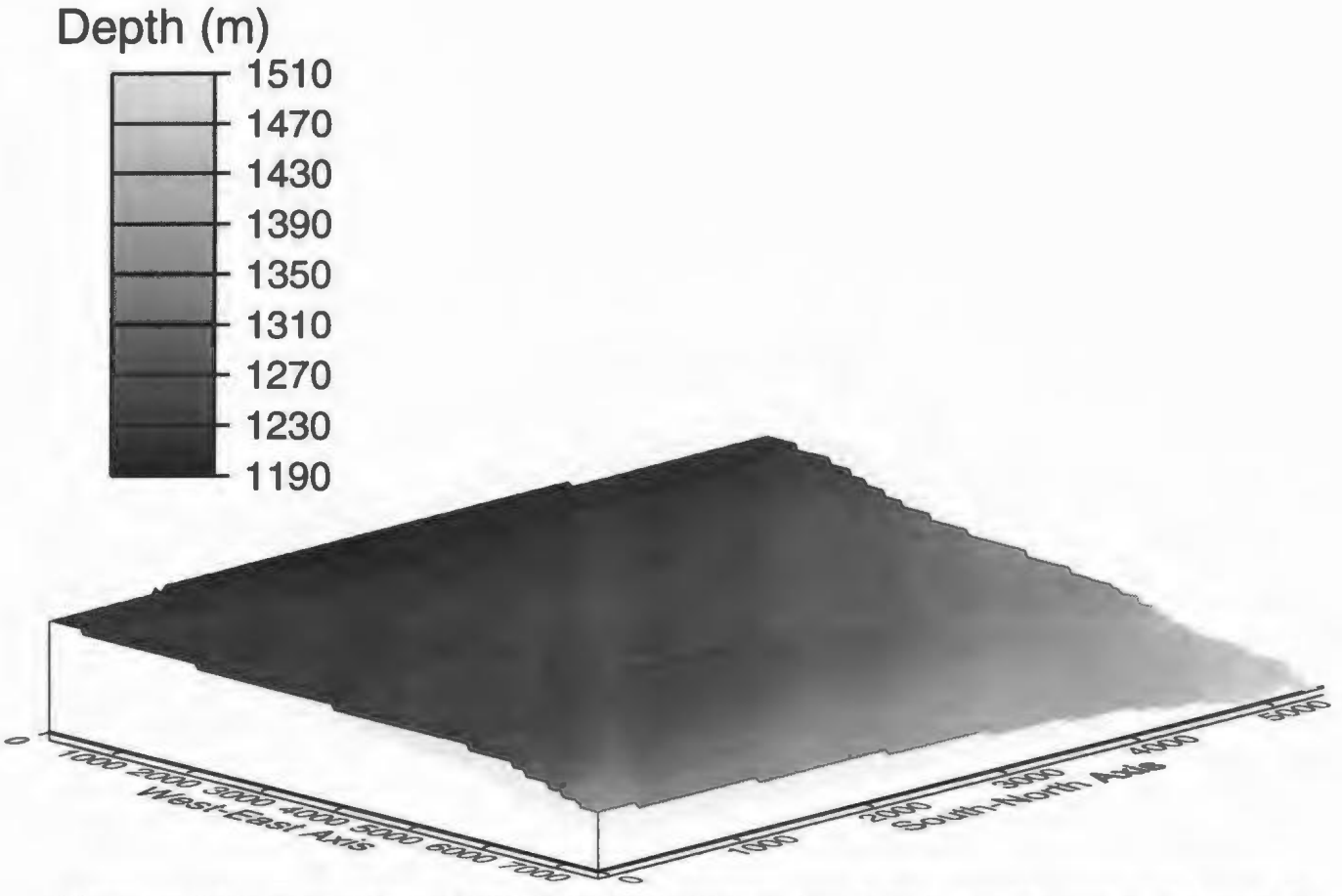

Figure 2.1(a). The Base Tertiary unconformity has a minimum depth of 1200 m below sea level and a maximum depth of 1500 m below sea level, and dips to the northeast.

Petrel Member

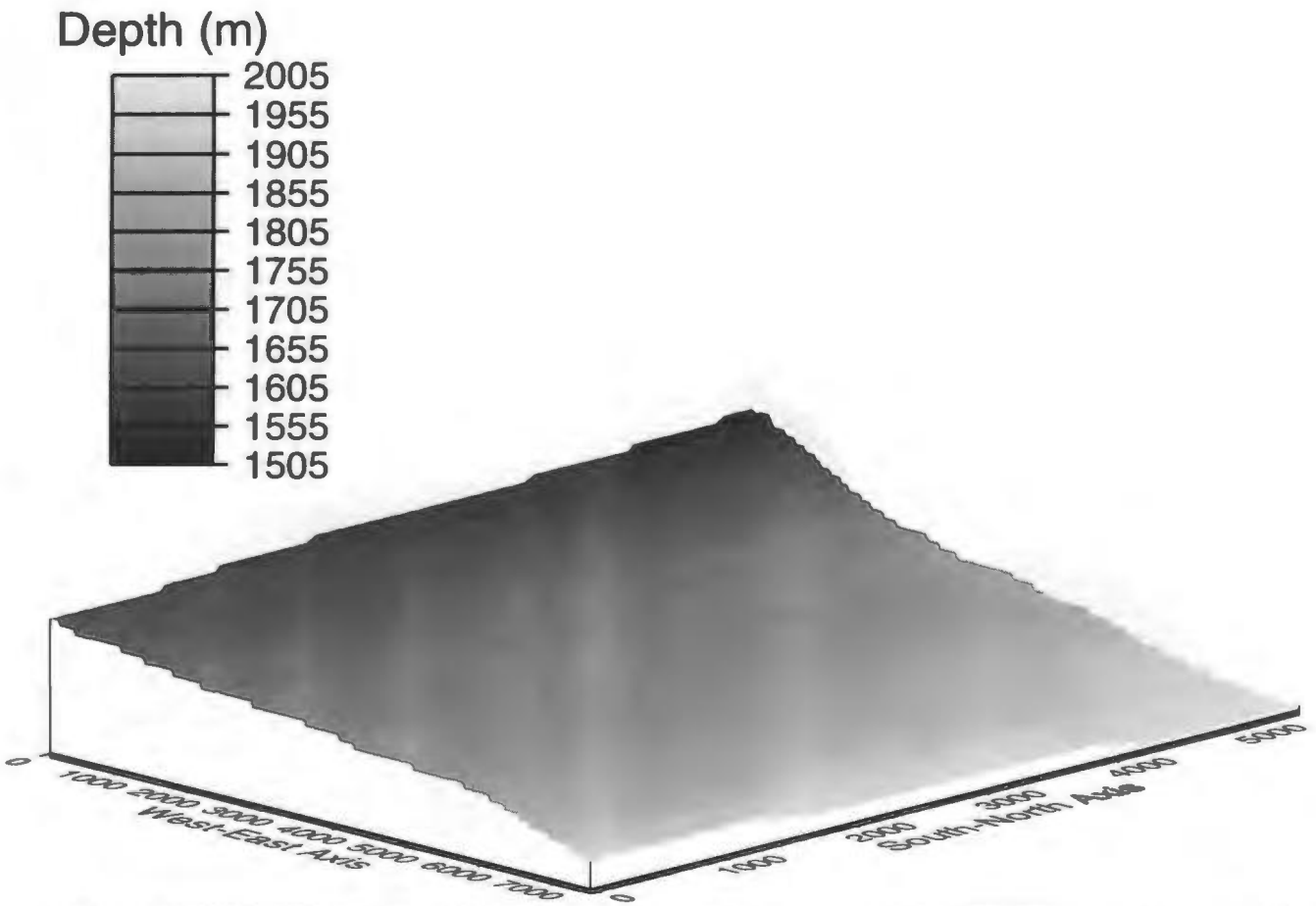

Figure 2.1(b). The Petrel Member has a minimum depth of 1350 m below sea level and a maximum depth of 1980 m below sea level. The Petrel limestone is a strong seismic marker throughout the Hibernia field.

Ekt3 Horizon

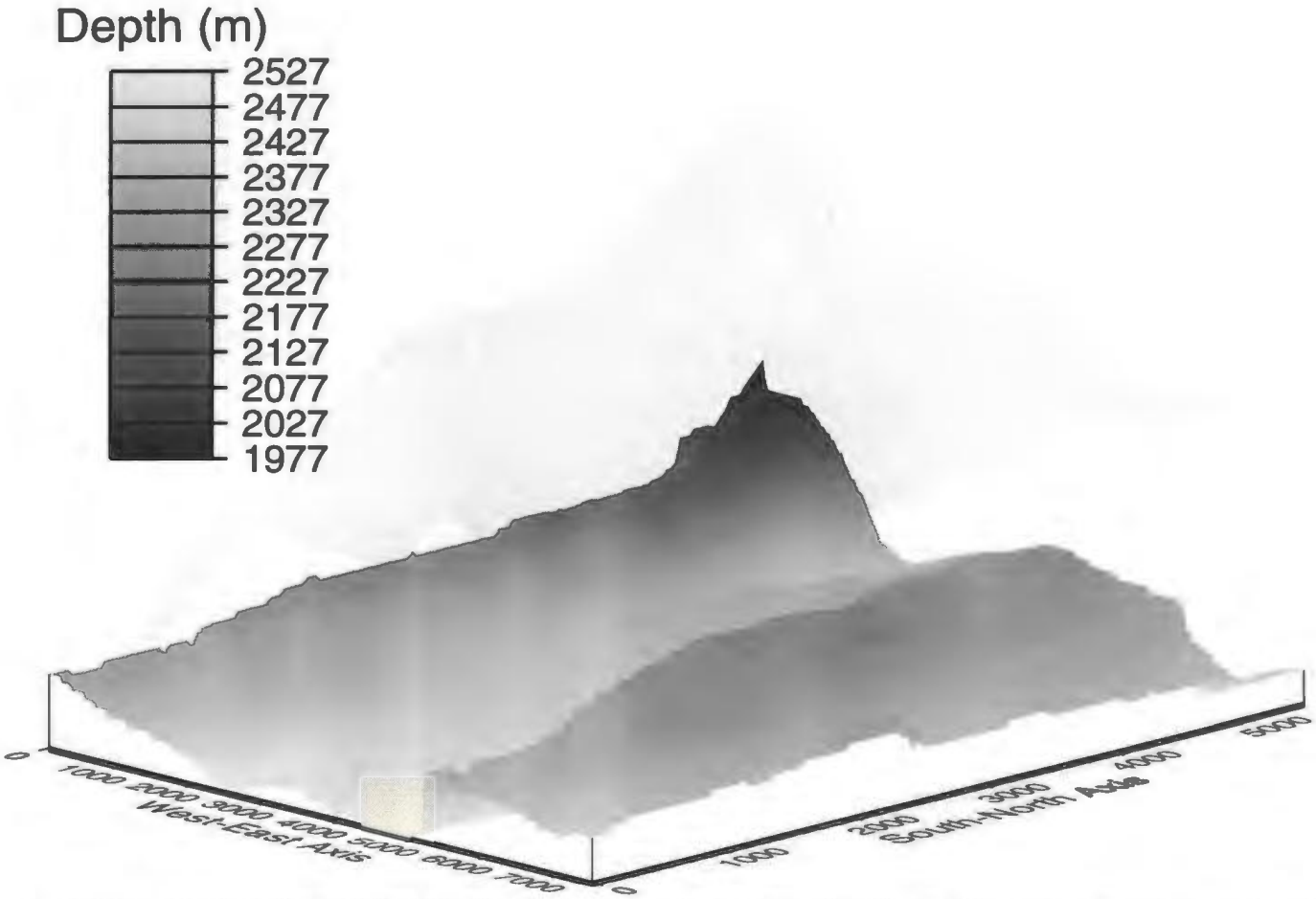

Figure 2.1(c). The Ekt3 horizon has a minimum depth of 1950 m below sea level and a maximum depth of 2505 m below sea level. The Ekt3 horizon is an apparent early Cretaceous truncation surface interpreted as corresponding to the base of the Ben Nevis formation.

Aan7 Horizon

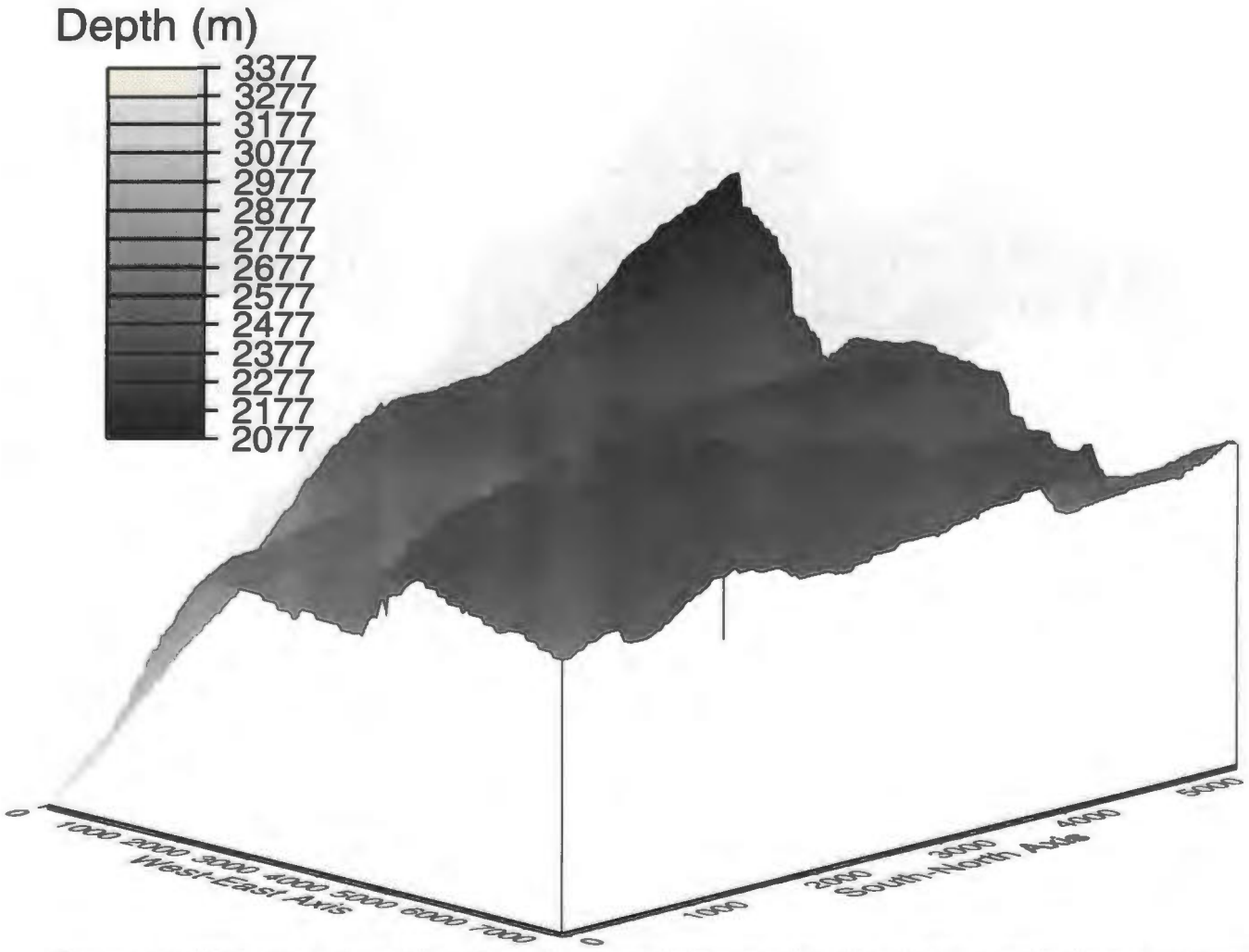

Figure 2.1(d). The Aan7 horizon has a minimum depth of 2025 m below sea level and a maximum depth of 3330 m below sea level. The Aan7 horizon is a seismic marker interpreted as corresponding to the base of the Lower Avalon Formation.

Am2 Horizon

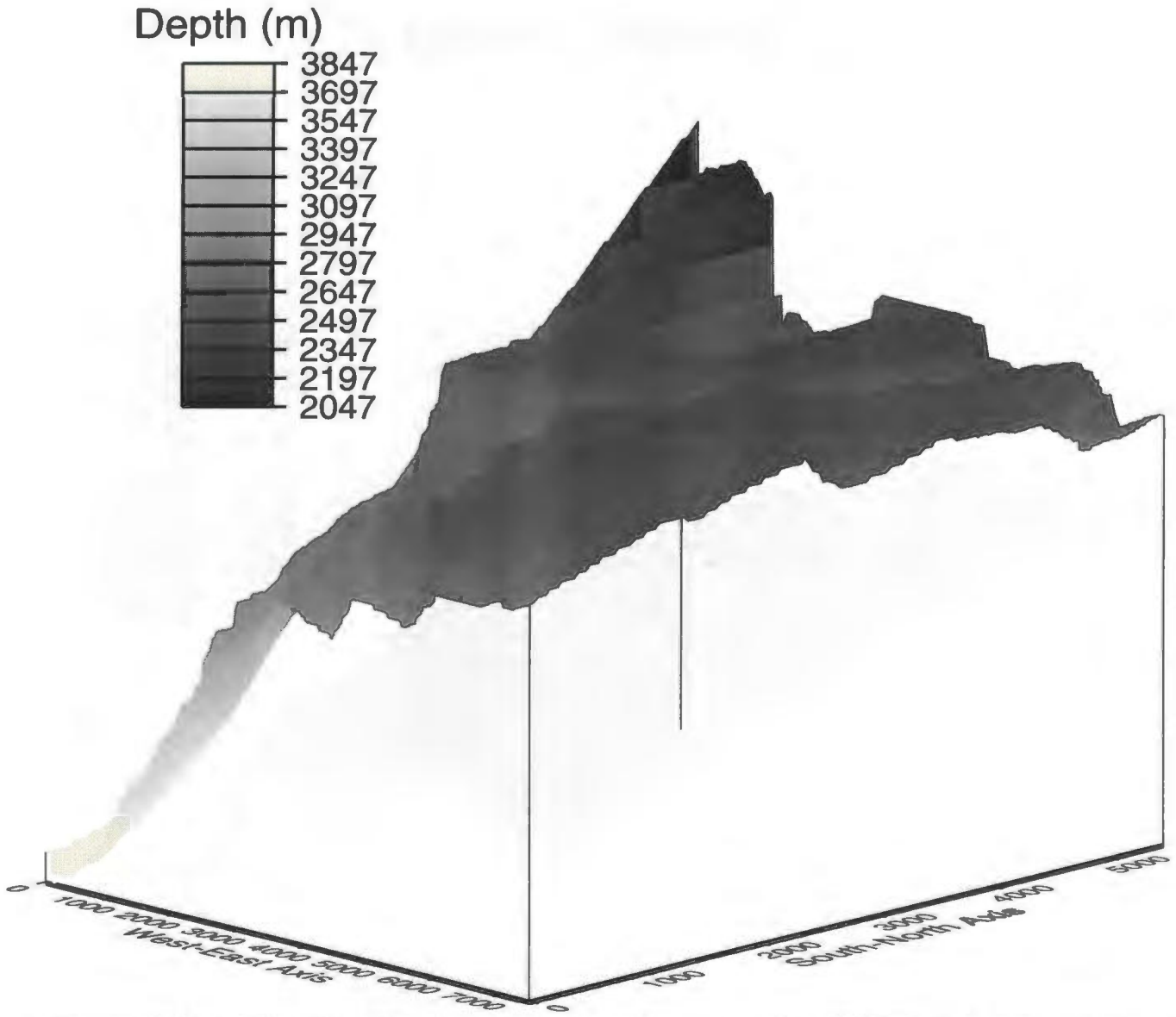

Figure 2.1(e). The Am2 horizon has a minimum depth of 2025 m below sea level and a maximum depth of 3870 m. The Am2 horizon is the 'A' marker Member limestone on the stratigraphic section.

Catalina Member

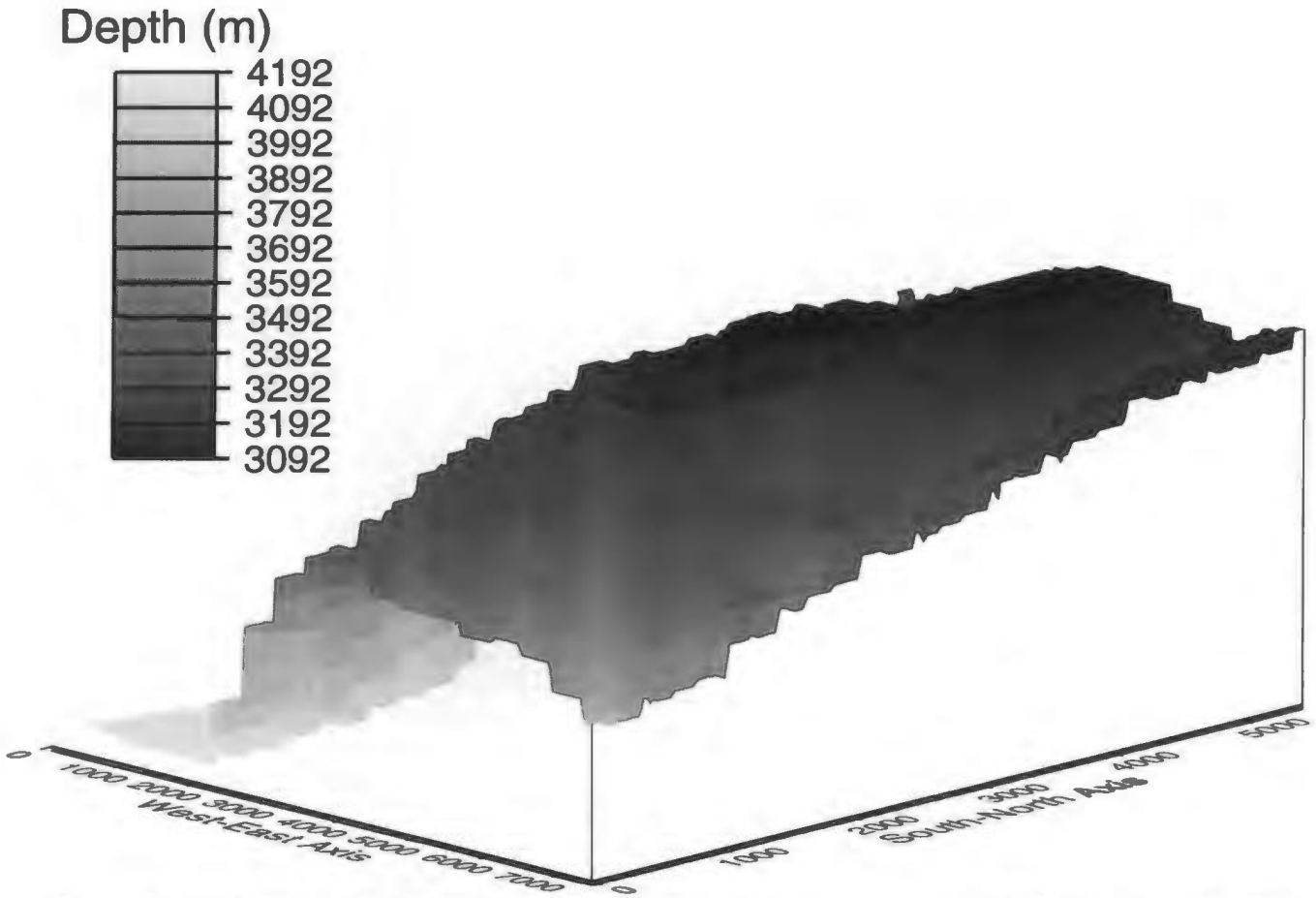

Figure 2.1(f). The Catalina Member has a minimum depth of 3060 m below sea level and a maximum depth of 4125 m below sea level.

Lower Hibernia Horizon

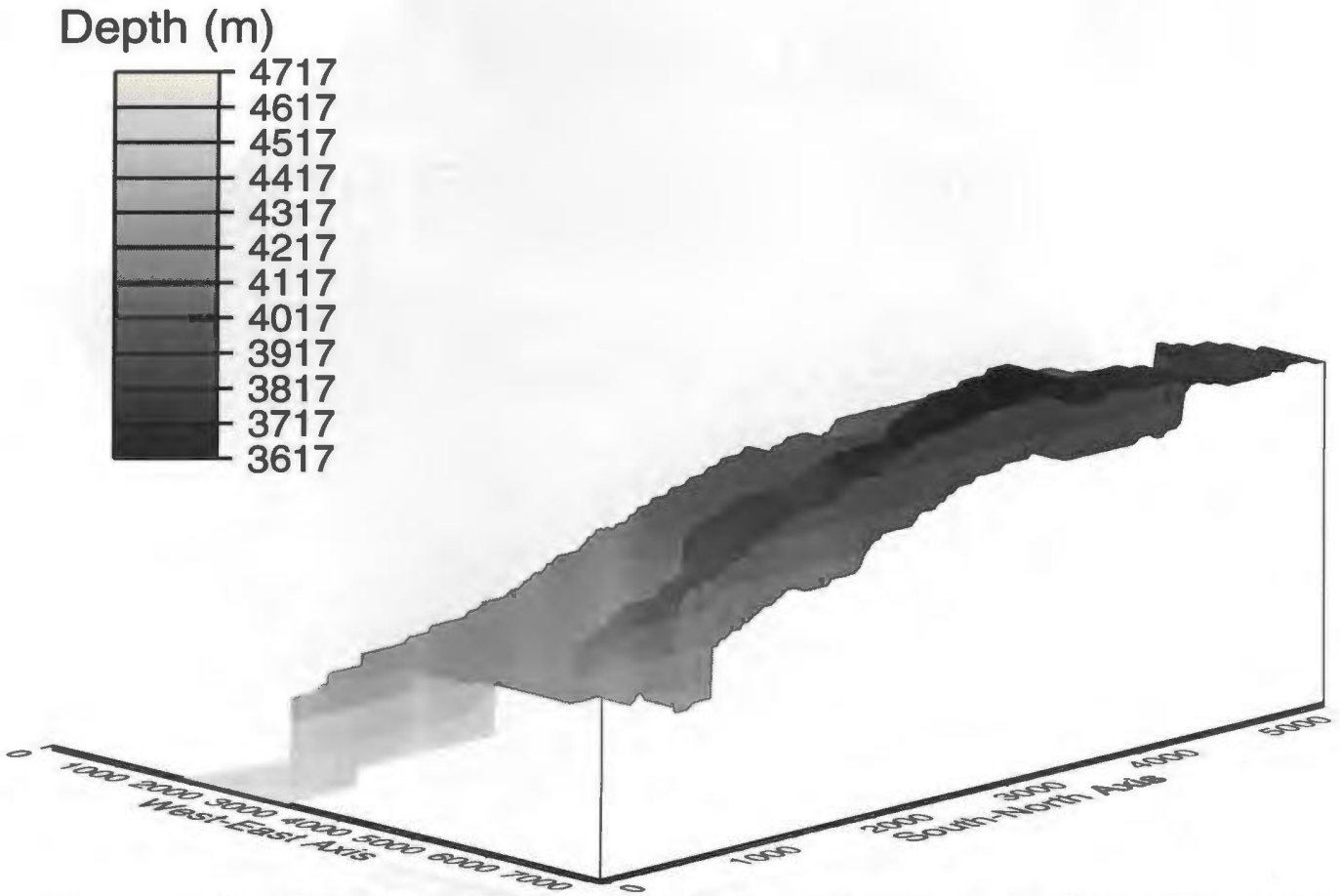

Figure 2.1(g). The Lower Hibernia horizon has a minimum depth of 3600 m below sea level and a maximum depth of 4635 m below sea level. This horizon represents the top of the Lower Hibernia zone from the stratigraphic section.

Murre Fault

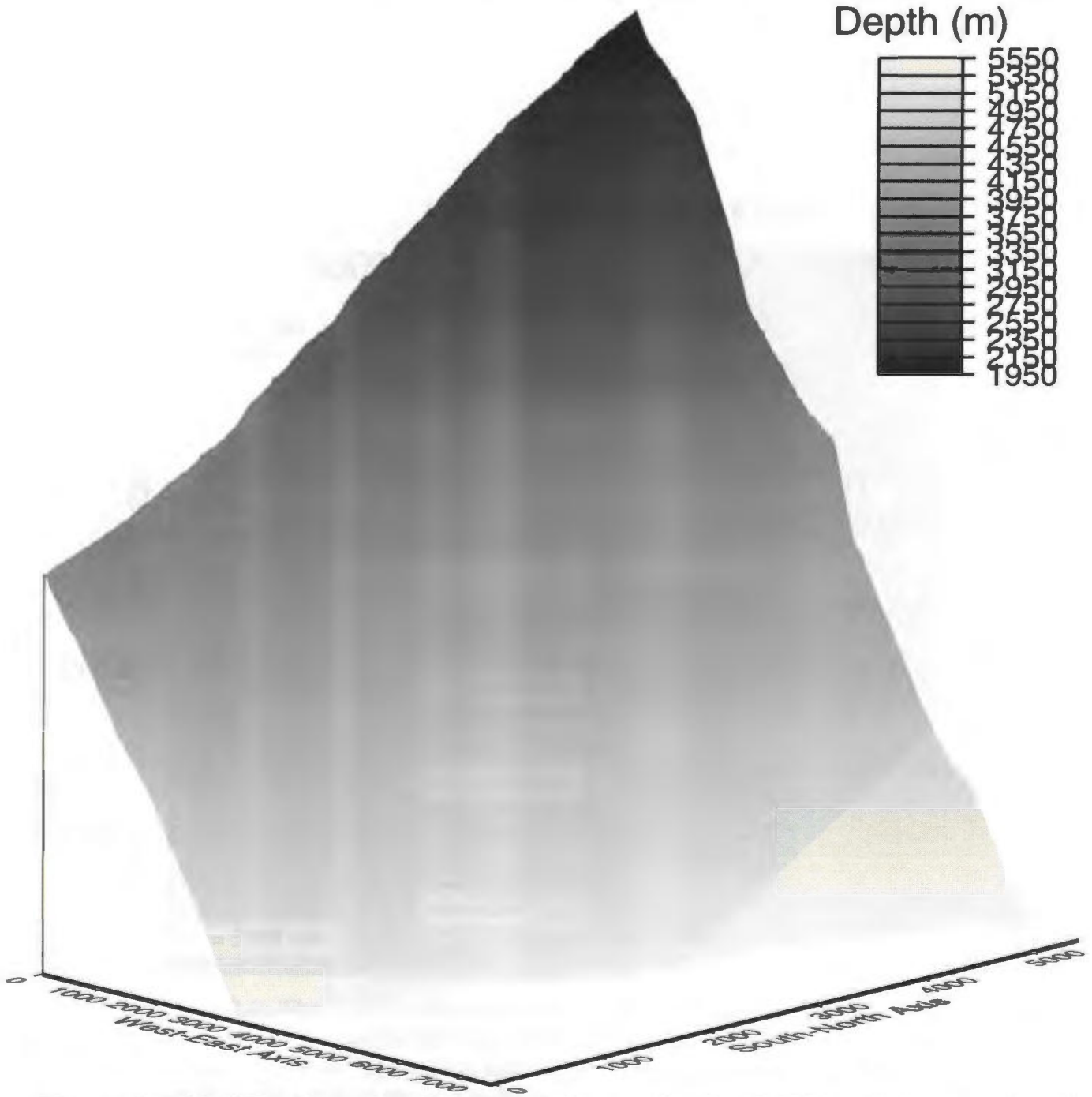

Figure 2.1(h). The Murre fault has a minimum depth of 1965 m below sea level and a maximum depth of 5535 m below sea level.

Simple Hibernia Model

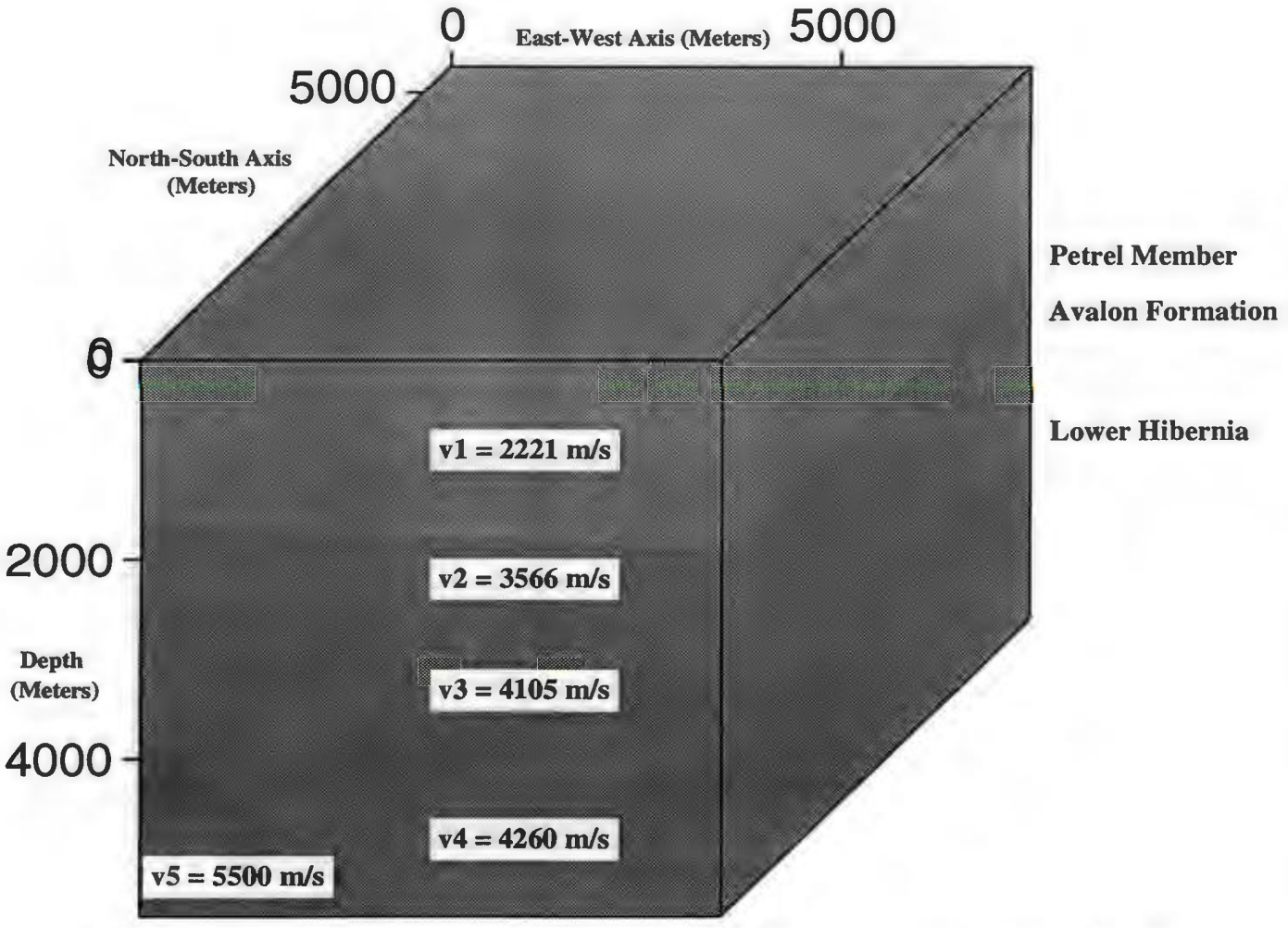

Figure 2.2: The 3 layer Hibernia model contains three stratigraphic layers and the Murre fault. The north and east correspond to the higher numbers on the axes of the plot. There are 213 grid points in the easterly direction, 157 in the northerly direction, and 370 in the z-direction.

Complex Hibernia Model

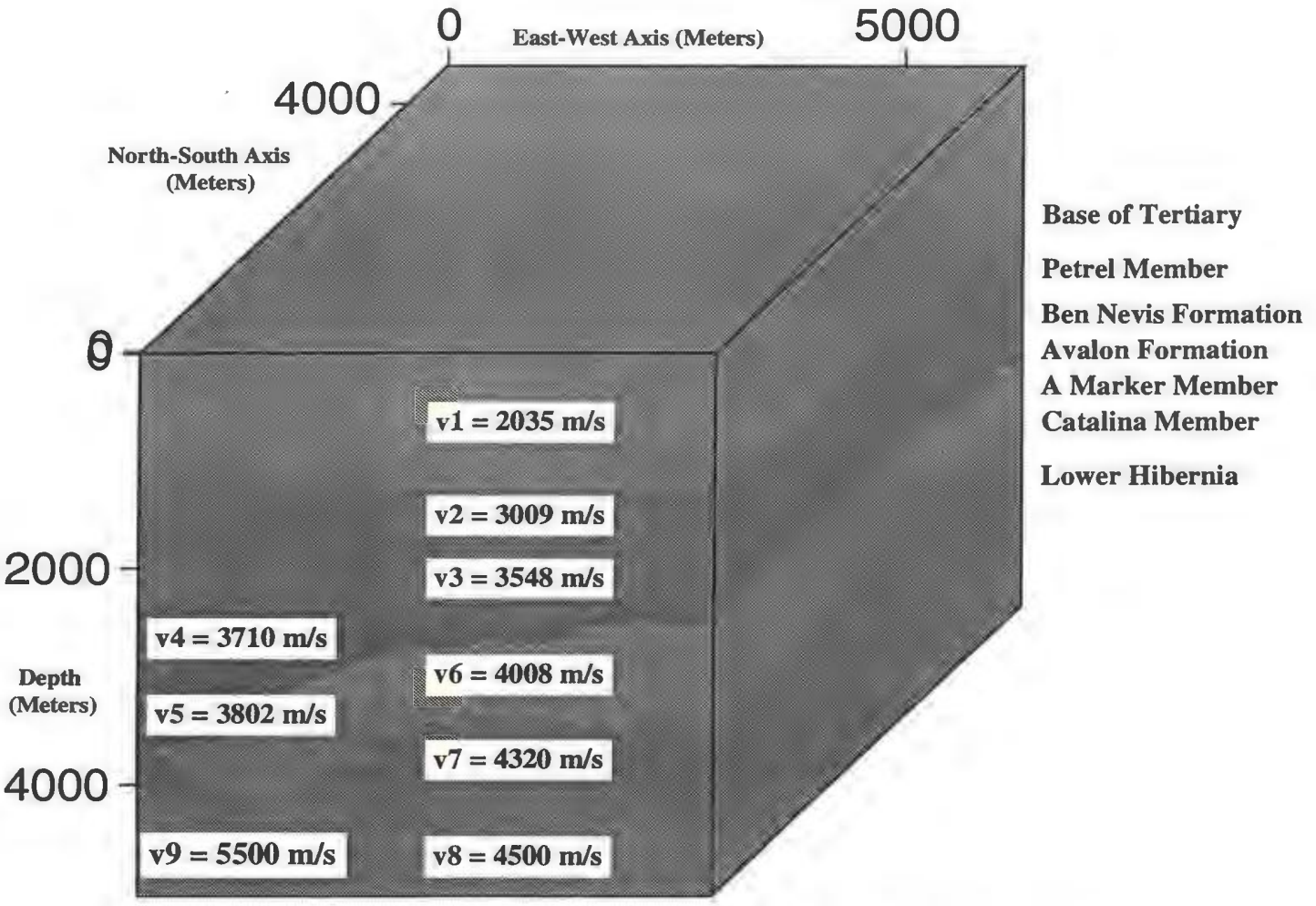

Figure 2.3: The 7 layer Hibernia model contains seven stratigraphic layers and the Murre fault. The north and east correspond to the higher numbers on the axes of the plot. There are 180 grid points in the easterly direction, 132 in the northerly direction, and 333 in the z-direction.

used for h_z is 15 m in order to improve the runtime of the algorithm. The grid spacing for the x- and y-directions is taken to be 35 m. The maximum velocity and h_z, along with the time and spatial weights described in section 2.4.1, are substituted into equation 2.7 resulting in $\Delta t \leq 0.0027$ seconds. The actual value taken for Δt is 0.002 seconds. The three layer velocity-depth model contained 213 x-points, 157 y-points, and 370 z-points. The seven layer model contained 180 x-points, 132 y-points, and 333 z-points.

Chapter 3. Post-stack migration of Hibernia data

3.1. Poststack migration algorithms

Successful poststack migration of seismic data requires a suitable migration algorithm in addition to an accurate estimate of the spatially varying seismic velocity. Poststack migration algorithms are available which operate in various domains (space-time, space-frequency, wavenumber-frequency, etc.), and which may be considered as either a time or depth migration. Time migrations produce an output section in time which may or may not be converted to a depth section by simply applying a stretch from time to depth (Whitmore et al., 1988). Depth conversion along vertical raypaths is valid only for regions with no structural dip, where there are only vertical velocity variations ((Yilmaz, 1988) and Robinson and Treitel (1980)). A migrated time section is often converted to depth using the image ray method, but this two stage depth migration process is incapable of handling lateral velocity variations (Hubral, 1977). In contrast, depth migrations produce migrated sections in depth, and are able to honor lateral velocity variations.

Individual migration algorithms are based upon specific assumptions about the input seismic data set and the underlying geology of the area of interest. In particular, assumptions are made regarding the structural complexity and velocity variations present in the region. This poststack migration analysis of Hibernia seismic data will focus on three different migration algorithms - frequency-wavenumber domain

migration (Stolt, 1978), phase-shift migration (Gazdag, 1978), and reverse-time migration (McMechan (1983) and Baysal et al. (1983)). Analysis of a migration algorithm's performance will involve considerations of accuracy, speed, ease of implementation, and computer requirements.

3.1.1. Frequency-wavenumber domain migration

Frequency-wavenumber domain migration is a time migration often referred to as Stolt migration. This method is extremely fast and is based upon a constant velocity model. Stolt migration cannot honor lateral velocity variations, and may even produce noticeable errors when faced with significant vertical velocity variations (Judson et al. 1980). Wave propagation in a layered earth with vertically varying velocities cannot be approximated by a constant velocity model, and input traces must be stretched from time to depth prior to migration to simulate these conditions. Advantages of the Stolt migration include its speed and ability to image steep dips, and its performance under low signal/noise ratios (Chun and Jacewitz, 1980).

In two dimensions, and within the constraints of the exploding reflector model, the acoustic wave equation is expressed as

$$\left(\frac{\partial^2}{\partial x^2}+\frac{\partial^2}{\partial z^2}-\frac{4}{v(x,z)^2}\frac{\partial^2}{\partial t^2}\right)P(x,z,t)=0\ . \tag{3.1}$$

where $v(x,z)$ is the velocity of the medium and $P(x,z,t)$ is the acoustic pressure wavefield. The basis of frequency-wavenumber domain migration is the 2-D Fourier transform of equation (3.1) over x and t. This transform produces $p(k_x,z=0,\omega)$ from $P(x,z=0,t)$. Next, the temporal frequency ω is mapped onto the vertical

wavenumber domain using the dispersion relation

$$\omega^2 = \left(\frac{v}{2}\right)^2 \left(k_x^2 + k_z^2\right). \tag{3.2}$$

while the horizontal wavenumber is left unchanged. This wavenumber mapping is consistent with the migrator's equation (Chun and Jacewitz, 1980). The amplitudes are then scaled by

$$\frac{v}{2}\frac{k_z}{\sqrt{(k_x^2 + k_z^2)}}. \tag{3.3}$$

creating $p(k_x, k_z, t = 0)$. This amplitude scaling operation is consistent with conservation of energy (Chun and Jacewitz, 1980). A 2-D inverse Fourier transform is then applied to create the migrated section, $P(x, z, t = 0)$ (Yilmaz, 1988).

3.1.2. Phase-shift migration

Phase-shift migration is a depth migration in the wavenumber-frequency domain that is capable of accommodating a depth-variable velocity function (Gazdag, 1978). Two-dimensional poststack depth migration algorithms are based on the exploding reflector model, and seek to reconstruct the acoustic pressure wavefield $P(x, z, t)$ at $(x, z, t = 0)$, from the recorded seismic data at $(x, z = 0, t)$. The use of the exploding reflector model subdivides the poststack migration operation into a wavefield extrapolation or downward continuation operation in which $P(x, z = 0, t)$ is transformed into $P(x, z, t)$, and an imaging step in which $P(x, z, t)$ is transformed into $P(x, z, t = 0)$ (Whitmore et al, 1988).

Two-dimensional poststack phase-shift migration begins with a Fourier transform

of equation (3.1) with respect to x and t, thereby producing equations (3.4) and (3.5).

$$\frac{\partial^2 p}{\partial z^2} + k_z^2 p = 0 \tag{3.4}$$

$$k_z = \pm\sqrt{\frac{4\omega^2}{v^2} - k_x^2} \tag{3.5}$$

In this equation, $p(k_x, z, \omega)$ is the 2-D Fourier transform of $P(x, z, t)$ with respect to x and t . The velocity is assumed to be laterally invariant, and $v(z)$ is assumed to be constant within depth strips of thickness Δz. This leads to exact solutions of equation (3.4) in the form of

$$p(k_x, z + \Delta z, \omega) = p(k_x, z, \omega).e^{(ik_z \Delta z)} \ . \tag{3.6}$$

Equation(3.6) is the extrapolation formula for phase-shift migration, and must be applied for every Fourier component of $p(k_x, z, \omega)$. The imaging condition is then implemented by summing over all frequencies. Finally, a 1-D inverse Fourier transform from $(k_x, z, t = 0)$ to $(x, z, t = 0)$ is applied to the imaged field for each depth. Whitmore et al. (1988) report that the operation count of a phase-shift migration is dominated by $O(N_z N_\omega N_x)$ complex operations. The phase-shift migration method is very accurate since the numerical procedure is free of truncation errors, and there is no stability condition limiting the size of Δt (Gazdag, 1978).

3.1.3. Reverse-time migration

Reverse-time migration is a depth migration in the space-time domain which uses finite-difference solutions to the wave equation to perform migration as a backward time marching scheme (McMechan (1983), Baysal et al. (1983), and Whitmore(1983)).

This method is the reverse of forward modeling using finite-difference techniques and the exploding reflector method, and is subject to the same considerations of stability and dispersion. Reverse-time migration uses the input seismic traces as a series of band-limited time-varying sources that act as a surface boundary condition (Levin (1984) and Harris and McMechan (1992)). Reverse-time migration solves the full wave equation in fixed spatial coordinates using the exploding reflector model. In two dimensions, equation (3.1) may be represented by a finite-difference approximation which is second-order accurate in time and fourth-order accurate in space.

$$u_{i,k}^{n+1} = \left[2 - \frac{5}{4}\left(\frac{v(x,z)^2\Delta t^2}{h^2}\right)\right] u_{i,k}^{n} + \frac{v(x,z)^2\Delta t^2}{48h^2}\left[16[u_{i+1,k}^{n} + u_{i,k+1}^{n} + u_{i-1,k}^{n} + u_{i,k-1}^{n}] - [u_{i+2,k}^{n} + u_{i,k+2}^{n} + u_{i-2,k}^{n} + u_{i,k-2}^{n}]\right] - u_{i,k}^{n-1} \tag{3.7}$$

Here, $v(x,z)$ is half the layer velocity since reverse-time migration uses the exploding reflector model. This finite-difference approximation uses a uniform grid spacing (h) in x and z, and may require interpolation in both directions to satisfy stability and dispersion conditions. Application of equation (2.7) using second-order time weights and fourth-order spatial weights requires that

$$\frac{v_{max}\Delta t}{h} \leq \sqrt{\frac{3}{8}} \tag{3.8}$$

in order to satisfy stability.

The wavefield and its time derivative are set to zero throughout the subsurface at the start time of the migration. The input seismic data at t_{max} provide the values for $P(x, z = 0, t)$, and equation (3.7) propagates these values throughout the subsurface. This operation continues for t_{max}, $t_{max} - \Delta t$, $t_{max} - 2\Delta t$, ... until time zero is reached.

As is the case in finite-difference modeling, boundary conditions must be invoked in reverse-time migration to avoid artificial reflections from the sides and base of the model. The 2-D reverse-time migration algorithm used in this project also uses the method of damping sponges to avoid such boundary reflections. Reverse-time migration requires $O(N_x..N_z..N_t)$ operations, where the size of N_x, N_z, and N_t is dependent upon the finite-difference stencil (equation (3.7)). The order of the finite-difference approximation controls the number of grid points per wavelength which are needed to avoid grid dispersion, and the resultant grid spacing, in conjunction with the maximum velocity, controls the time sampling necessary to satisfy stability criteria.

Two-dimensional reverse-time migration is at a disadvantage when compared to other methods because of greater computation costs and the lack of a specialization to a v(z) migration(Whitmore et al., 1988). However, the reverse-time migration is independent of dip and is easy to code and implement on a computer with enough main memory to hold the necessary input data for the required three time steps.

3.1.4. 3-D reverse-time migration

Three-dimensional reverse-time migration is very similar to 3-D forward modeling as described in chapter two. Equation (2.4) is the finite-difference approximation to the 3-D wave equation which is the basis of 3-D reverse-time migration. The same stability and dispersion criteria, as well as boundary condition considerations, are also required for 3-D reverse-time migration. It is often necessary to interpolate 3-D seismic data in both the x- and y-directions to satisfy the stability and dispersion

criteria, and this can lead to large values for N_x and N_y. Three-dimensional reverse-time migration requires a large amount of computer time and memory, but can provide a high quality of seismic imaging for data sets which are complex enough to warrant its application. New innovations, such as variable grid spacing in the z-direction (Jastram and Behle, 1992), aid in reducing the cost of this technique, and it is now seeing application in imaging 3-D seismic data from areas such as the Gulf of Mexico (Mufti et al., 1996).

3.2. Poststack migration of Hibernia model data

The three layer Hibernia model (Figure 2.3) generated a cube of seismic data that consisted of 173 inlines with 117 crosslines. Inlines were defined as those lines which extended in the north-south direction, while crosslines extended in the east-west direction. There were 1600 time samples at a sampling rate of 0.002 seconds. A smaller cube of model data, consisting of 100 inlines and 100 crosslines, was migrated using the 3-D migration. As well, several inlines and crosslines were migrated using the 2-D migration algorithms. All computations were performed on a Sparc 10 computer, unless otherwise indicated. The results will be shown for inline 30, a north-south line at an east-west position of 1750 m, and crossline 30, an east-west line at a north-south position of 1750 m.

The Stolt migration required a $v(t)$ rms velocity function, and a stretch factor to approximate wave propagation in an earth with vertically varying velocities. The $v(t)$ velocity function was derived by converting the model interval velocities to rms

velocities. These velocities were placed at the times corresponding to the average depth of each layer in the model. It was particularly difficult to correctly position the fault using this migration technique as the depth of the fault varies significantly along the seismic section. This illustrates one of the limitations of Stolt migration. However, the migration is very fast, requiring only seconds to compute for these model lines. The phase-shift migration required a $v(t)$ interval velocity function, and output a time section as the migrated result. A time section was output because the phase-shift migration algorithm converted the depth data to time data automatically after the migration was completed. The migration required approximately 60 minutes of cpu time for these model lines. The Stolt and phase-shift migrations were converted to depth to allow for comparison with the reverse-time migration results using vertical raypaths and the same interval velocity function that was used in the phase-shift migration. This stretch from time to depth is easily done and requires only seconds of cpu time.

Prior to performing reverse-time migration it is necessary to calculate the required grid spacing and time sampling as outlined in section 3.1.3 and equations 2.8 and 3.8. The velocities used in these equations are half the medium velocities since this technique is based on exploding reflector modeling. The minimum velocity in this model is 2221 m/s and the maximum velocity is 5500 m/s. The value taken for w for a two-dimensional model is 5, and the maximum frequency is assumed to be 30 Hz. This leads to a recommended grid spacing of 7.40 m and a Δt of 0.001 ms for the 2-D reverse-time migration. The seismic data and the $v(x,z)$ velocity model

must be interpolated to this grid spacing before computing the migration result. The actual grid spacing which was used in the 2-D reverse-time migration was 8.75 m. since it was easier to interpolate the data to this spacing from an original grid spacing of 35 m and 15 m. The $v(x, z)$ velocity-model is the exact velocity model for each line as defined in the original finite-difference model. The 2-D reverse-time migration requires approximately 3 hours of cpu time to output a depth section for this model data. and that section must then be decimated to the original trace spacing for plotting purposes. The 3-D reverse-time migration algorithm allows the grid spacing in the horizontal direction to be different from the grid spacing in the vertical direction. The conditions for avoiding dispersion and numerical instability in 3-D reverse-time migration are identical to those required for 3-D finite-difference modeling. and the 3-D reverse-time migration could therefore be run on the synthetic seismic data exactly as it was produced by the modeling algorithm. The horizontal grid spacing was 35 m. the vertical grid spacing was 15 m. and the time sampling rate was 0.002 ms. The 3-D migration of 100 inlines and 100 crosslines with a 20 trace padding at the ends of the lines required 48 hours of cpu time on a Sparcserver 1000 for 1500 time steps. The output depth model was only computed for 300 depth samples. rather than the full 370 depth samples that were actually contained in the model.

Figure 3.1(a) is a synthetic seismic section that was obtained for inline 30. and figures 3.2(a) - (d) are the results of the various migrations. In each case, the migration results have been overlain by thin black lines to show the location of the reflectors

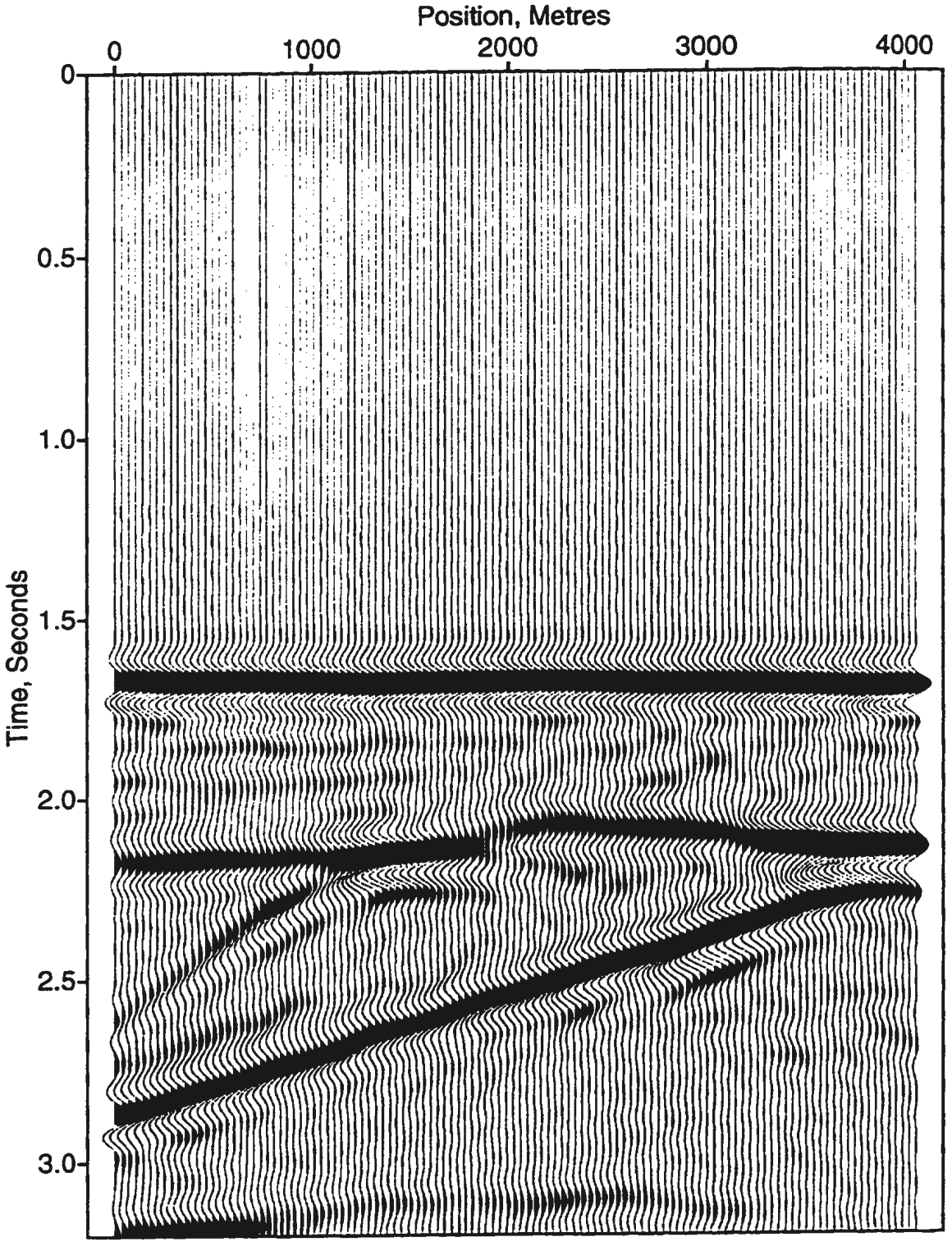

Figure 3.1 shows the synthetic seismic data for inline 30 from the three layer Hibernia model.

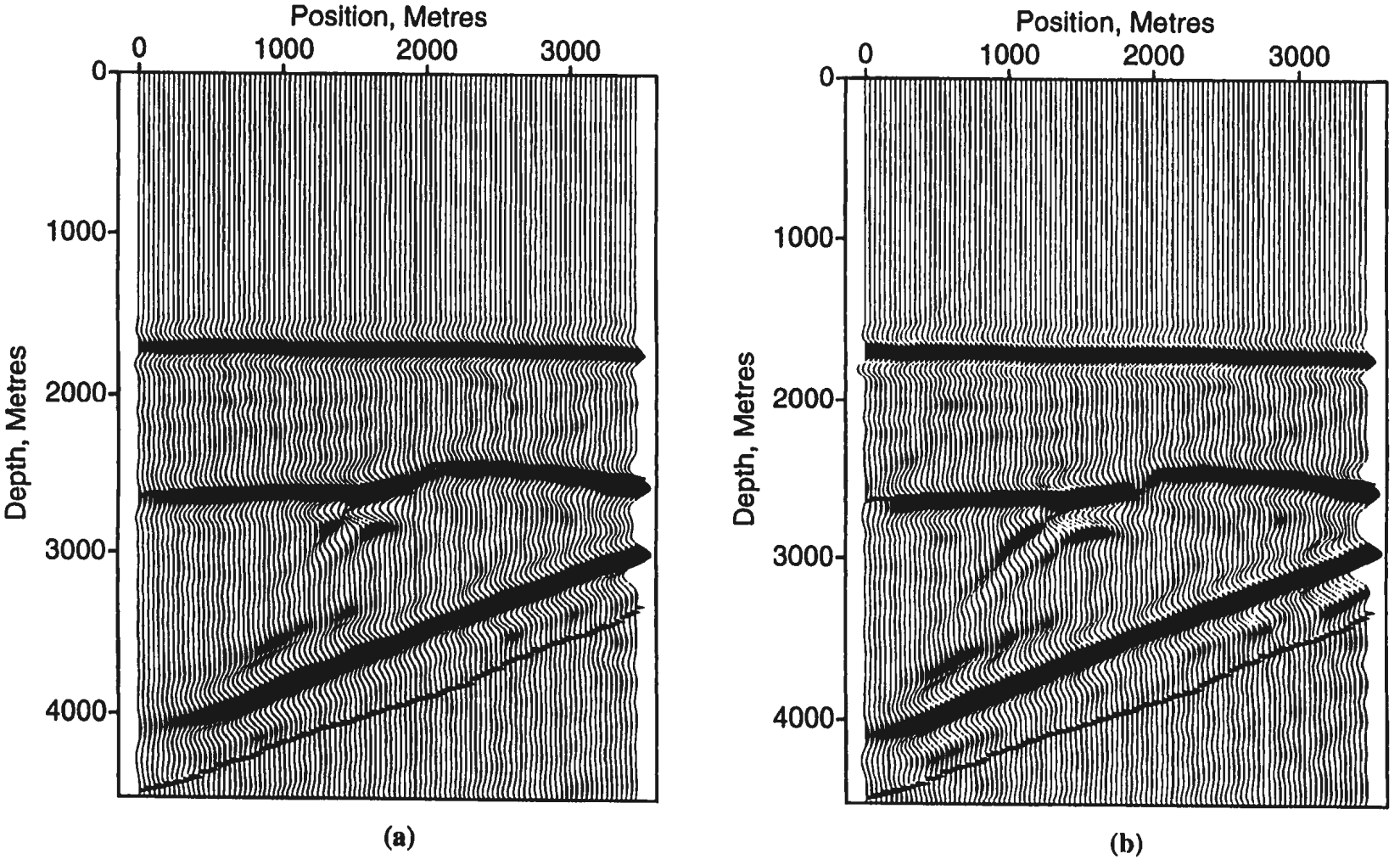

Figures 3.2(a) and (b) are the results of the Stolt and Gazdag migrations of inline 30 after conversion to depth to allow for comparison with the reverse-time migrations. The first two layers are the Petrel Member and the base of the Lower Avalon. The third layer is the location of the Murre fault on this line.

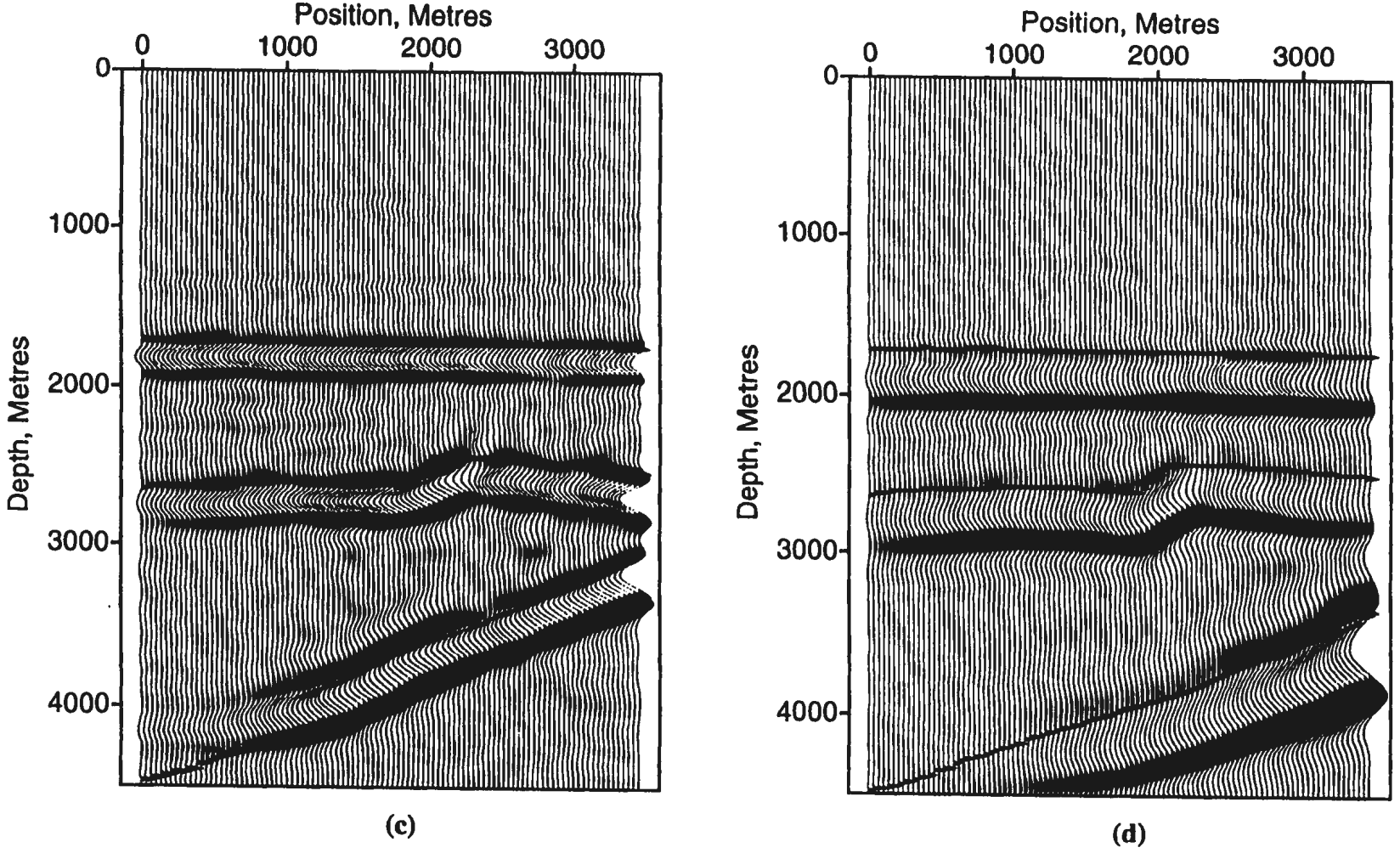

Figures 3.2(c) and (d) are the results of the 2-D and 3-D reverse-time migrations of inline 30, respectively. The 3-D migration is the only technique which places the Murre fault at the correct depth location.

as they were defined in the original finite-difference model. Figures 3.2(a) and 3.2(b) are the results of the Stolt and phase-shift migrations, respectively, after conversion to depth to allow for comparison with the reverse-time migration results. The top two horizons have been correctly positioned in both cases, but the Murre fault is placed at too shallow a depth. Figure 3.2(c) is the result of the 2-D reverse-time migration, and it also places the Murre fault at too shallow a depth. The 3-D reverse-time migration in figure 3.2(d) is the only technique which places the Murre fault in the correct position for this inline, since it is the only migration technique tested which is capable of correctly positioning out-of-plane energy.

Figure 3.3 is the synthetic seismic data for crossline 30, and the migration results are shown in figures 3.4(a) - (d). The Stolt and phase-shift migrations have still not correctly positioned the fault in depth, and there is crossover of the reflection from the Hibernia Formation with the fault. Figures 3.4(c) and (d) show that both the 2-D and 3-D reverse-time migrations have provided a correct spatial image for this line with only minor amplitude differences.

The seven layer Hibernia model produced 140 inlines and 92 crosslines of synthetic seismic data. The entire 3-D cube of data was migrated using the 3-D reverse-time migration algorithm, which required 67 hours of cpu time and approximately 21 days of wall clock time on a Sparc 10 computer. Results of the various migration algorithms will be shown for inline 60 and crossline 60. Inline 60 is a north-south line at an east-west position of 2800 m, and crossline 60 is an east-west line at a north-south position of 2800 m. The 2-D migrations of these lines required similar amounts of cpu time

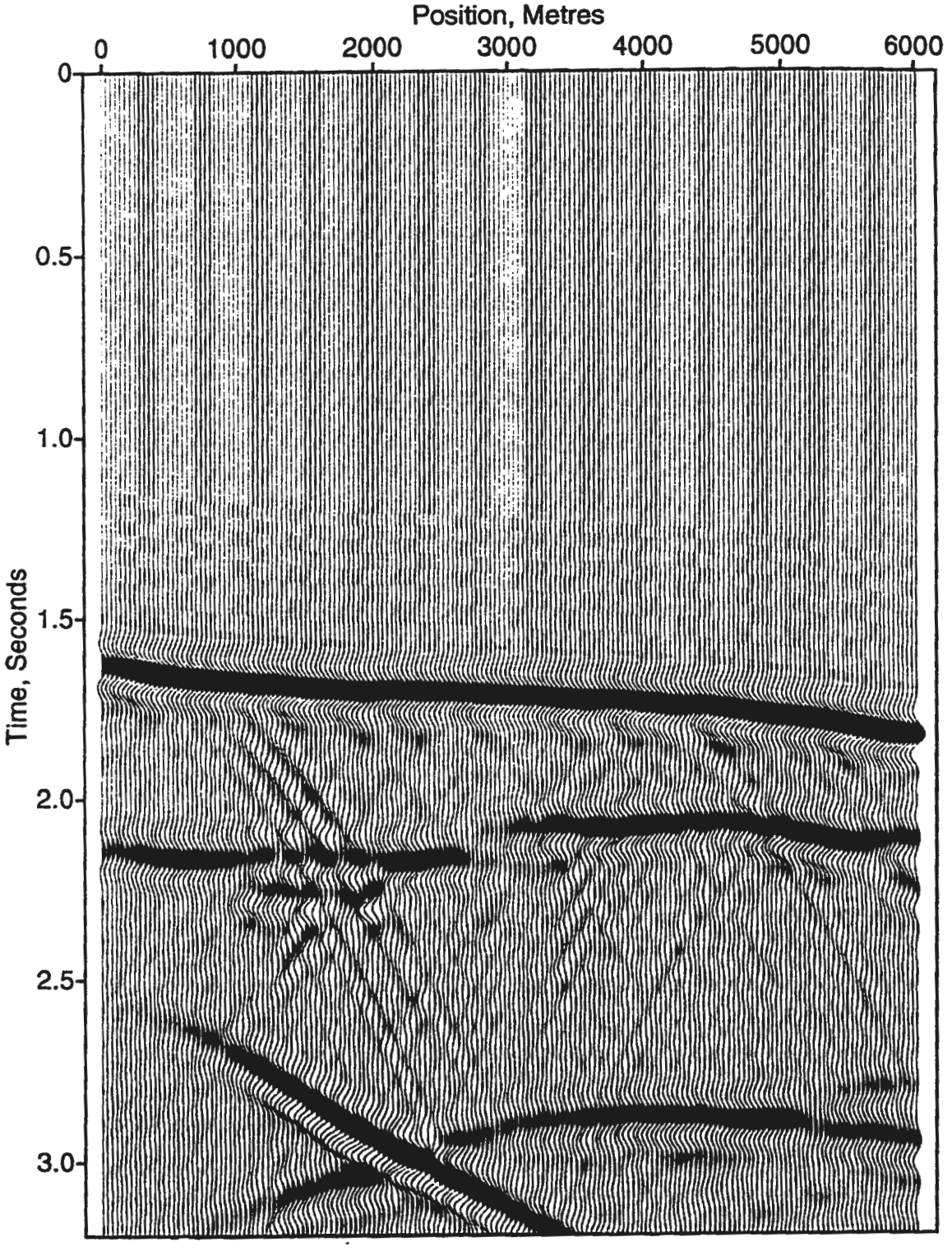

Figure 3.3 shows the synthetic seismic data for crossline 30 from the three layer Hibernia model.

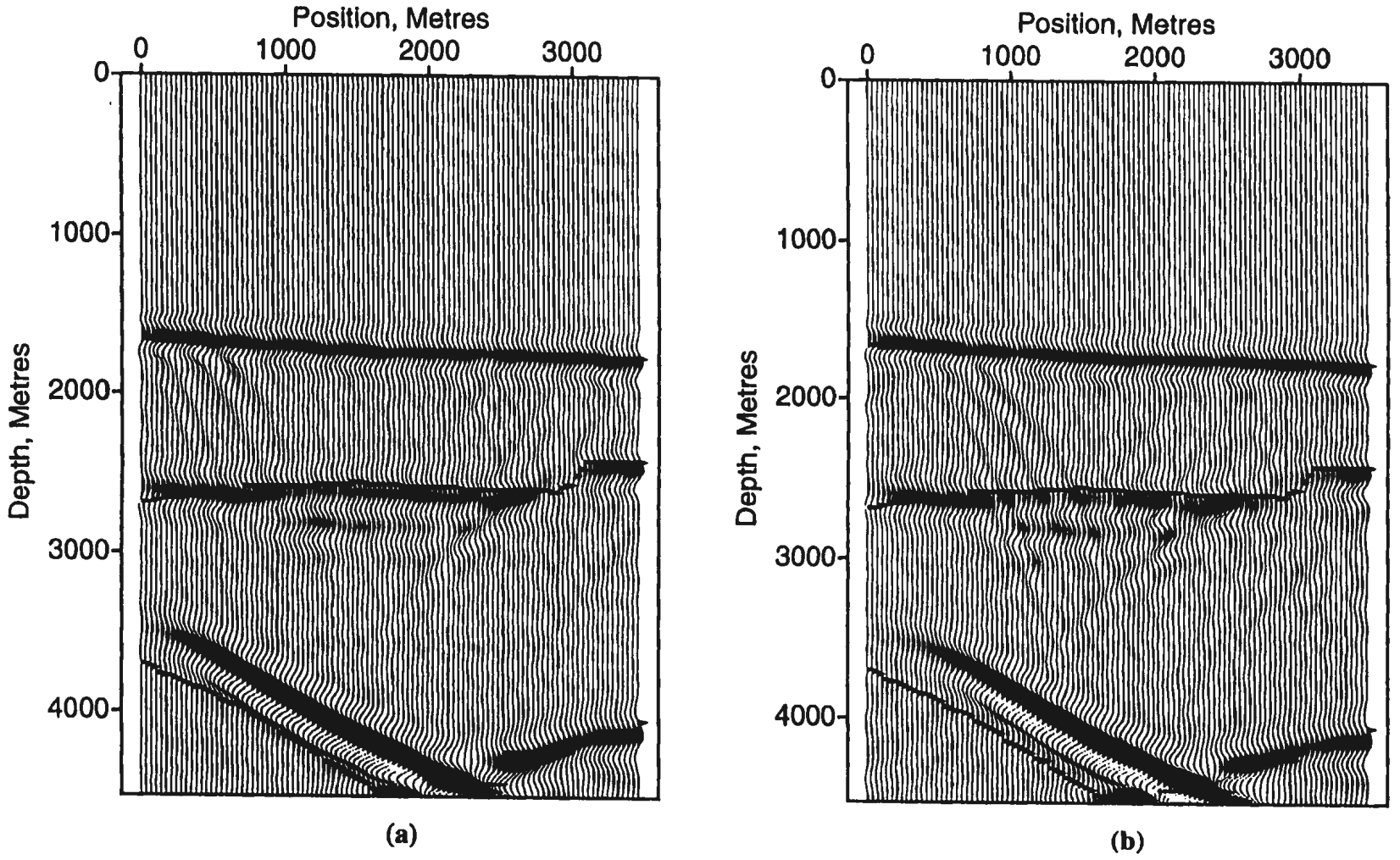

Figures 3.4(a) and (b) are the results of the Stolt and Gazdag migrations of crossline 30 after conversion to depth to allow for comparison with the reverse-time migrations. The Petrel Member, base of the Lower Avalon, and the Hibernia Formation are all present on this section.

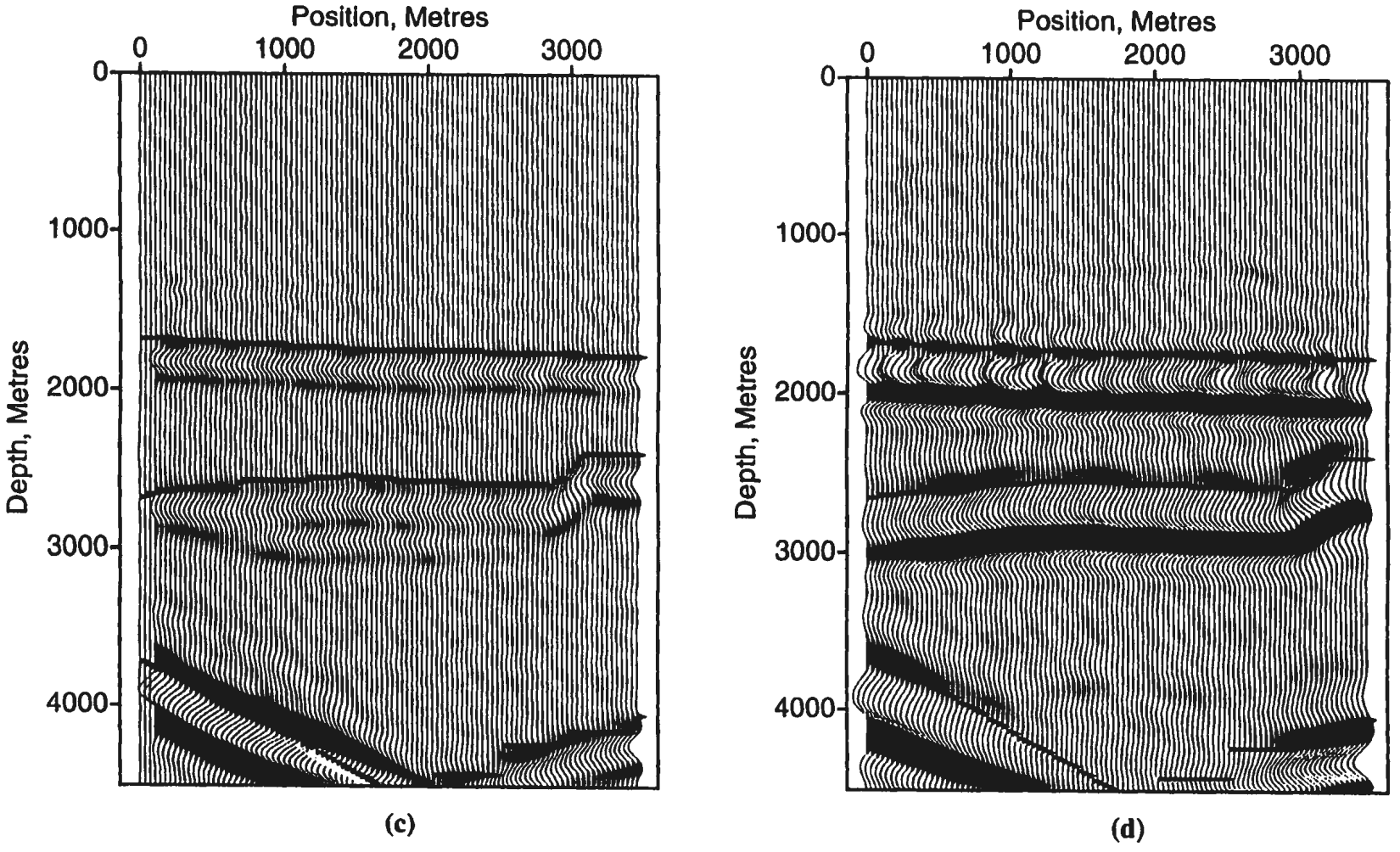

Figures 3.4(c) and (d) are the results of the 2-D and 3-D reverse-time migrations of crossline 30, respectively. There are no significant differences between the two migration results for this section.

as was described for inline 30 from the three layer model. The grid spacing for the reverse-time migrations was also the same as was used in the migrations of inline 30. Figure 3.5 shows the synthetic seismic data for inline 60, and figures 3.6(a) - (d) are the results of the various migrations. Figures 3.6(a) and (b) are the results of the Stolt and phase-shift migrations, respectively, after conversion to depth. In both cases, the Murre fault has been plotted at too shallow a depth. Figure 3.6(c) is the result of the 2-D reverse-time migration, which also places the Murre fault (bottom reflector) at too shallow a depth. As well, the image of the Hibernia formation (second deepest reflector) in the middle of the section implies the presence of a rollover feature which does not actually exist. The result of the 3-D migration in figure 3.6(d) provides the best image of the fault and the Hibernia formation.

Figure 3.7 shows the synthetic seismic data for crossline 60, and figures 3.8(a) - (d) are the results of the various migrations. Figures 3.8(a) and (b) are the results of the Stolt and phase-shift migrations, with both migrations showing crossover of the Hibernia Formation reflection with the fault. The Murre fault is also placed at too shallow a depth in the section. Figure 3.8(c) is the result of the 2-D reverse-time migration, and correctly images all reflectors but provides a wavy image of the fault. The 3-D migration result in figure 3.8(d) provides the best result of all the migrations of crossline 60.

This migration analysis of Hibernia model data has shown that the 2-D reverse-time migration provides the most accurate image of all the 2-D migration techniques tested, but there are instances when even this method does not provide a correct

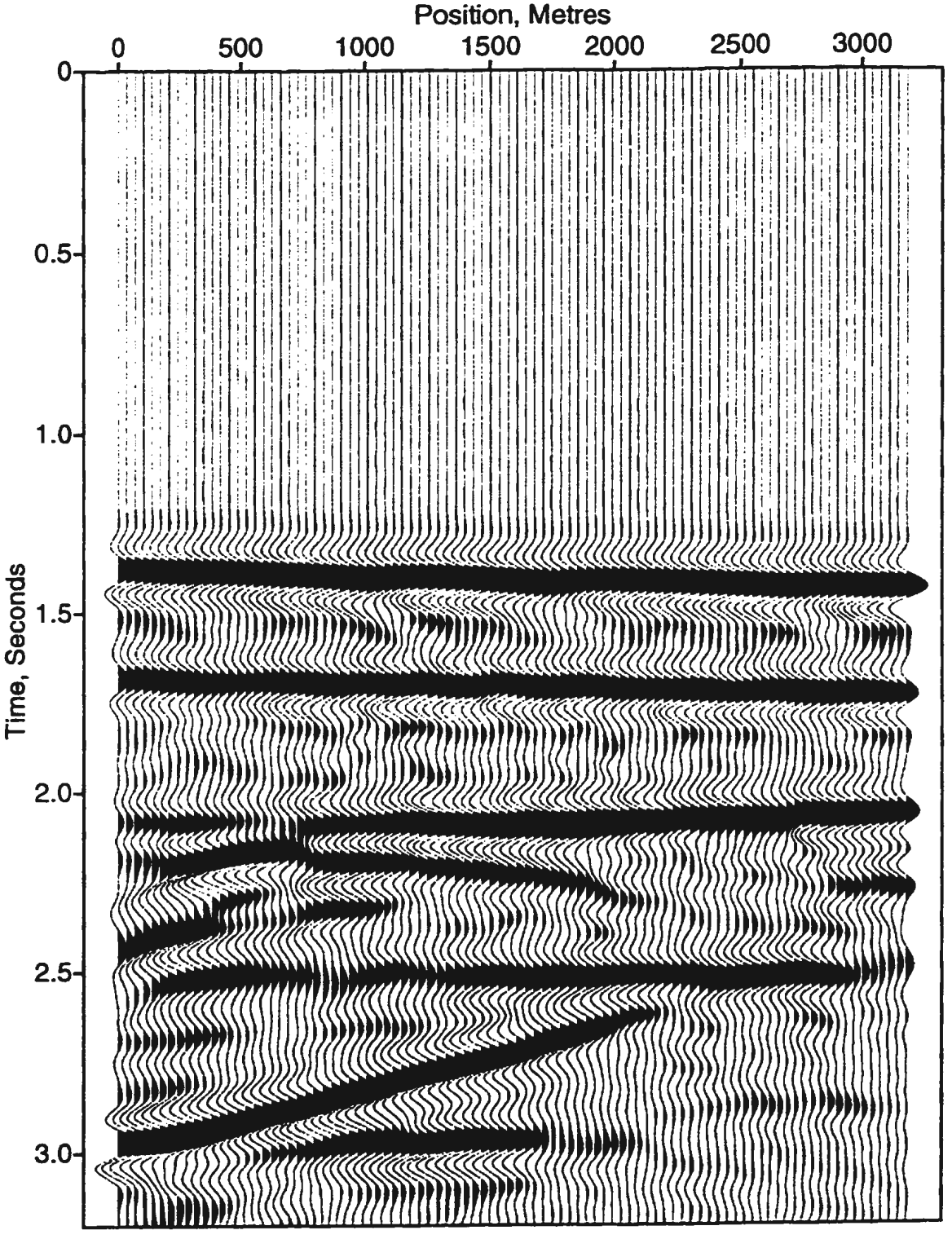

Figure 3.5 shows the synthetic seismic data for inline 60 from the seven layer Hibernia model.

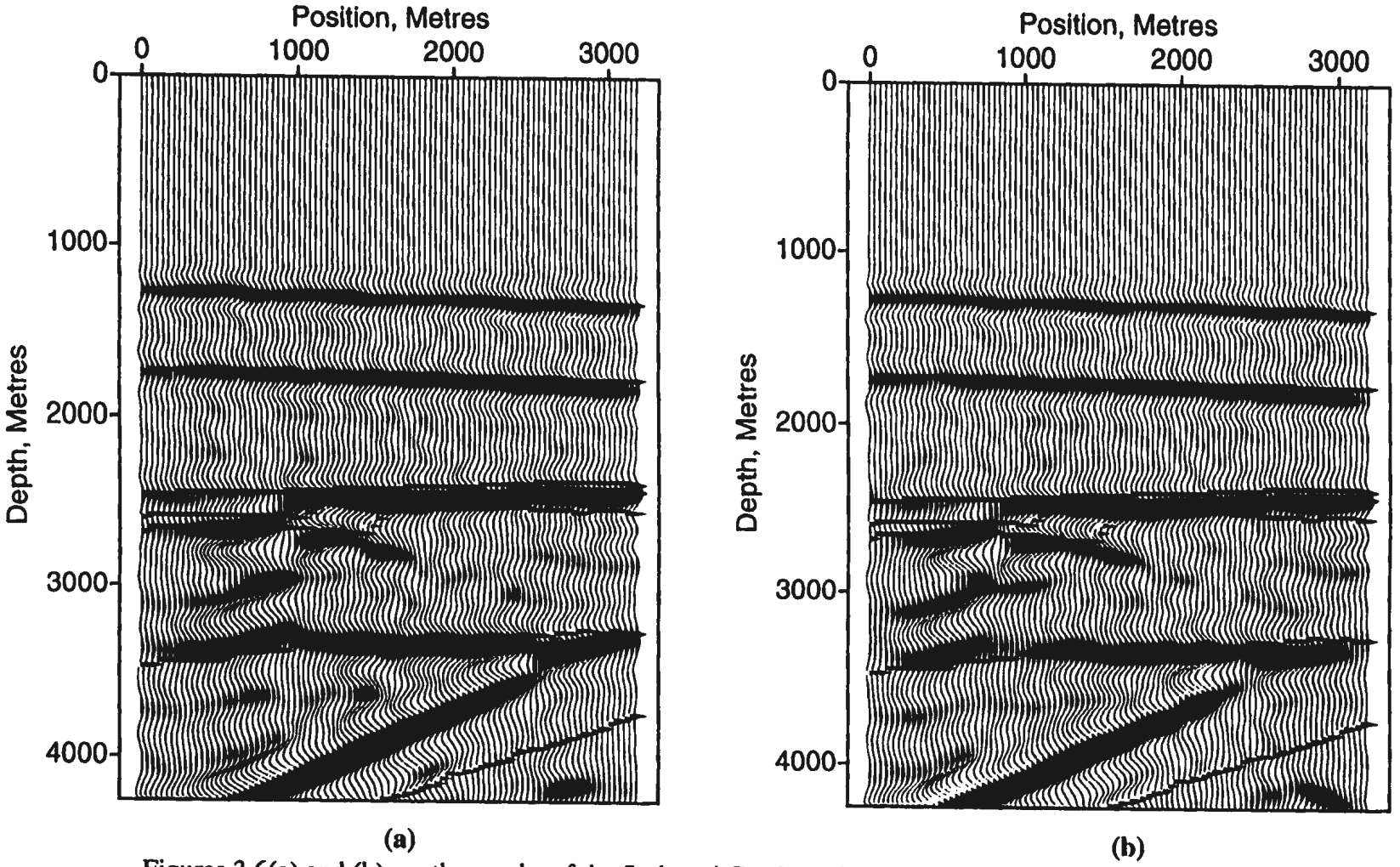

Figures 3.6(a) and (b) are the results of the Stolt and Gazdag migrations of inline 60 after conversion to depth to allow for comparison with the reverse-time migrations. The layers are the Base of Tertiary unconformity, Petrel Member, Ben Nevis Formation, Avalon Formation, A Marker Member, Catalina Member, and the Lower Hibernia Formation.

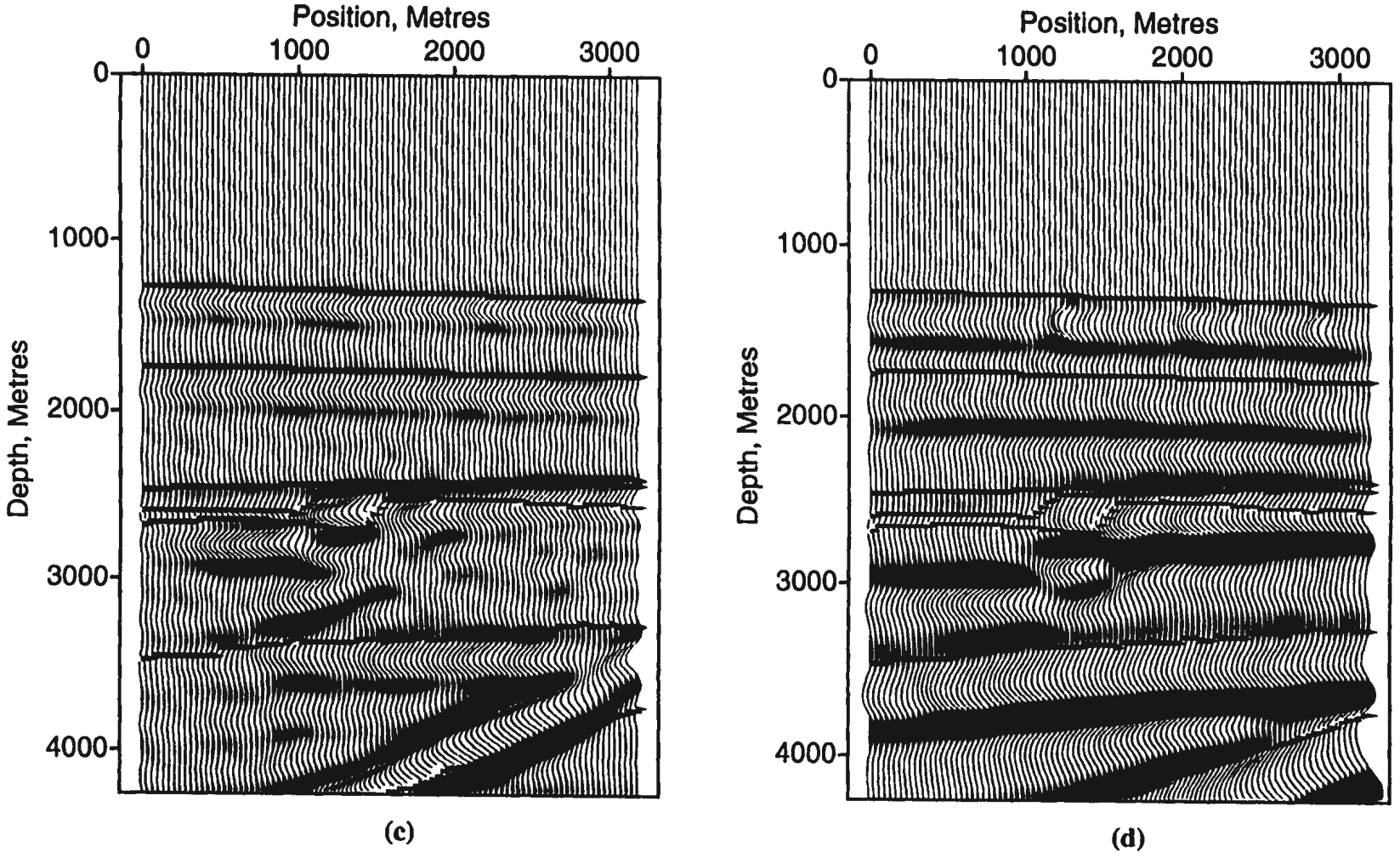

Figures 3.6(c) and (d) are the results of the 2-D and 3-D reverse-time migrations of inline 60, respectively. The 3-D migration provides a better image of the Hibernia Formation and the Murre fault.

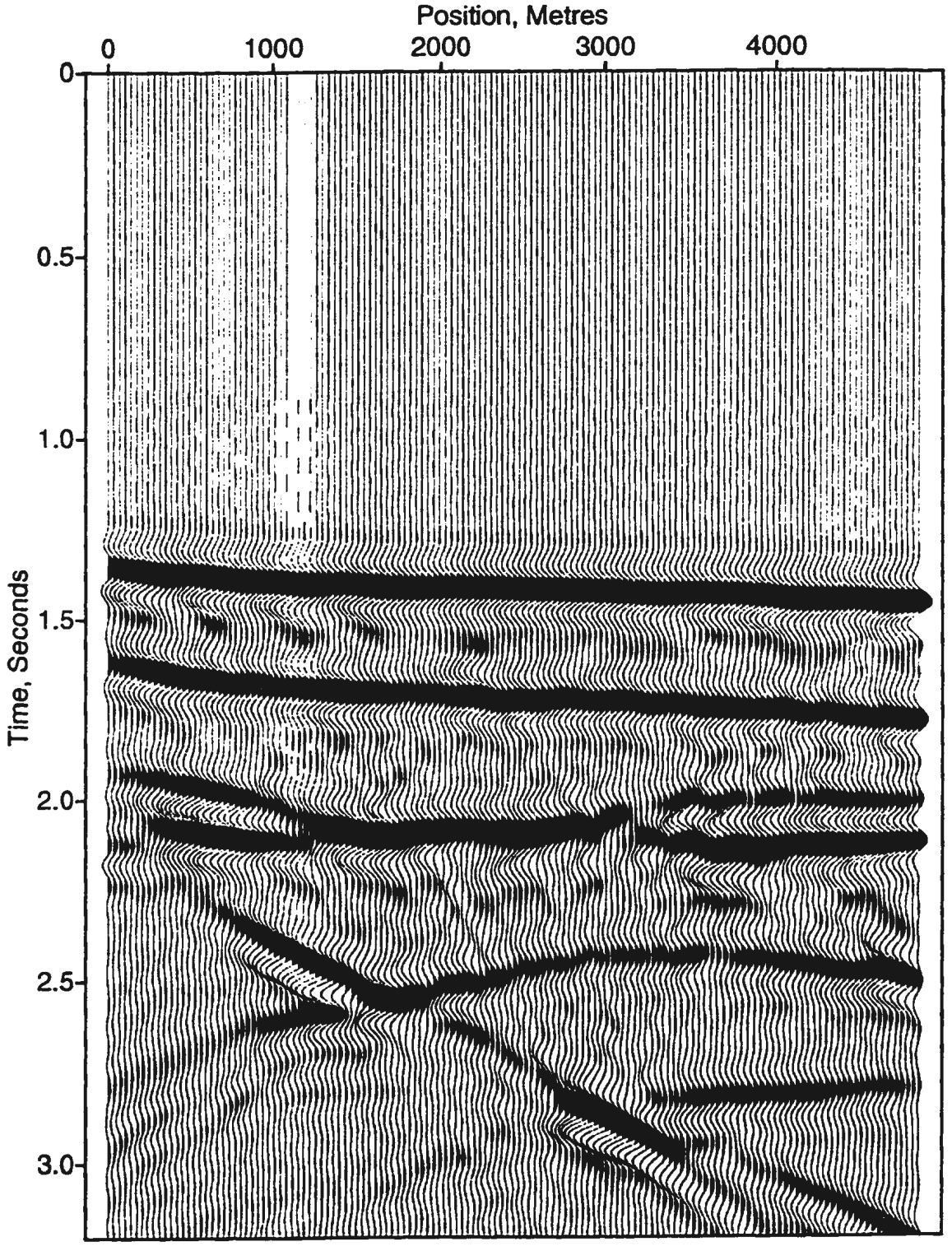

Figure 3.7 shows the synthetic seismic data for crossline 60 from the seven layer Hibernia model.

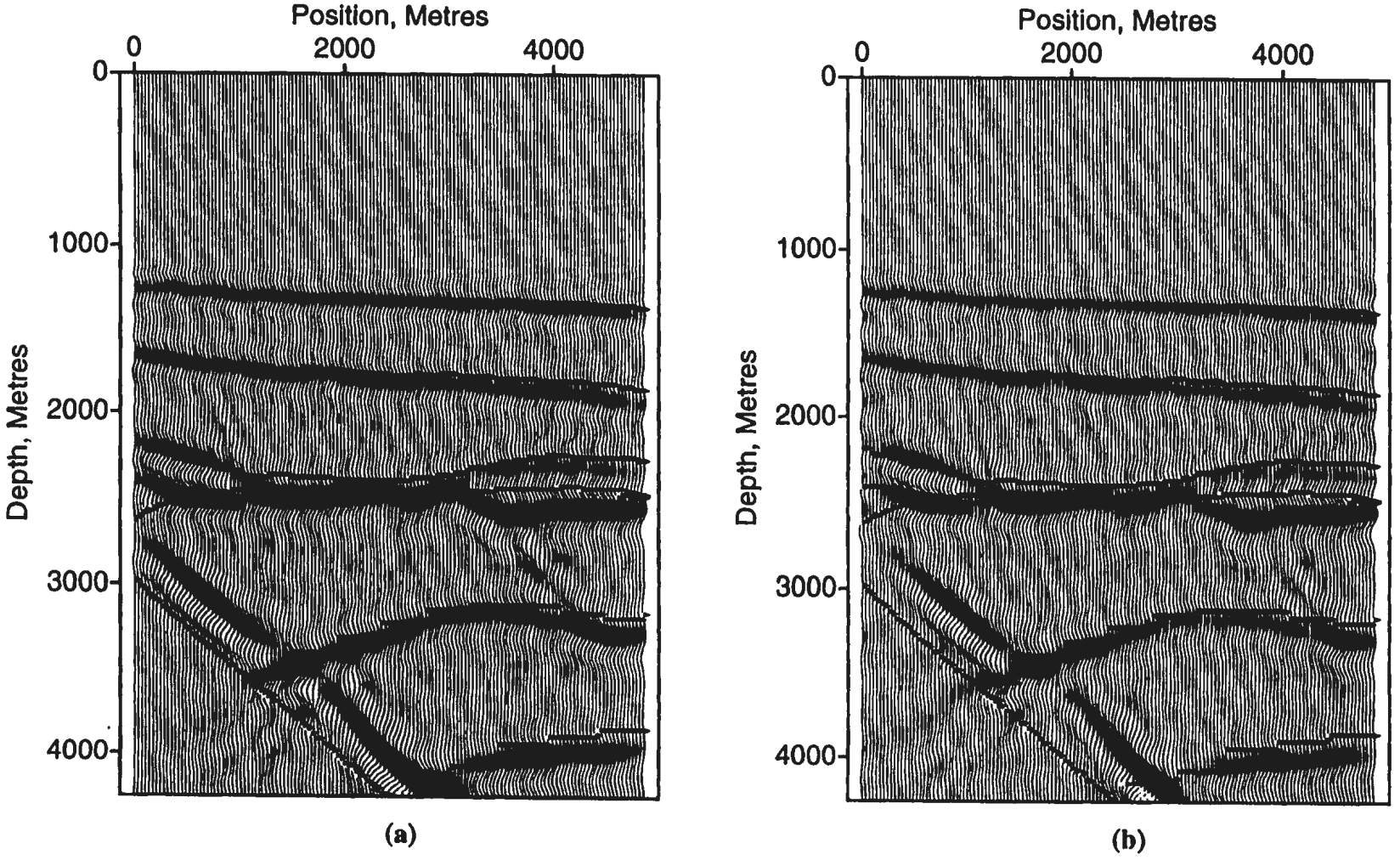

Figures 3.8(a) and (b) are the results of the Stolt and Gazdag migrations of crossline 60 after conversion to depth to allow for comparison with the reverse-time migrations. The Murre fault is not placed at the correct depth location for this section.

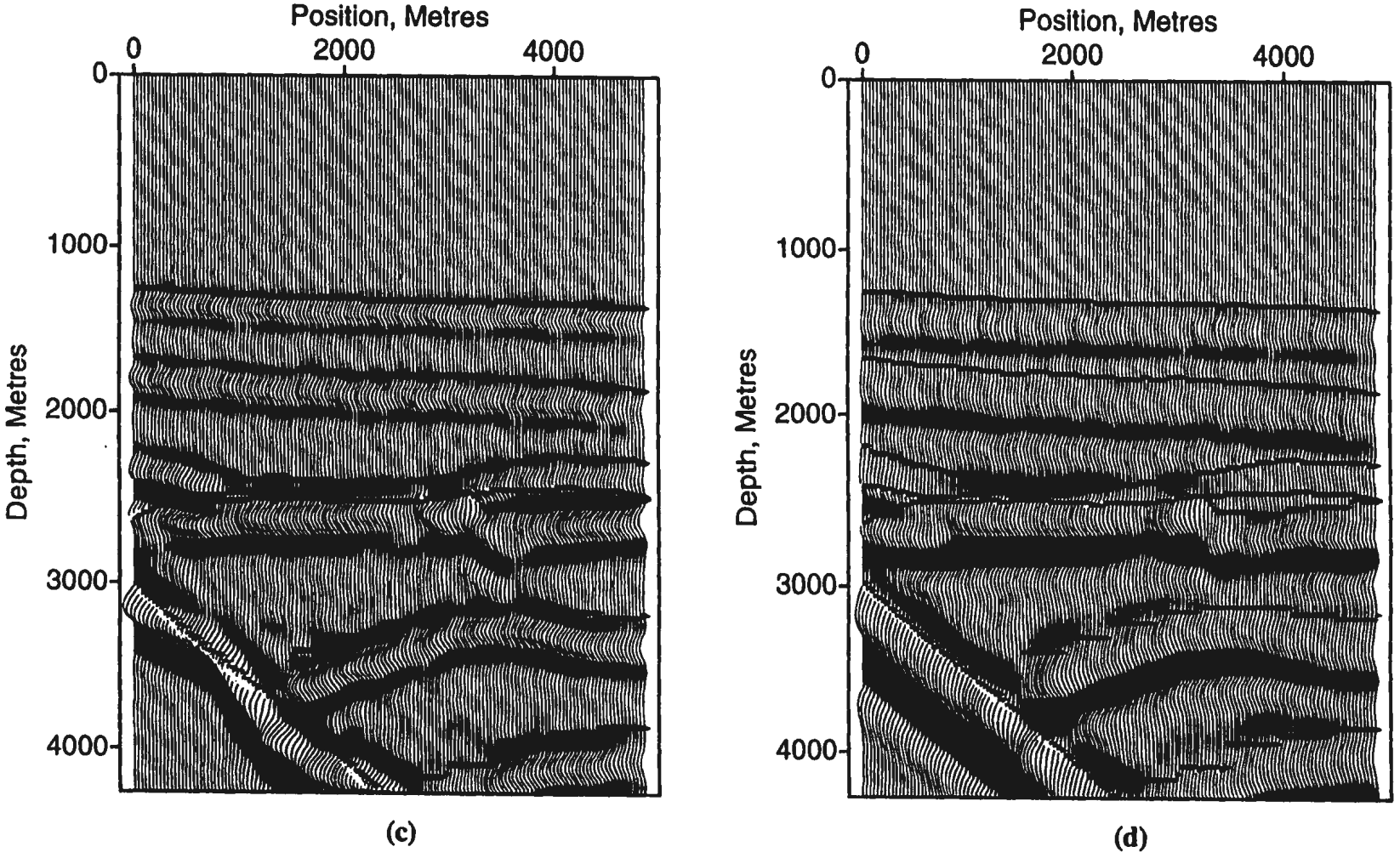

Figures 3.8(c) and (d) are the results of the 2-D and 3-D reverse-time migrations of crossline 60, respectively. The 3-D migration provides a slightly better image of the shape of the fault.

image due to out-of-plane reflection energy. In such cases, a 3-D migration is required to accurately position the out-of-plane energy.

3.3. Poststack migration of Hibernia seismic data

A subset of the 3-D seismic dataset from the 1991 survey of the Hibernia field was chosen as the test area for the migration algorithms. This area is the rectangle outlined in figure 3.9, and was chosen because it overlays the model area. Inlines in this survey run 26/206 degrees and crosslines run perpendicular to this. The lines within the area of interest have been numbered so that the first inline is on the right side of the rectangle, and the first crossline is at the top of the rectangle. The dataset consists of 310 inlines and 270 crosslines of stacked seismic data at a 25 m spacing. The 2-D migration algorithms were used on several inlines and crosslines and the results will be shown for inline 170 and crossline 210. Figure 3.10 is the seismic data for inline 170, and figures 3.11(a) and (b) are the results of the Stolt and phase-shift migrations, respectively, after conversion to depth. Figure 3.11 (c) is the result of the 2-D reverse-time migration of inline 170 using a single $v(z)$ velocity function. This function contains the same interval velocities as were used in the $v(t)$ function supplied to the phase-shift migration. The results show that the Stolt migration has not fully collapsed all of the diffractions, and there is still crossover of some of the reflections. The phase-shift and reverse-time migrations produce similar quality images, but the reverse-time migration has a lower frequency content due to the application of a pre-migration bandpass filter of 10/15-35/40 Hz. The filter was applied to reduce the

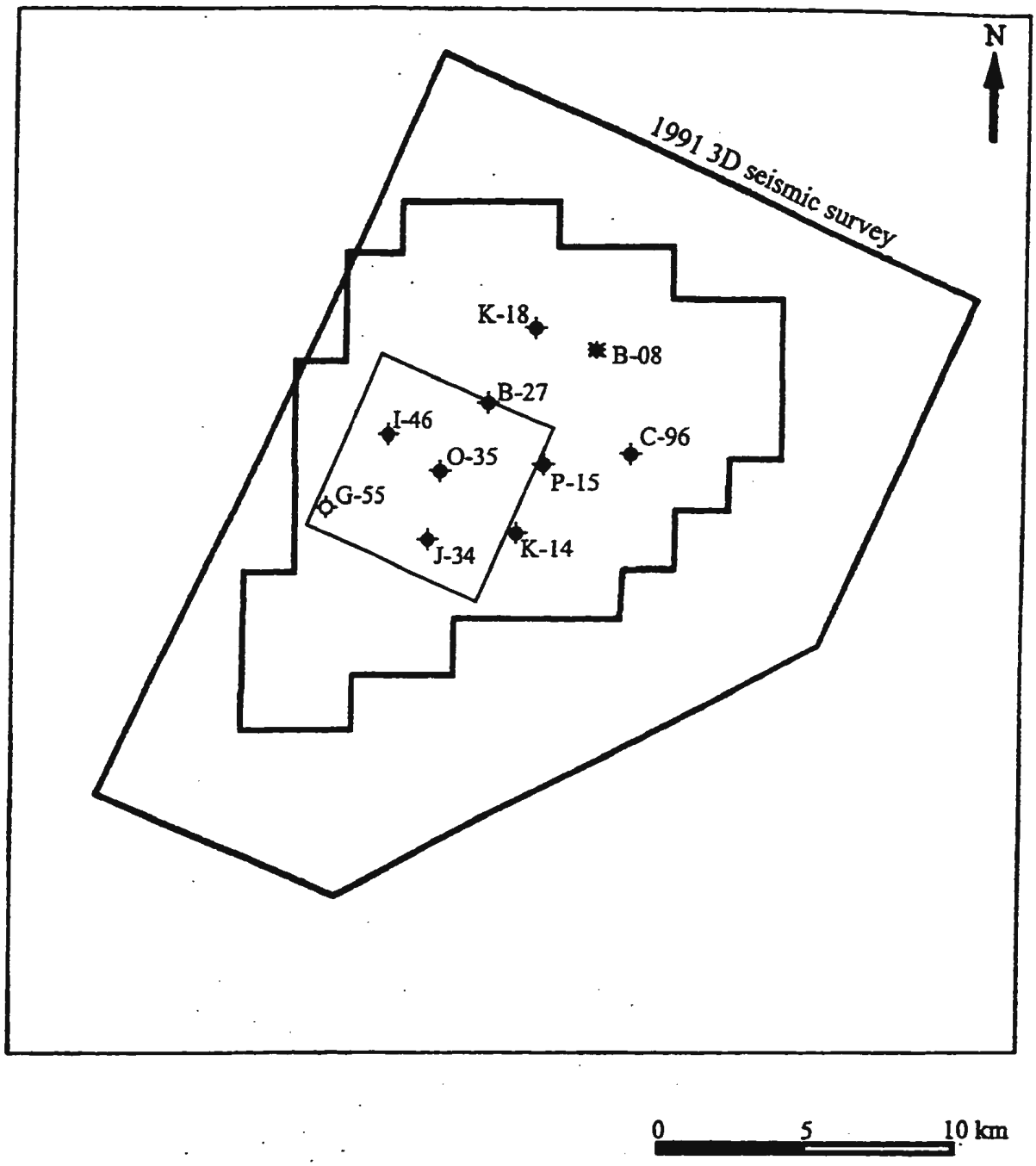

Figure 3.9. The migration area of interest from the 1991 3-D seismic survey is outlined by the small rectangle. This figure was adapted from one provided by the Hibernia Management and Development Company.

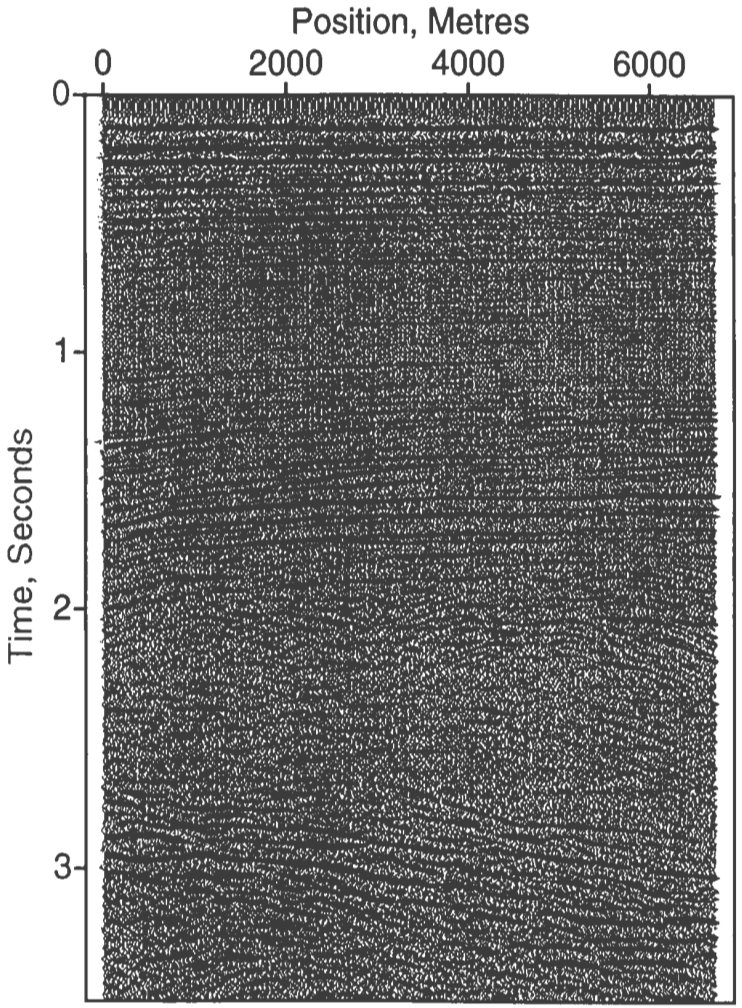

Figure 3.10 is the stacked seismic data for inline 170.

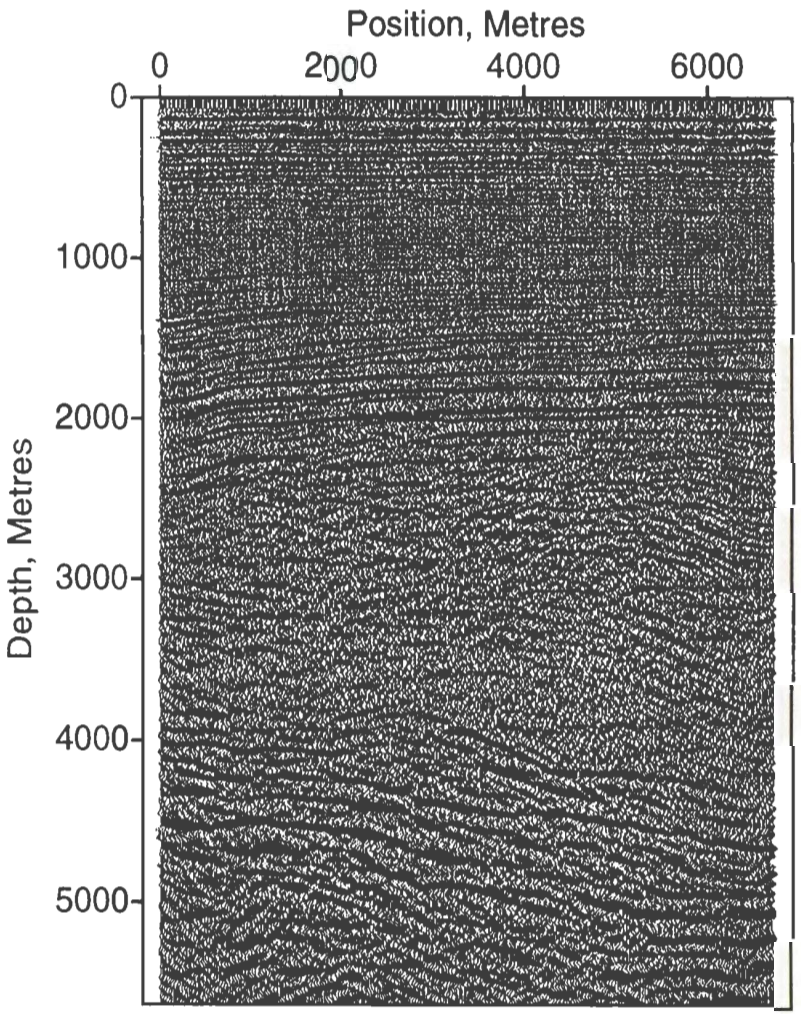

(a)

Figure 3.11(a) is the result of the Stolt migration after conversion to depth.

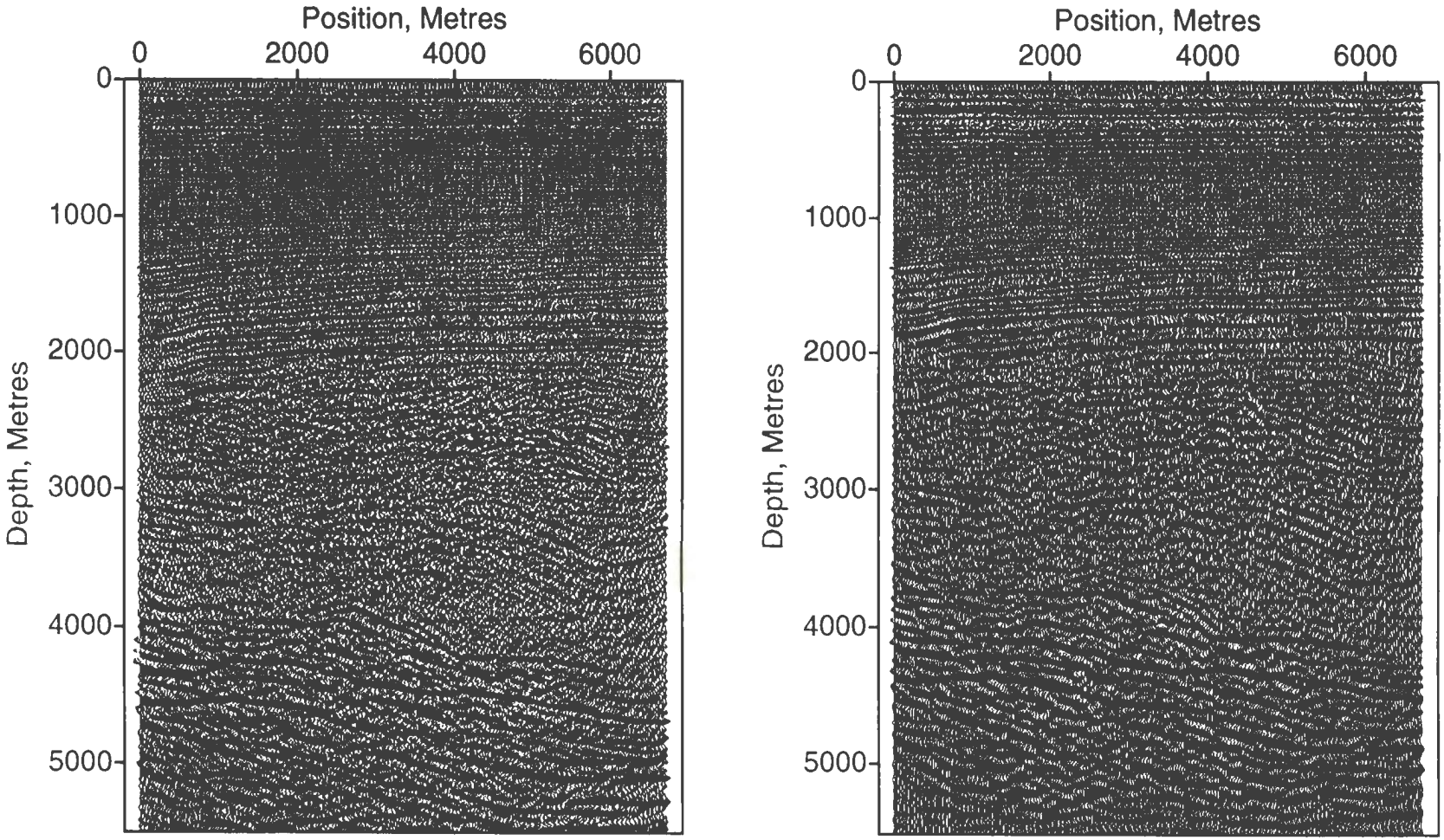

Figures 3.11(b) and (c) are the results of the phase-shift and reverse-time migrations of inline 170, respectively. The migrations produce very similar images, but the reverse-time migration requires a much greater cpu time.

runtime of the migration.

Figures 3.12 and 3.13(a) - (c) show the same plots for crossline 210, with the Stolt migration resulting in the worst image. The diffractions have not been fully collapsed and the rollover of the sediments into the fault has been very poorly imaged. Figures 3.13(b) and (c) are the results of the phase-shift and reverse-time migrations, and the results are quite similar. The rollover is well-imaged in both sections, but the fault is better imaged in the reverse-time migration. The top of the fault is more correctly imaged by the reverse-time migration, which places it at a depth of approximately 2500 m. The phase-shift migration places the top of the fault at approximately 3000 m.

A subset of the migration test area consisting of 150 inlines and 150 crosslines from the lower left corner of the survey, in the area of the G-55 well, was used to compare 2-D and 3-D reverse-time migration. The minimum velocity used in the migration velocity model was 2035 m/s and the maximum velocity was 4850 m/s. The grid spacing and time sampling rate were calculated according to equations 1.7 and 1.8. These calculations produced a recommended grid spacing of 9.69 m and a time sampling rate of 0.001 ms. The 3-D velocity model required for the migration needs a 20 trace padding in all directions, and 400 depth samples would be needed to image the Avalon Formation. This meant that the total size of the model would be 387 X 387 X 400 samples if a uniform grid spacing of 9.69 m was used in the velocity model. A 3-D migration of this size would require months to complete on a Sparc 10 computer, and ideally requires a supercomputer.

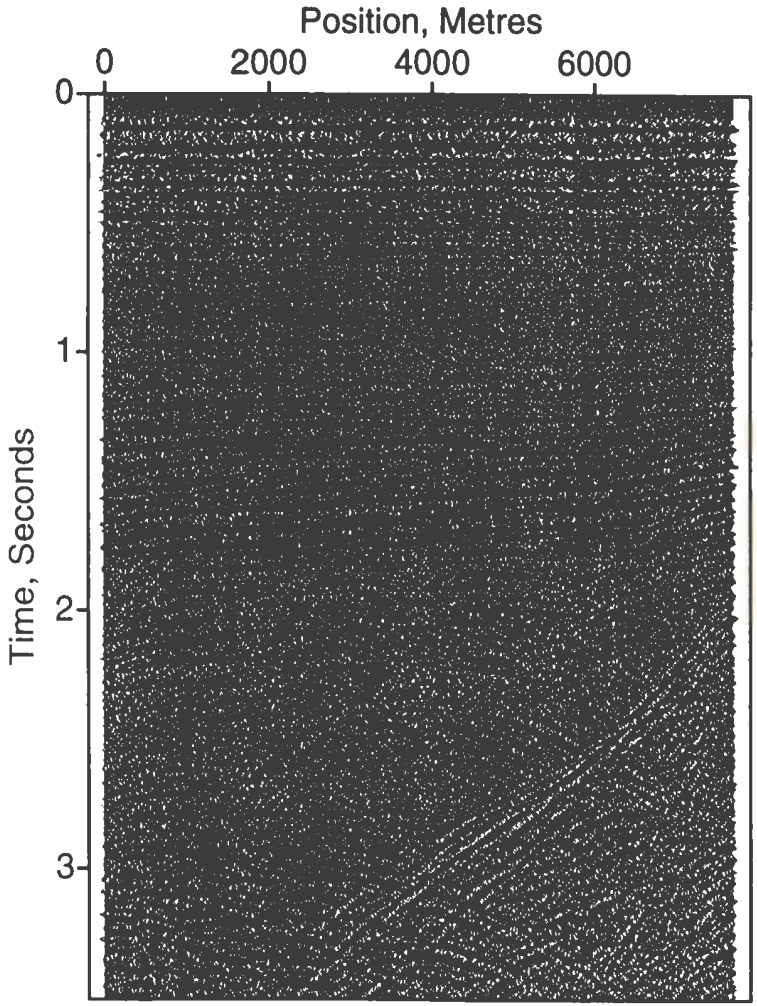

Figure 3.12 is the stacked seismic data for crossline 210.

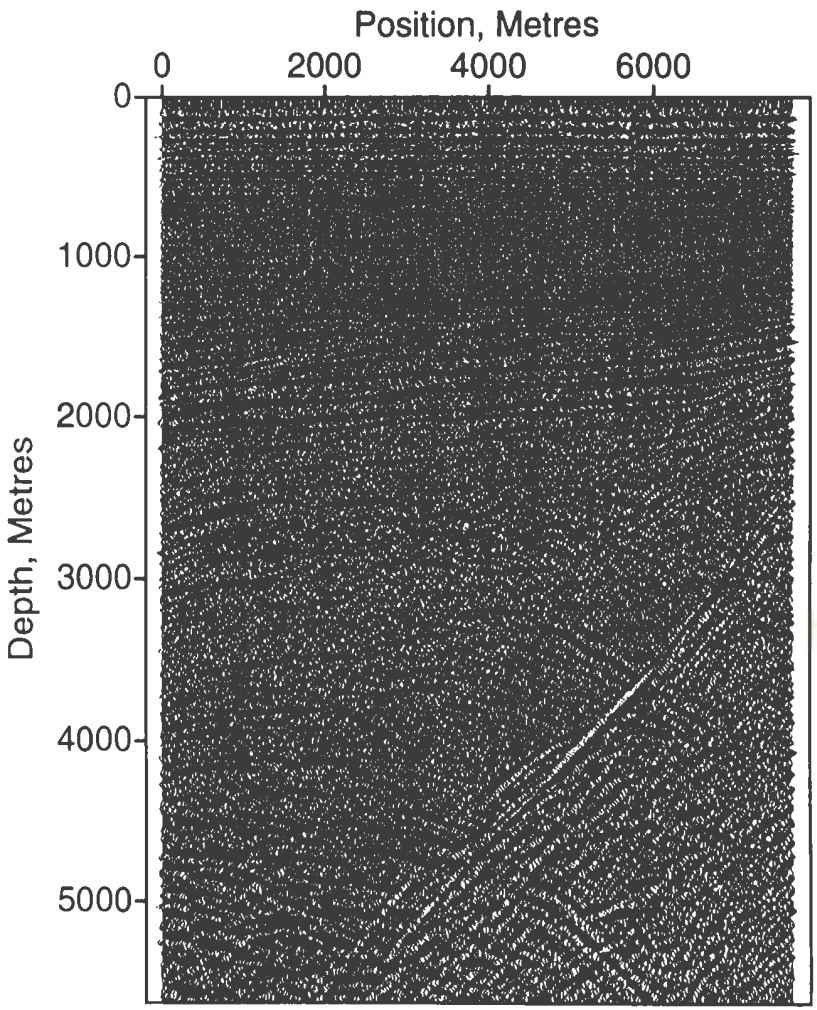

(a)

Figure 3.13(a) is the result of the Stolt migration after conversion to depth.

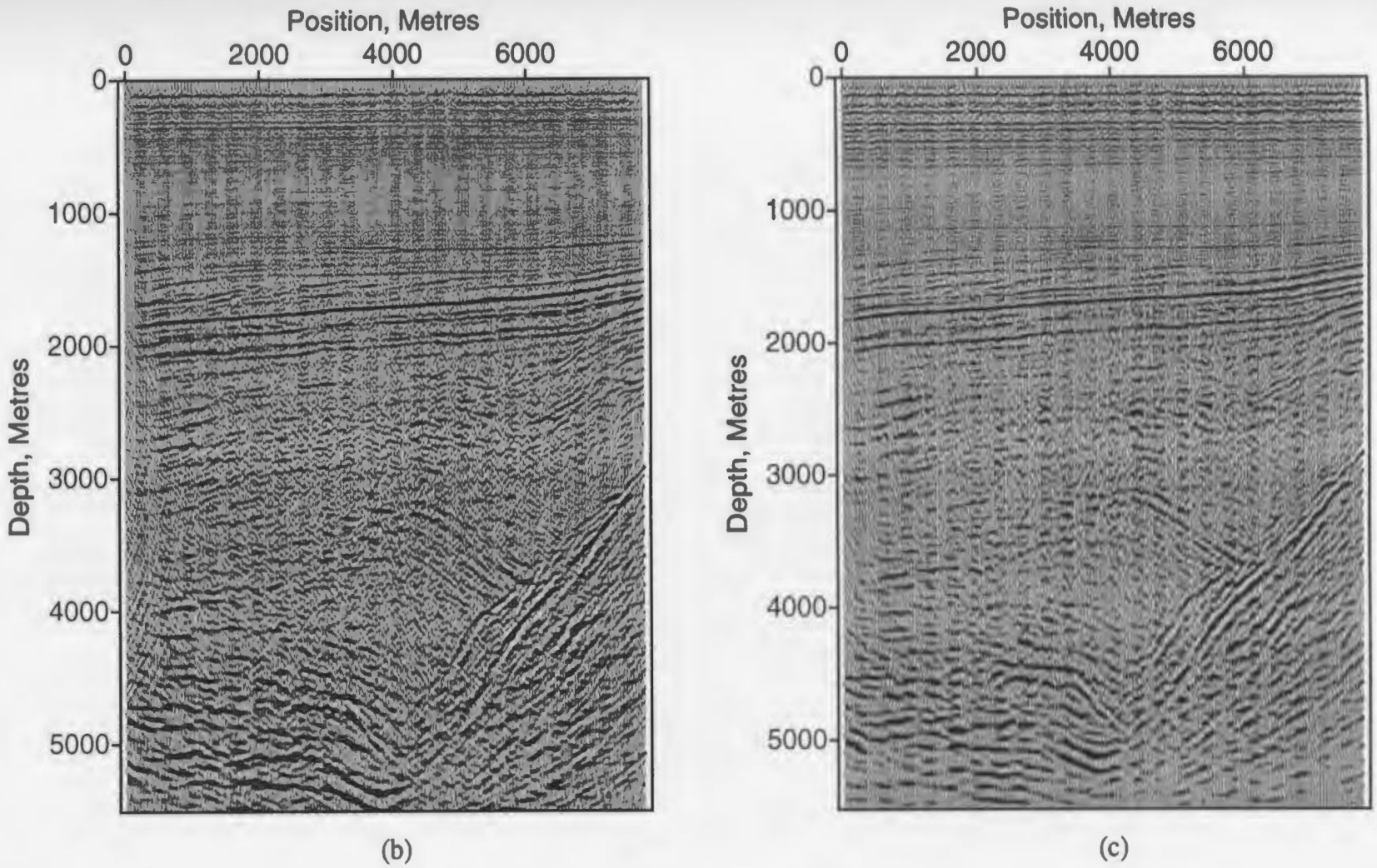

Figures 3.13(b) and (c) are the results of the phase-shift and reverse-time migrations of crossline 210, respectively. The rollover of the sediments into the fault is well-imaged by both migrations, but the reverse-time migration provides a better image of the fault.

In order to complete the 3-D migration in an acceptable amount of time, and to show the effects of using too coarse a grid spacing, the first 3-D migration of the Hibernia data was computed using the 25 m grid spacing in all directions. For comparison purposes, the 2-D reverse-time migration of inline 100 was also computed using the same coarse grid spacing. Figure 3.14(a) is the seismic data for inline 100, and figures 3.14(b) and (c) are the 2-D and 3-D migration results, respectively. These migrations are both unusable since they cannot provide a clear image below approximately 1500 m, but the 3-D migration provides a slightly better image than the 2-D migration. The 2-D migration completed in approximately 5 minutes, and the 3-D migration required about 2 days of wall clock time. Figure 3.15 shows the result of a 3-D migration of inline 100 using a finer grid spacing of 12.5 m in the z-direction. This migration required approximately 15 days of wall clock time to complete on a Sparc 10, and is still not up to the quality of the 2-D reverse-time migration using grid spacing which satisfies the dispersion conditions.

A comparison of 2-D and 3-D reverse-time migration for Hibernia seismic data using a fine grid size may be found in Wu et al. (1996). These migrations were computed using a grid spacing of 6.25 m in the x- and y- directions and 4.69 m in the z-direction. However, the total depth imaged by the migrations was only on the order of 2000 m in order to complete the migration in a reasonable amount of time. The results of the 2-D and 3-D migrations are displayed in figures 3.16(a) and (b), respectively. The erosional channel located at a depth of 1400 m and a distance of 1100-1300 m is much more clearly imaged by the 3-D migration.

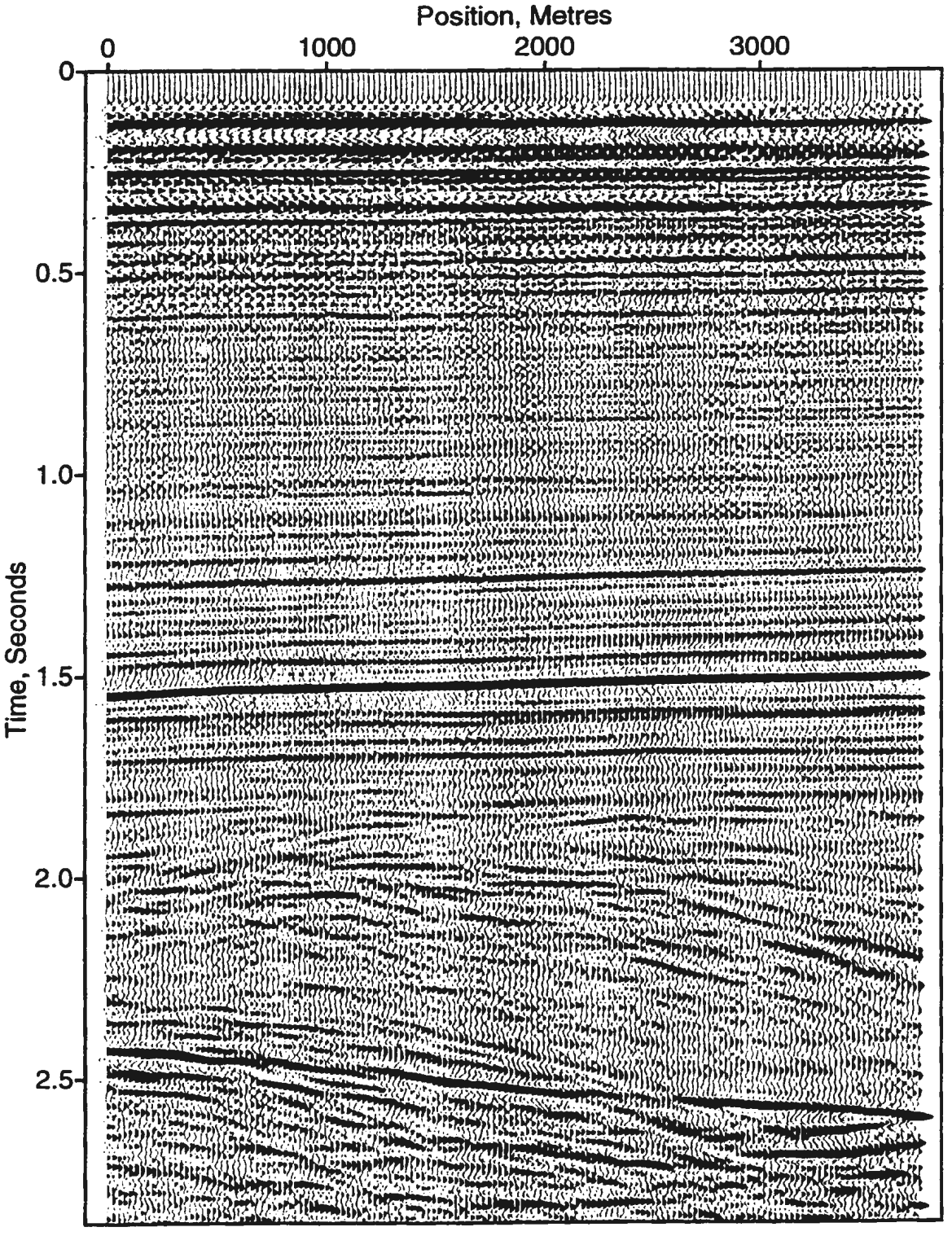

Figure 3.14(a) is the seismic data for inline 100 that is input to the migrations.

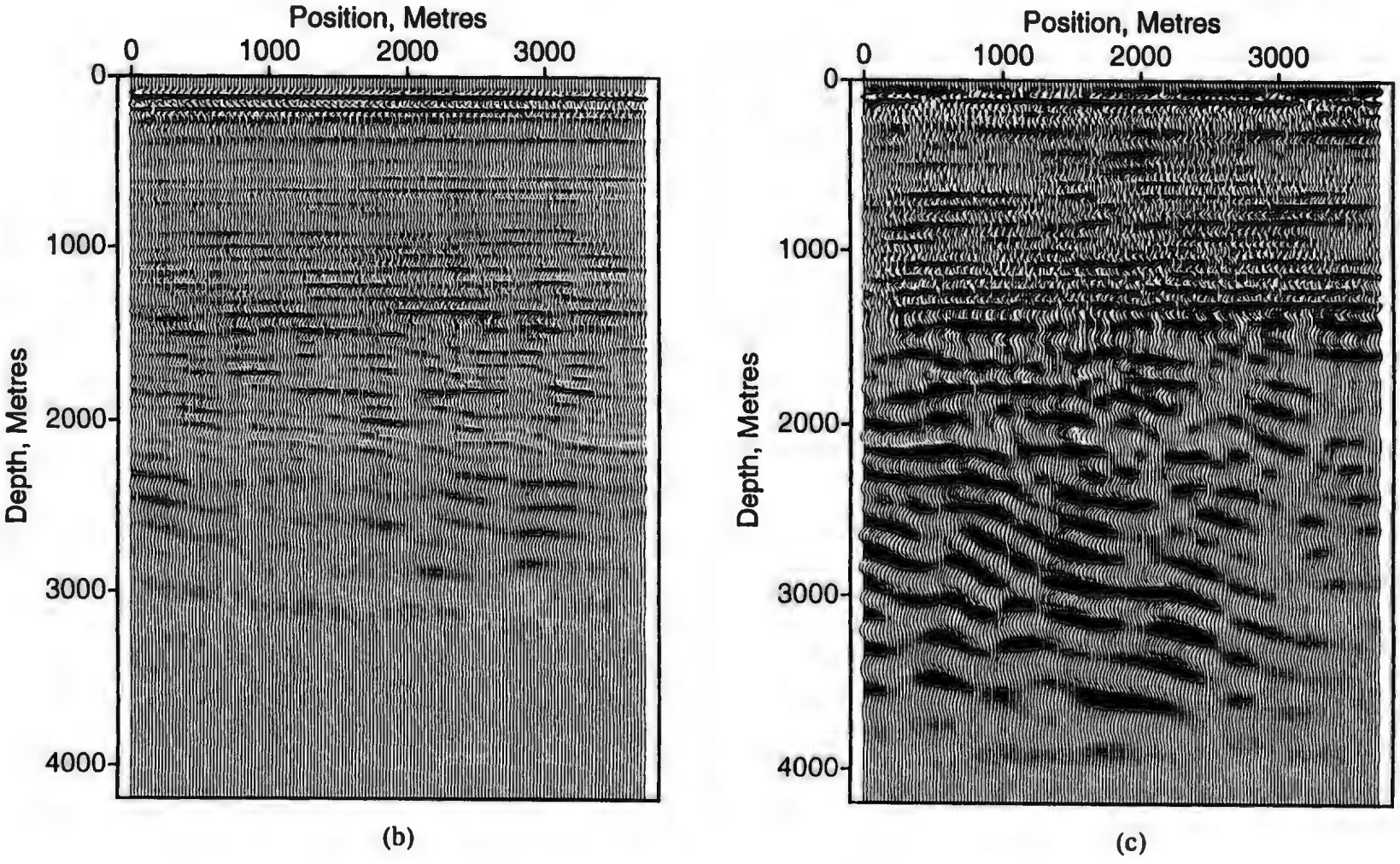

Figures 3.14(b) and (c) are the results of the 2-D and 3-D reverse-time migrations of inline 100 using the coarse grid spacing. The results are very poor, and do not provide a clear image below 1500 m.

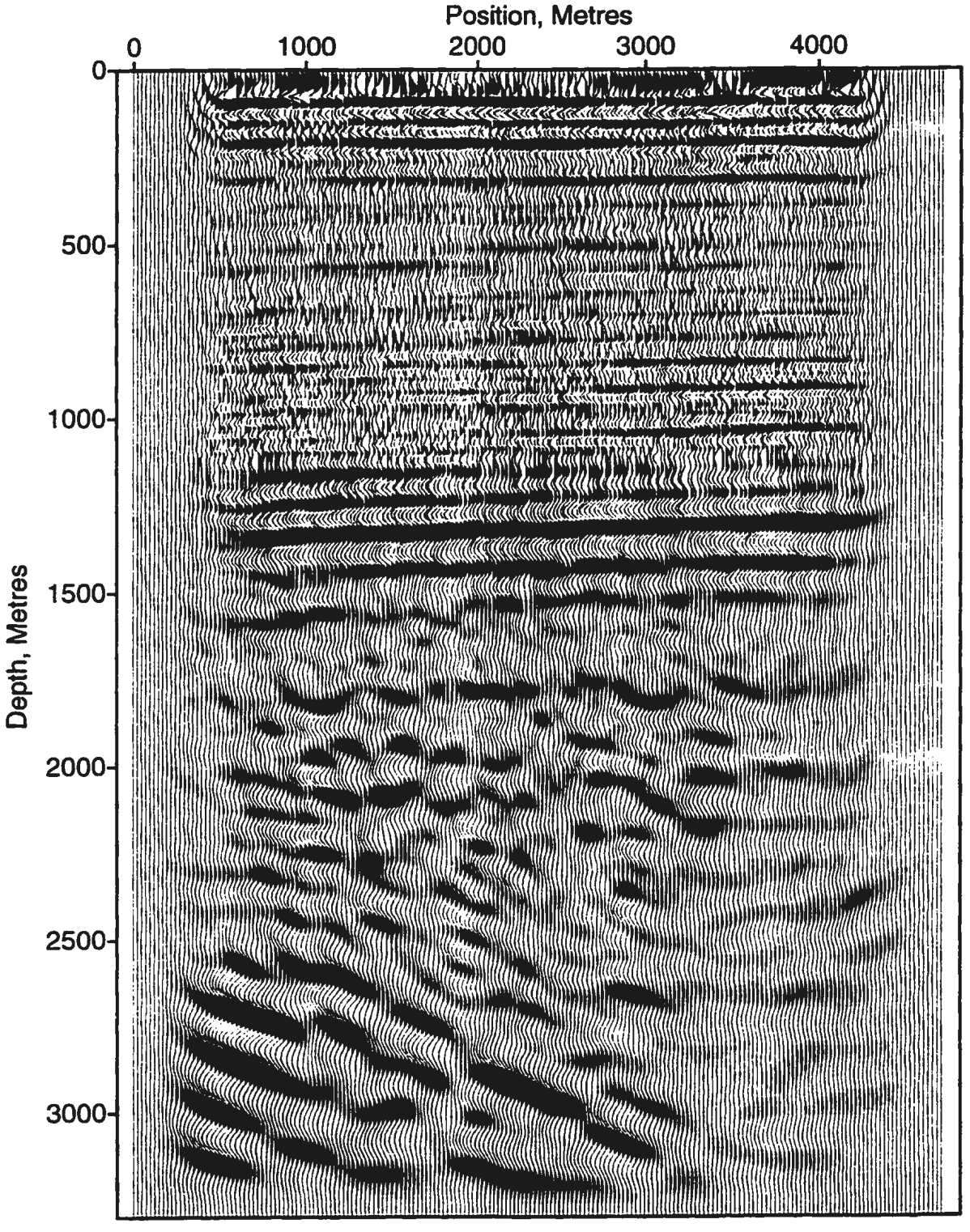

Figure 3.15 is the result of the 3-D reverse-time migration using a vertical grid spacing of 12.5 m and a horizontal grid spacing of 25 m.

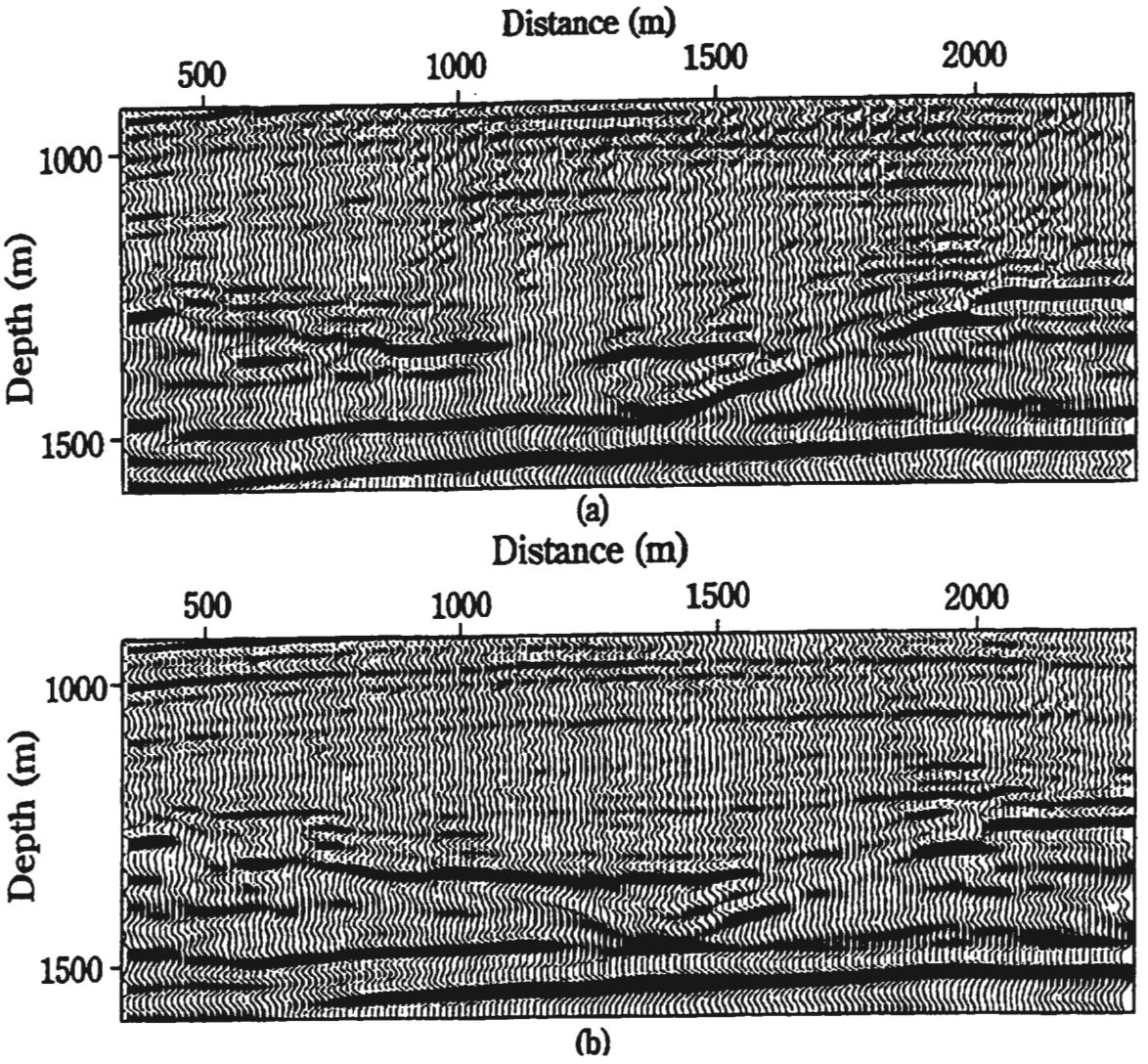

Figure 3.16(a) and (b) are the results of a 2-D and 3-D reverse-time migration for Hibernia seismic data taken from Wu et al. (1996). The 3-D migration obtains a much clearer image of the erosional channel located at position 1200 and depth 1400 m.

Chapter 4. Optimization of Poststack migration

4.1. Sensitivity of poststack migration to input velocities

Poststack migration algorithms may output the migrated seismic section as either a time or depth section depending upon which migration algorithm is chosen. An input velocity model is required to correctly migrate the seismic data regardless of which migration algorithm is being used, and a velocity model will eventually be required to convert migrated time sections into depth sections suitable for determining possible hydrocarbon traps and well locations. The velocity model input to the migration may be determined from a variety of sources such as sonic logs, checkshots, vertical seismic profiles (VSPs), normal moveout analysis (NMO), tomography, or iterative prestack migration. Iterative prestack migration is expensive, and velocity information derived from wells is limited in quantity and field coverage. Recent work by Bickel (1990), Lines(1993a), and Versteeg (1995) document the difficulties involved in obtaining an accurate estimate of the interval velocities needed for poststack migration using methods such as NMO analysis and traveltime tomography.

Conventional methods of velocity estimation, such as normal moveout analysis for the stacking velocities, often fail because of violation of the assumptions inherent to these techniques (Bickel, 1990). Estimating the interval velocities from the stacking velocities requires assuming that the layer is homogeneous and the velocity of the layer is laterally invariant. Violations of this assumption can cause stacking velocity

estimates to vary dramatically from the average. Velocity errors on the order of 5 to 10 per cent may exist due to the resolution limit of the process used to estimate stacking velocities. Lines (1993a) shows that ambiguity in velocity estimates for traveltime tomography is a function of the fractional error in traveltime picking and the offset-depth ratio. Versteeg (1995) separates the error in depth estimation into a component which is due to the migration scheme and one which is a function of the seismic data - its offset, velocity, reflector depth, wavelet frequency, picking accuracy, and attenuation.

It is difficult to control the accuracy of the velocity model input to migration, since many of the factors affecting velocity accuracy (earth properties, acquisition geometry, etc.) are outside of the geophysicist's control at this point in the seismic processing scheme. The purpose of this velocity sensitivity analysis of poststack migration was to determine the effect that known errors in the velocity model have on the migration results. This was done using the synthetic seismic data generated from the Hibernia models, and the fact that the correct interval velocities are known for these models. Specific levels of error were introduced into the velocity models used in the migration scheme, and the fractional discrepancies between the actual model depths and the migrated depths were then calculated. Most of the errors were chosen to be between 5 to 10 per cent since this level of error is very easily introduced by the resolution limit of the process for estimating stacking velocities. The effects of these errors on the migration depths of the reflectors will be shown, and any other sources of migration velocity error will only increase the migration depth errors.

$$\delta_{i,j} = \frac{|M_{i,j} - m_{i,j}|}{M_{i,j}} \tag{4.1}$$

$$i = 1.2.....I \ (trace\ index) \tag{4.2}$$

$$j = 1.2.....J \ (sample\ index)$$

Here, $M_{i,j}$ is the actual model depth for a sample (i, j), $m_{i,j}$ is the migrated depth, I is the total number of traces in the seismic section, and J is the number of layers for which to calculate error plots. The sum of fractional discrepancies,

$$P = \sum_{i=1}^{I} \sum_{j=1}^{J} \delta_{i,j}. \tag{4.3}$$

must be minimized to obtain a good match between the migrated data and the original model layers. The depth errors due to errors in the velocity model must then be compared to the depth errors that are inherent to the migration scheme and are obtained even with the correct velocity model.

The 2-D reverse-time migration algorithm was used in this sensitivity analysis of the effect of errors in the velocity model on the migration results, since it is the most general and accurate technique of those under consideration. The 2-D reverse-time migration requires an input $v(x, z)$ velocity model that may easily be adjusted to allow specific levels of error to be introduced into different layers. The use of the 2-D reverse-time migration, in conjunction with the model data, allowed the creation of a velocity model which has the correct depth and shape for all layers, but has the wrong velocity between layers.

Crossline 30 from both the three and seven layer Hibernia models was chosen as

a test line for the velocity error analysis. Velocity errors as indicated in Table 4.1 were introduced into the top three layers in the first model. The v1 velocity model contained a velocity that was 10 per cent too high in the shallowest layer, while all other velocities were correct. The v2 model contained the error in the first velocity, as well as a velocity that was 5 per cent too low in the next deepest layer. The v3 model contained the first two errors, as well as a velocity that was 5 per cent too high in the third layer. These three velocity models were then used to migrate the seismic data using a 2-D reverse-time migration algorithm.

Table 4.1: Velocity models containing errors

Model	Layer	Correct velocity	Error Introduced	New Velocity
v1	1	2221 m/s	10 per cent too high	2443 m/s
v2	1	2221 m/s	10 per cent too high	2443 m/s
	2	3566 m/s	5 per cent too low	3388 m/s
v3	1	2221 m/s	10 per cent too high	2443 m/s
	2	3566 m/s	5 per cent too low	3388 m/s
	3	4105 m/s	5 per cent too high	4310 m/s

The migration results using the original velocity model and the three new velocity models were compared to the actual depths of the layers as defined in the original model. The top of each layer in the migrated section was picked on the number of traces on which it was identifiable, and each top was then used to calculate the average fractional discrepancy over that number of traces for a particular layer. Figures 4.1(a) - 4.1(d) show the migration results using each of the velocity models for crossline 30.

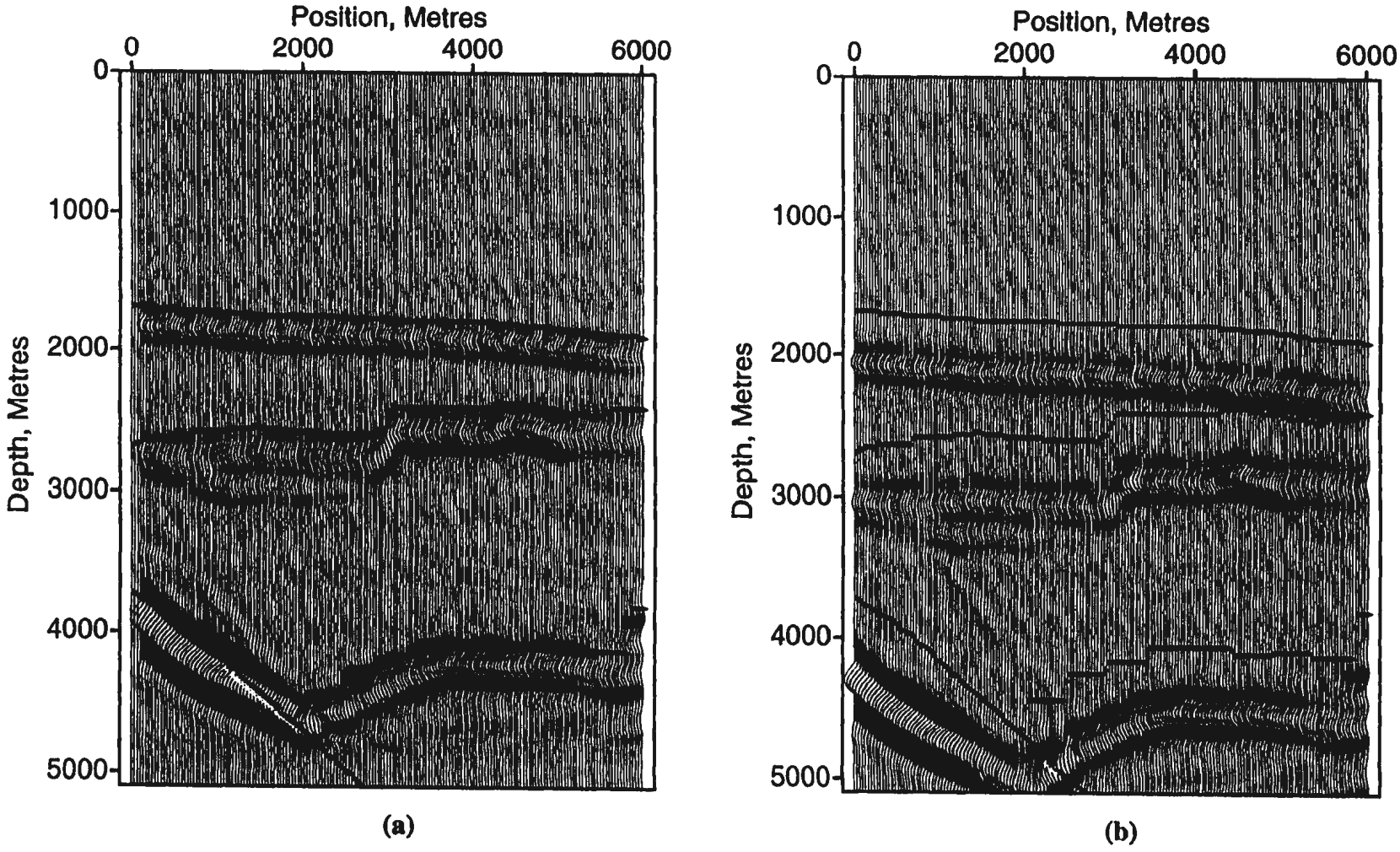

Figure 4.1(a) is the result of the 2-D reverse-time migration of crossline 30 with the correct velocity model. Figure 4.1(b) is the result of the 2-D reverse-time migration of crossline 30 using the v1 velocity model. The shapes of the migrated layers are correct, but the velocity errors have introduced depth errors.

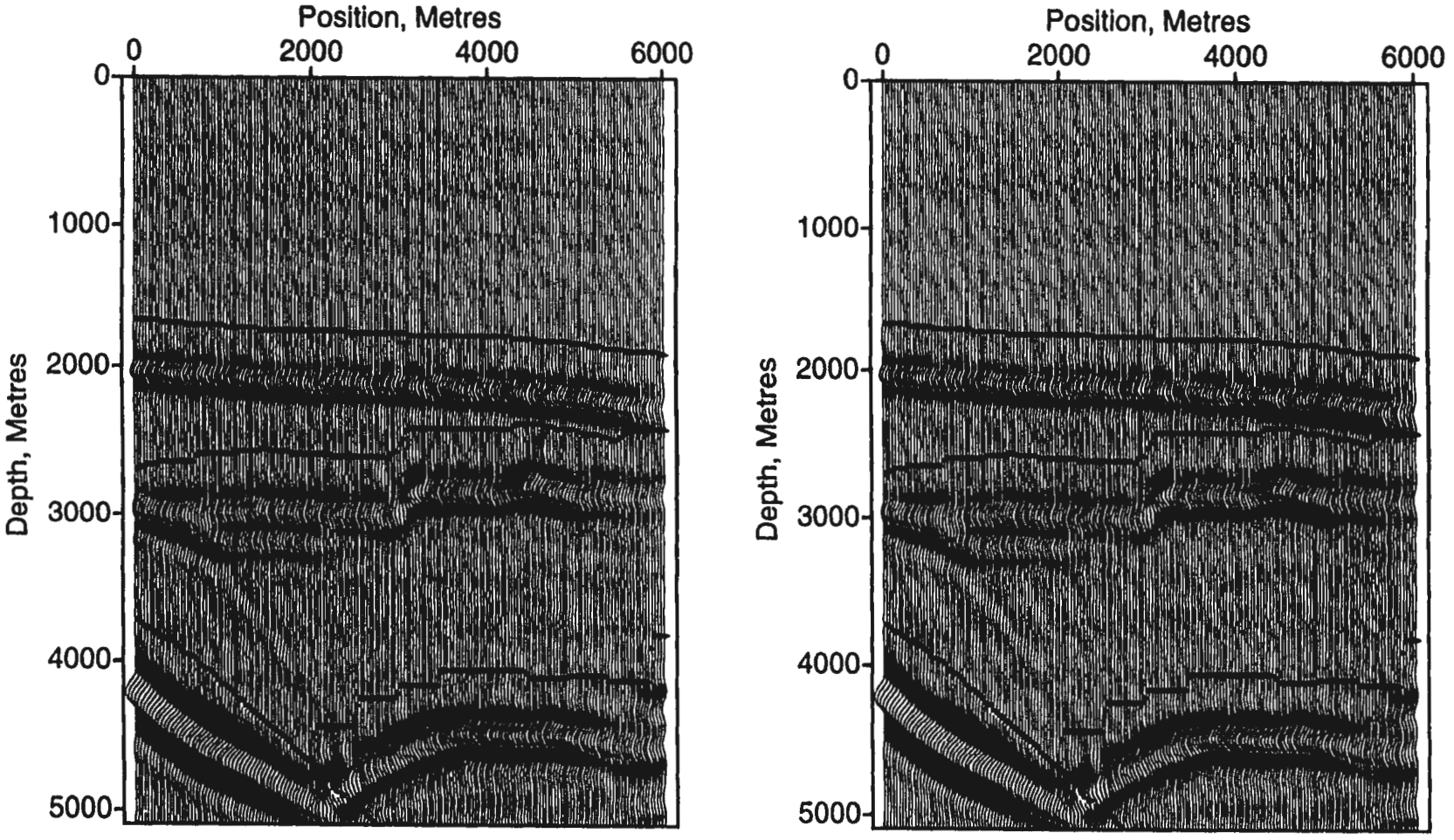

Figure 4.1(c) is the result of the 2-D reverse-time migration of crossline 30 using the v2 velocity model. Figure 4.1(d) is the result of the 2-D reverse-time migration of crossline 30 using the v3 velocity model. A small velocity error in a thick layer may cause a greater depth error than a large velocity error in a thin layer.

and table 4.2 contains the average fractional discrepancies from the depth comparison. The Murre fault was one of the layers used in this analysis, since figure 4.1(a) shows that this line is one of the lines for which the Murre fault may be correctly positioned using a 2-D migration technique. Analysis of the migration results show that using too high a velocity in a shallow layer may be partially compensated for by using too low a velocity in a deeper layer. This idea will be explored further using crossline 30 from the seven layer Hibernia model, where it will be shown that it is possible to obtain a correct migration depth for a layer using a combination of velocities which are not appropriate for this model.

Table 4.3 shows the velocity errors which were present in each of five different velocity models that were used in 2-D reverse-time migrations of crossline 30 from the seven layer model. The first model contained a velocity that was 5 per cent too low in the shallowest layer. The second velocity model was designed so that the error in the second layer would compensate for the error in the first layer, and all deeper layers in the model would therefore be placed at their correct locations. The first layer is quite large, averaging 1350 m in thickness, and requires that the thinner second layer have a velocity that was 34 per cent too high in order to maintain the same average velocity at the base of the second layer. The third velocity model contained a velocity that was 10 per cent too high in the third layer, and the fourth model tried to compensate for this error in deeper regions by using a velocity that was 8 per cent too low in the sixth layer. The fifth model had a velocity that was 5 per cent too high in the seventh layer.

Table 4.2: Average fractional discrepancies for crossline 30

Velocity model	Layer	No. of traces	Average fractional discrepancy
original	Petrel	166	0.0243657
	Aan7	170	0.0175108
	Hibernia	110	0.0136982
	Murre	57	0.0228400
Model v1	Petrel	169	0.0925046
	Aan7	165	0.0740670
	Hibernia	96	0.0416703
	Murre	79	0.0366080
Model v2	Petrel	174	0.0881588
	Aan7	170	0.0622835
	Hibernia	105	0.0375185
	Murre	83	0.0239224
Model v3	Petrel	169	0.0853421
	Aan7	171	0.0633210
	Hibernia	95	0.0320753
	Murre	73	0.0227504

Figures 4.2(a) - 4.2(f) contain the migration results for crossline 30, and table 4.4 shows the resulting average fractional discrepancy in the migration depths for the Base of Tertiary, Petrel, Ekt3, Catalina, and Hibernia horizons, as well as the Murre fault. This study shows that the picking accuracy of the layers from the migration

Table 4.3: Velocity models containing errors

Model	Layer	Correct Velocity	Error Introduced	New Velocity
v1	1	2035 m/s	5 per cent too low	1933 m/s
v2	1	2035 m/s	5 per cent too low	1933 m/s
	2	3009 m/s	34 per cent too high	4034 m/s
v3	1	2035 m/s	5 per cent too low	1933 m/s
	2	3009 m/s	34 per cent too high	4034 m/s
	3	3548 m/s	10 per cent too high	3903 m/s
v4	1	2035 m/s	5 per cent too low	1933 m/s
	2	3009 m/s	34 per cent too high	4034 m/s
	3	3548 m/s	10 per cent too high	3903 m/s
	6	4008 m/s	8 per cent too low	3687 m/s
v5	1	2035 m/s	5 per cent too low	1933 m/s
	2	3009 m/s	34 per cent too high	4034 m/s
	3	3548 m/s	10 per cent too high	3903 m/s
	6	4008 m/s	8 per cent too low	3687 m/s
	7	4320 m/s	5 per cent too high	4536 m/s

results is on the order of 1.0 per cent, while the migration results from models two and four show that it is possible to obtain accurate layer depths for the deeper layers when using incorrect velocity models. This illustrates the non-unique nature of the role of velocities in migration, in which mathematically accurate solutions may be found which do not fit the true physical nature of the model.

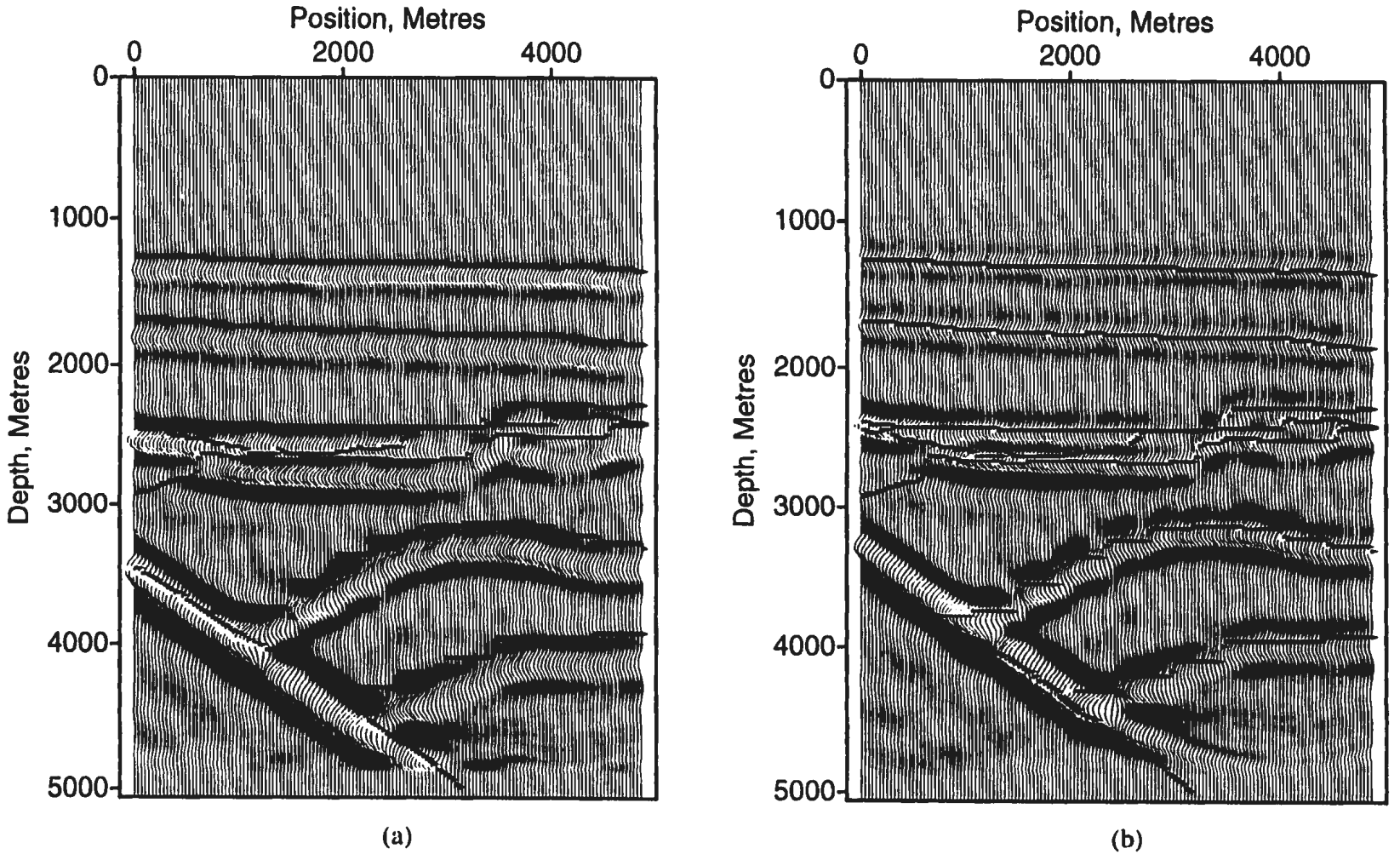

Figure 4.2(a) is the result of the 2-D reverse-time migration of crossline 30 using the correct velocity model. Figure 4.2(b) is the result of the 2-D reverse-time migration of crossline 30 using the v1 velocity model.

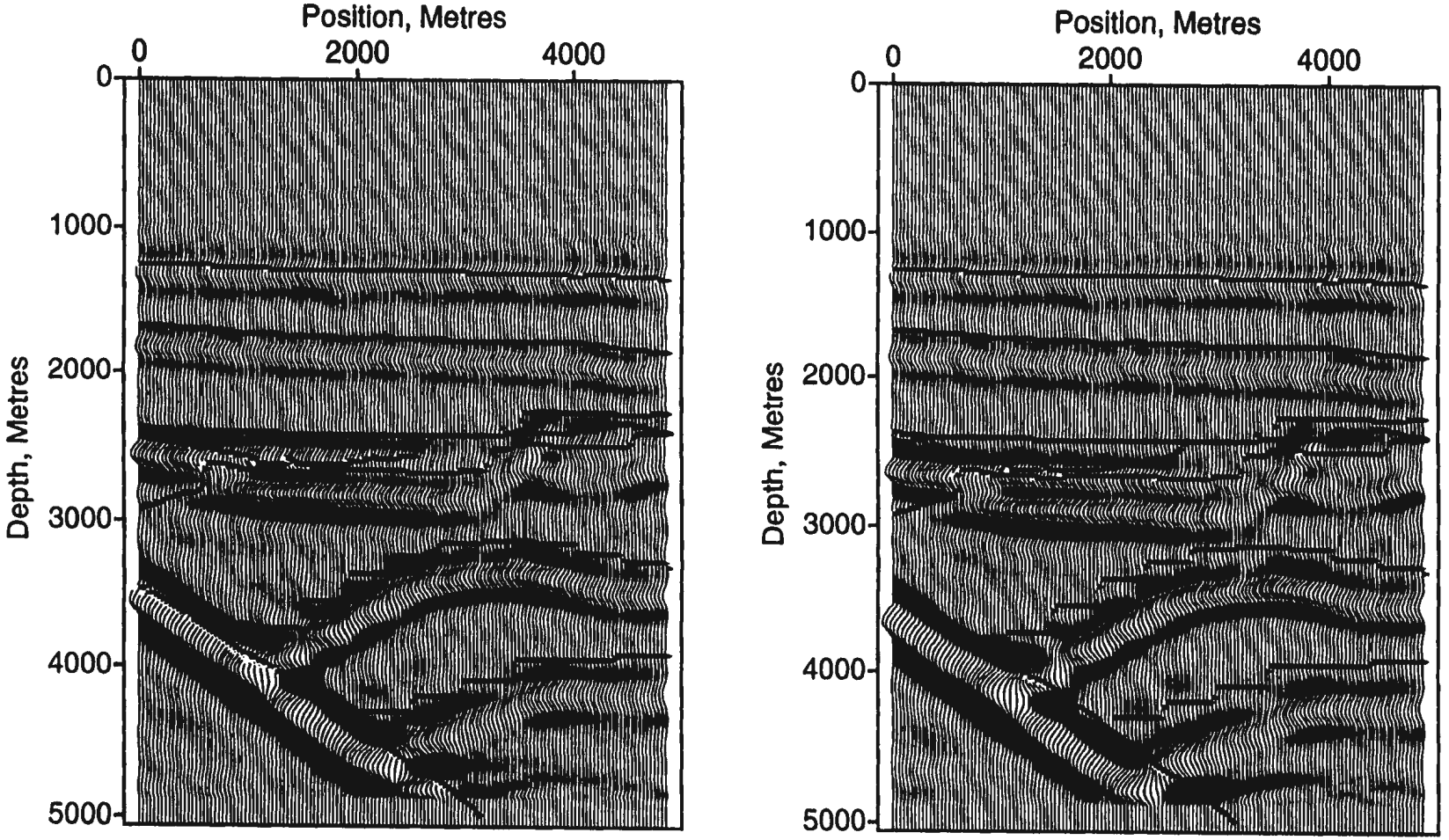

(c) (d)

Figure 4.2(c) is the result obtained from the 2-D reverse-time migration of crossline 30 with the v2 velocity model. The second layer has been placed at the correct depth, even though this model does not have the correct velocities. Figure 4.2(d) is the result of the 2-D reverse-time migration of crossline 30 using the v3 velocity model.

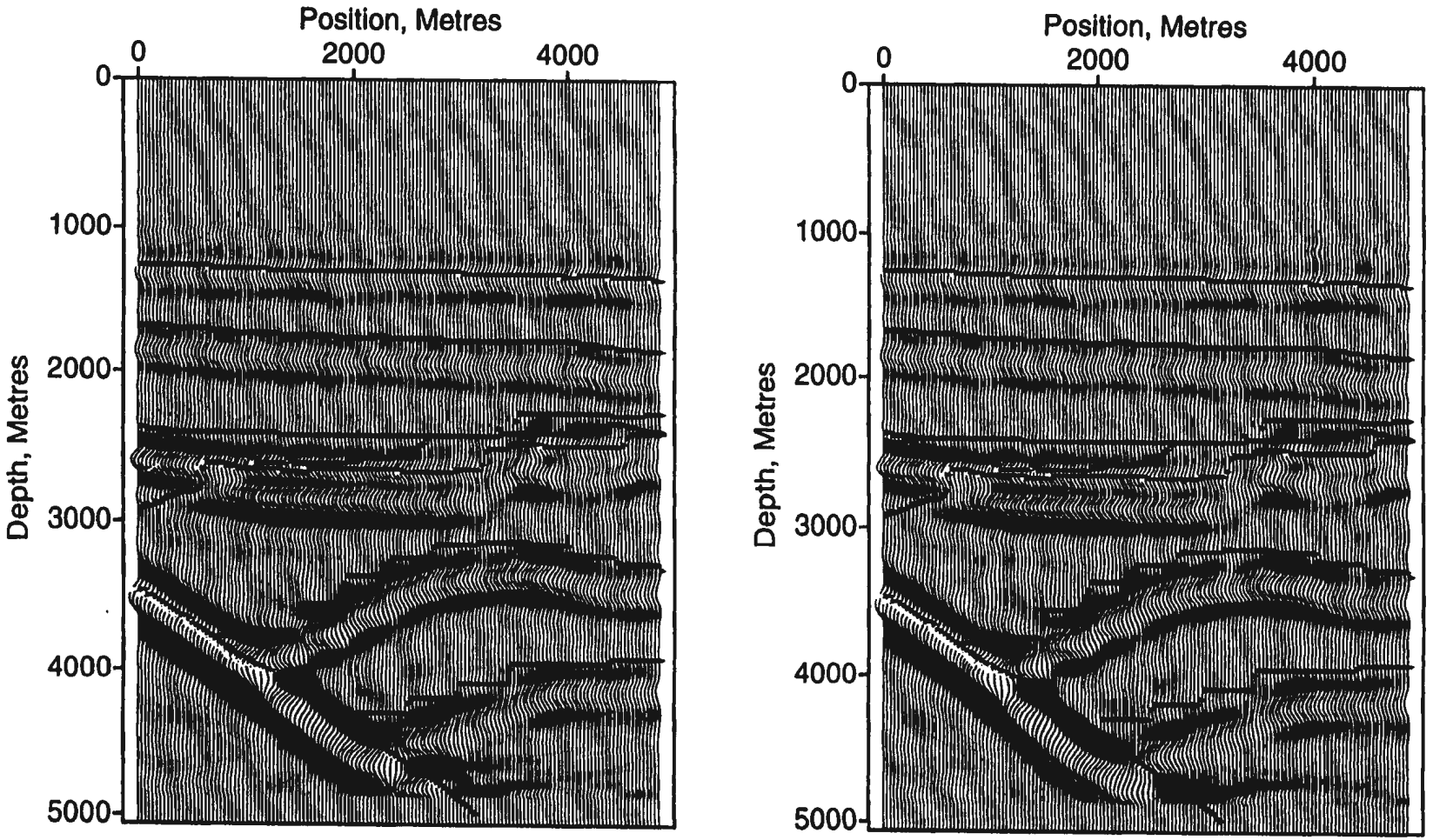

(e) (f)

Figure 4.2(e) is the result of the 2-D reverse-time migration of crossline 30 using the v4 velocity model. Figure 4.2(f) is the result of the 2-D reverse-time migration of crossline 30 using the v5 velocity model. These results demonstrate that an incorrect velocity model for the shallow layers may still produce accurate positioning of layers in the deeper parts of the model.

Table 4.4: Average fractional discrepancies for crossline 30

Velocity Model	Layer	No. of traces	Avg. fractional discrepancy
original	Base Tertiary	143	0.0504407
	Petrel	138	0.0343086
	Ekt3	145	0.0144015
	Catalina	104	0.0139937
	Hibernia	68	0.00721751
	Murre	82	0.0458778
Model v1	Base Tertiary	139	0.103686
	Petrel	145	0.0859698
	Ekt3	139	0.0517411
	Catalina	100	0.0448476
	Hibernia	75	0.0348512
	Murre	76	0.0708620
Model v2	Base Tertiary	142	0.112350
	Petrel	138	0.0212799
	Ekt3	155	0.00735648
	Catalina	109	0.0114237
	Hibernia	76	0.00536111
	Murre	87	0.0377870

Table 4.4: Average fractional discrepancies for crossline 30 (cont.)

Velocity model	Layer	No. of traces	Avg. fractional discrepancy
Model v3	Base Tertiary	146	0.113734
	Petrel	139	0.0180502
	Ekt3	145	0.0158416
	Catalina	98	0.0151164
	Hibernia	71	0.0150806
	Murre	74	0.0161764
Model v4	Base Tertiary	143	0.107806
	Petrel	137	0.0200376
	Ekt3	155	0.0143598
	Catalina	87	0.00786287
	Hibernia	72	0.00382156
	Murre	84	0.0395909
Model v5	Base Tertiary	147	0.109752
	Petrel	136	0.0165477
	Ekt3	147	0.0143912
	Catalina	96	0.0104516
	Hibernia	70	0.00806678
	Murre	85	0.0335816

4.2. Migration optimization based on well top information

Small errors in the velocity model (i.e., less than 5 per cent) input to a poststack migration algorithm will not severely affect the image quality, but will cause depth errors in the migrated section. A recent paper by Lines (1993b) proposes optimizing migration results by matching migration depths to formation tops at nearby well sites. Figure 4.3 visually outlines the flow of the migration optimization procedure. Layers are required to intersect the well in order to use this method in determining layer velocities, and the match between migrated depths and well tops is derived using an iterative least-squares method. The least squares technique is robust, and attempts to minimize the sum of the squared differences between the migrated depths and the N formation tops.

$$\begin{aligned} S &= \sum_{i=0}^{N} |d_i(V_j) - w_i|^2 \\ j &= 1, 2, \ldots, M \end{aligned} \tag{4.4}$$

Here, d_i is the depth of the migrated data, w_i is the ith well top, V_j is the velocity for the jth layer, and S is the quantity to be minimized by choice of velocity parameters. It is necessary to compute ΔV_j, so that

$$\begin{aligned} \frac{\partial S}{\partial \Delta V_j} &= 0 \\ j &= 1, 2, \ldots, M. \end{aligned} \tag{4.5}$$

for a model that contains M velocity layers.

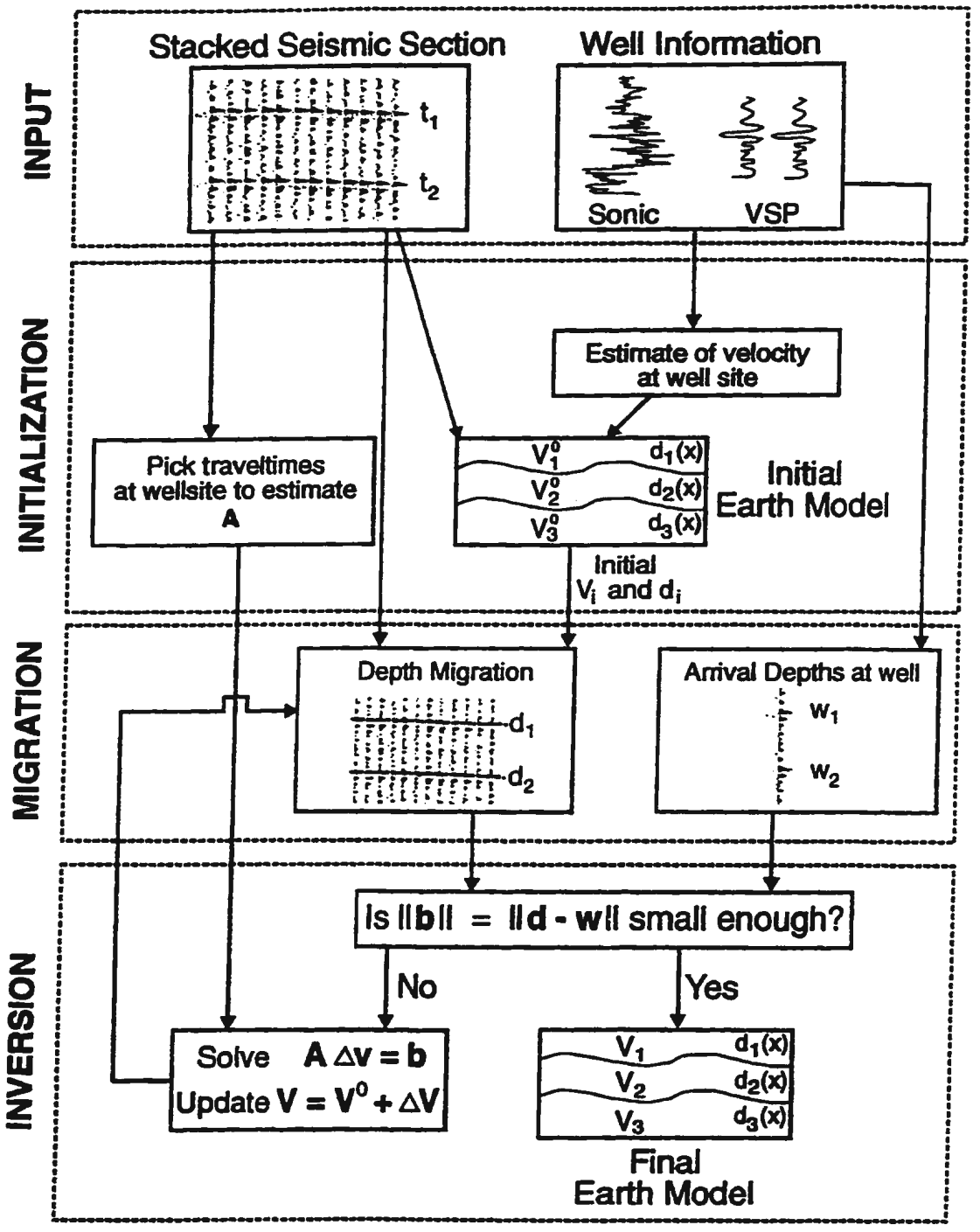

Figure 4.3 outlines the poststack migration optimization procedure. (figure taken from Lines, 1993b)

A procedure for determining a least-squares minimization of S is developed in Lines and Treitel (1984). and has the following form:

$$\underline{\underline{A}}\,\underline{x} = \underline{b} \tag{4.6}$$

$$x_i = \Delta V_i \quad .i = 0.2. \ldots . V \tag{4.7}$$

$$A_{i,j} = \frac{\partial d_i}{\partial V_j} = t_j \tag{4.8}$$

$$\underline{b} = \underline{w} - \underline{d} \tag{4.9}$$

$$d_i = \sum_{j=1}^{i} V_j t_j. \tag{4.10}$$

In the above equations. $\underline{x}$ is the parameter vector containing the velocity changes. $\underline{\underline{A}}$ is the Jacobian matrix. $\underline{b}$ is the discrepancy vector. t_j is the 1-way interval traveltime in the jth layer. $\underline{w}$ is the vector containing the well depths. and $\underline{d}$ is the vector containing the migration depths. The Jacobian values are obtained by picking the seismic traveltimes of the layers at the well location. with the accuracy of the Jacobian affecting the rate of convergence more so than the final result. Convergence is ultimately determined by the error term. $b^T b$. being sufficiently small in magnitude. The solution for the least-squares system in equation (4.6) is computed using the singular value decomposition method (SVD). which allows a sensitivity analysis to determine solution reliability (Jackson (1976) and Lines and Treitel (1985)).

4.2.1. Migration optimization of Hibernia model data

This poststack migration optimization procedure was initially tested on model data from both the three and seven layer Hibernia models. The v3 model from the velocity

error analysis of the three layer Hibernia model was used as a starting velocity model, and the trace at location 2900 was chosen as the well location for crossline 30. The migration with the correct velocity model was used to provide formation tops for the Petrel, Aan7, and Hibernia layers at the well location. The Jacobian was computed from the one-way traveltime differences between layers on the input seismic time section, and the values for the discrepancy vector, $\underline{b}$, were computed as the difference between the correct velocity migration depths and the v3 model migration depths. Four iterations of velocity sensitivity analysis and 2-D reverse-time migration were required to produce a velocity model that reasonably approximated the true velocity model for this line. The results of the various iterations are summarized in table 4.5, and the migration results are shown in figure 4.4 . The velocity model obtained through this procedure results in a reduced average absolute depth error of approximately 32 m for crossline 30. The total time required for this procedure is essentially the time needed to compute the four migrations, as the sensitivity analysis step is very fast.

The poststack optimization procedure was also applied to crossline 30 from the seven layer Hibernia model. The v5 velocity model was used as a starting velocity model, and the trace at location 2100 was used as the well location. The discrepancy vector was calculated for the Base of Tertiary, Petrel, Ekt3, Catalina, and Hibernia horizons for crossline 30. The optimization procedure for these lines was complicated by the fact that the v5 velocity model was deliberately created to produce a good match for the depth of the Petrel and Catalina horizons (see figure 4.2(f)). The

results of the various iterations are summarized in table 4.6. and the final migration results are shown in figure 4.5. The average depth error has been reduced from 71 m to 15 m .

Table 4.5: Poststack migration optimization results for crossline 30

Iteration	Layer	Depth discrepancy	True velocity	Optimization velocity
1	Petrel	-218.92 m	2221 m/s	2180 m/s
	Aan7	-231.29 m	3566 m/s	3336 m/s
	Hibernia	-393.12 m	4105 m/s	3868 m/s
2	Petrel	87.14 m	2221 m/s	2285 m/s
	Aan7	122.74 m	3566 m/s	3485 m/s
	Hibernia	240.36 m	4105 m/s	4189 m/s
3	Petrel	-29.38 m	2221 m/s	2250 m/s
	Aan7	-73.61 m	3566 m/s	3300 m/s
	Hibernia	-106.16 m	4105 m/s	4100 m/s
4	Petrel	-14.53 m	2221 m/s	2233 m/s
	Aan7	33.72 m	3566 m/s	3502 m/s
	Hibernia	48.12 m	4105 m/s	4139 m/s

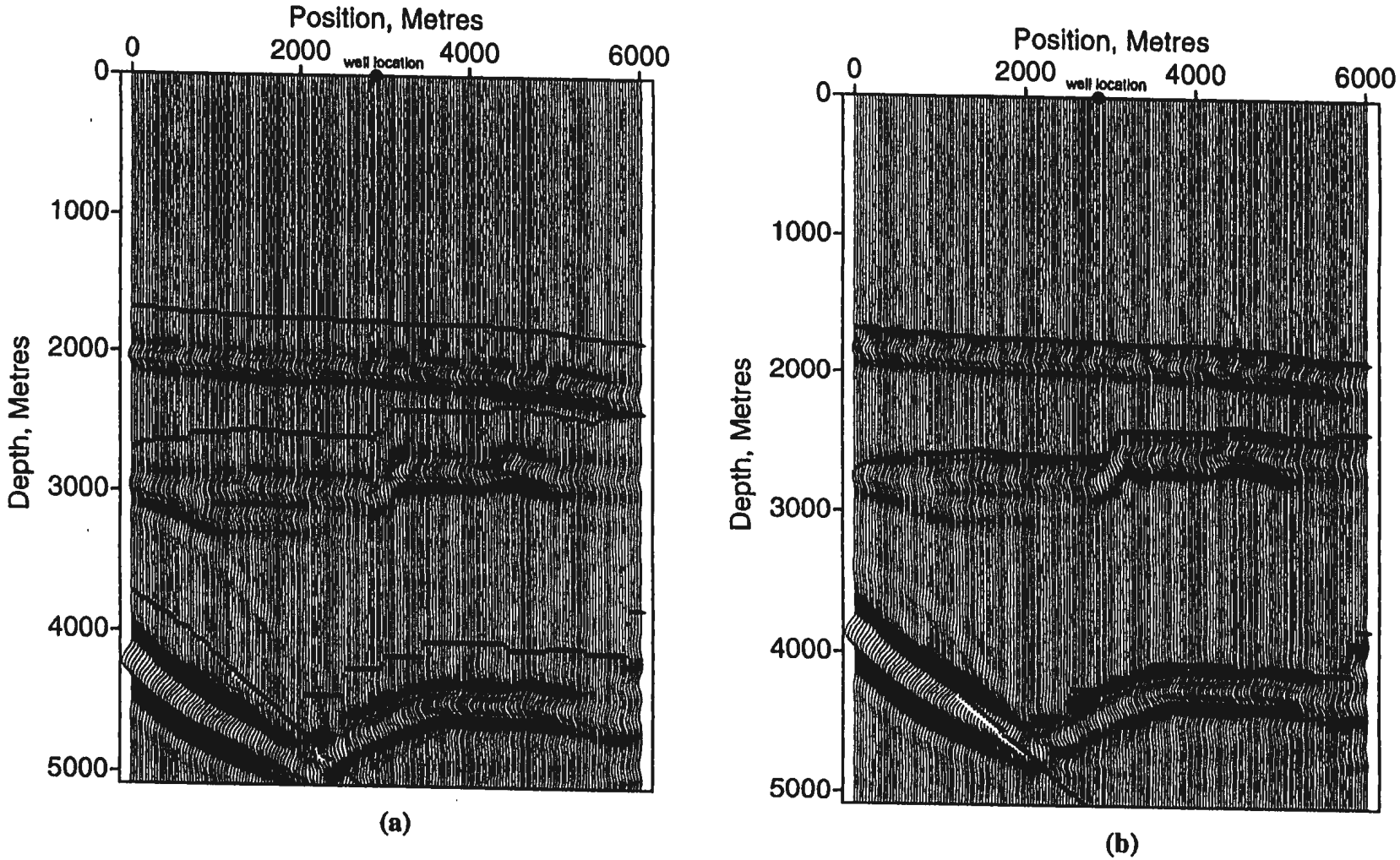

Figures 4.4(a) and (b) show, respectively, the migration result with the starting velocity model and the final migration result obtained with the optimized velocity model.

Table 4.6: Poststack migration optimization results for crossline 30

Iteration	Layer	Depth discrepancy	True velocity	Optimization velocity
1	Base Tertiary	87.19 m	2035 m/s	2061 m/s
	Petrel	-46.42 m	3009 m/s	3194 m/s
	Ekt3	-45.89 m	3548 m/s	3908 m/s
	Catalina	-77.95 m	4008 m/s	3543 m/s
	Hibernia	-97.06 m	4320 m/s	4437 m/s
2	Base Tertiary	-4.31 m	2035 m/s	2055 m/s
	Petrel	-69.71 m	3009 m/s	2784 m/s
	Ekt3	-59.83 m	3548 m/s	3981 m/s
	Catalina	-83.78 m	4008 m/s	3437 m/s
	Hibernia	-69.95 m	4320 m/s	4509 m/s
3	Base Tertiary	-25.41 m	2035 m/s	2018 m/s
	Petrel	42.59 m	3009 m/s	3211 m/s
	Ekt3	-3.68 m	3548 m/s	3638 m/s
	Catalina	42.96 m	4008 m/s	3645 m/s
	Hibernia	33.54 m	4320 m/s	4460 m/s
4	Base Tertiary	17.33 m	2035 m/s	2043 m/s
	Petrel	1.22 m	3009 m/s	3110 m/s
	Ekt3	-13.55 m	3548 m/s	3528 m/s
	Catalina	28.00 m	4008 m/s	3830 m/s
	Hibernia	15.57 m	4320 m/s	4396 m/s

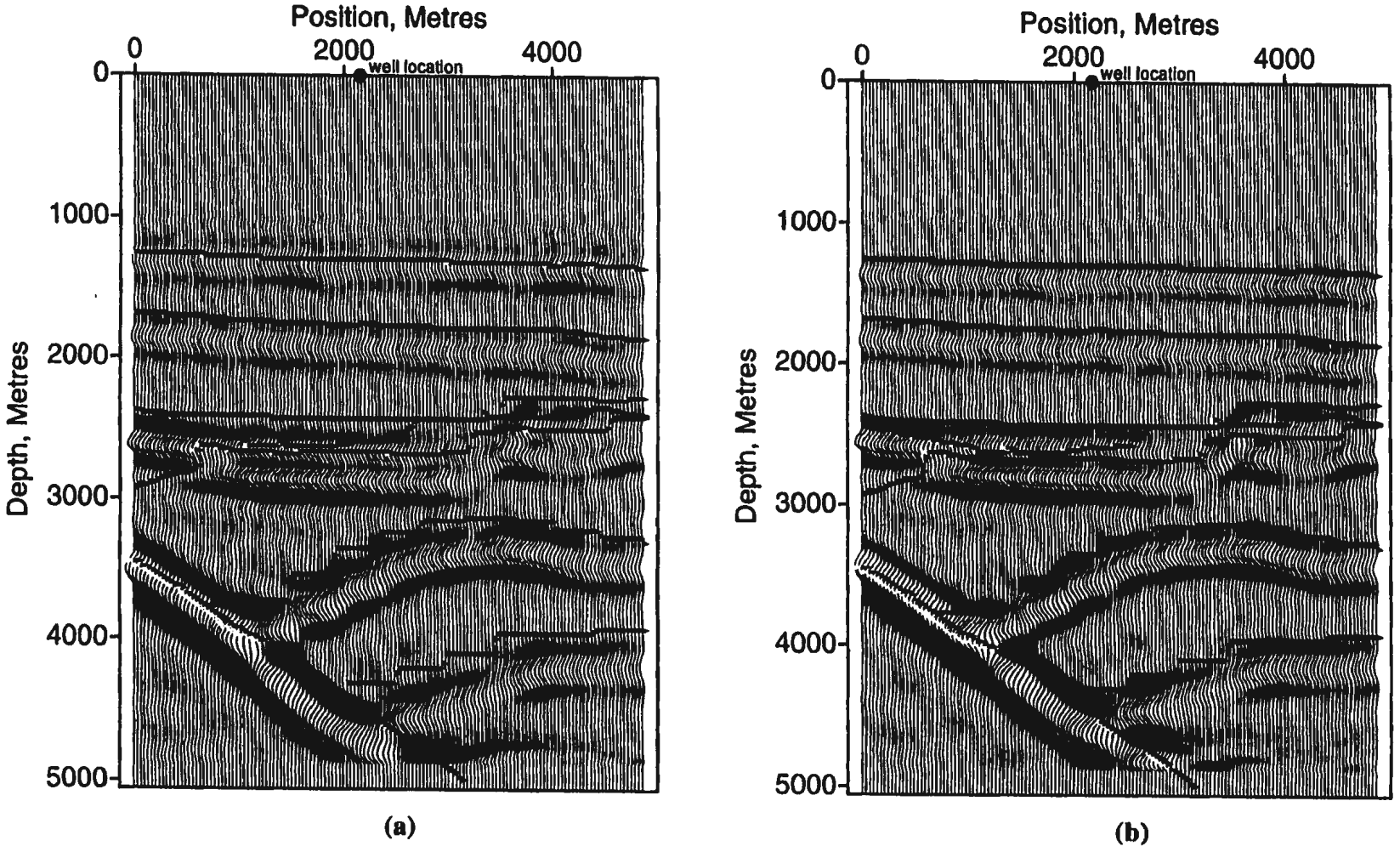

Figures 4.5(a) and (b) are, respectively, the migration obtained with the starting velocity model and the final migration obtained with the optimized velocity model. The average depth error has been reduced from 71 m to 15 m.

4.2.2. Optimization of Hibernia seismic data

Formation top information is available for various wells in the Hibernia field, and inline 1128, passing through well J-34 (figure 1.4), was chosen to test the migration optimization method. The layers used in calculating the discrepancy vector, $\underline{b}$, were chosen based on their presence as formation tops in the well, and the ease involved in identifying them as events on the seismic section. The Base of Tertiary unconformity, top of the Petrel Member, and top of the Avalon Formation were the formation tops used in the migration optimization of inline 1128. The formation tops for these horizons were obtained from the well information available from C-NOPB for the J-34 well. The average absolute depth error resulting from migration with the starting velocity model was 40 m. After four iterations of migration and velocity analysis, the average absolute depth error was reduced to 15 m. Figures 4.6(a) and (b) show the results of the initial migration and the optimized migration.

The updating of the velocity model in the outlined migration optimization method requires a least squares inversion step. In order to determine the reliability of this solution, it is useful to apply a sensitivity analysis which computes the solution which is barely acceptable for a particular error criterion. The change in the model parameters for this "edge" solution provides information on how much variability may occur in a given inversion solution. Jackson (1976) shows that edge solutions may be determined using SVD for the Jacobian matrix $\underline{\underline{A}}$. Jackson shows that variability about the original solution, $\underline{x}$, for a system with n data points is given by

$$\delta x = \frac{\sqrt{n[\sigma^2 - r^2]\nu_k}}{\lambda_k}. \qquad (4.11)$$

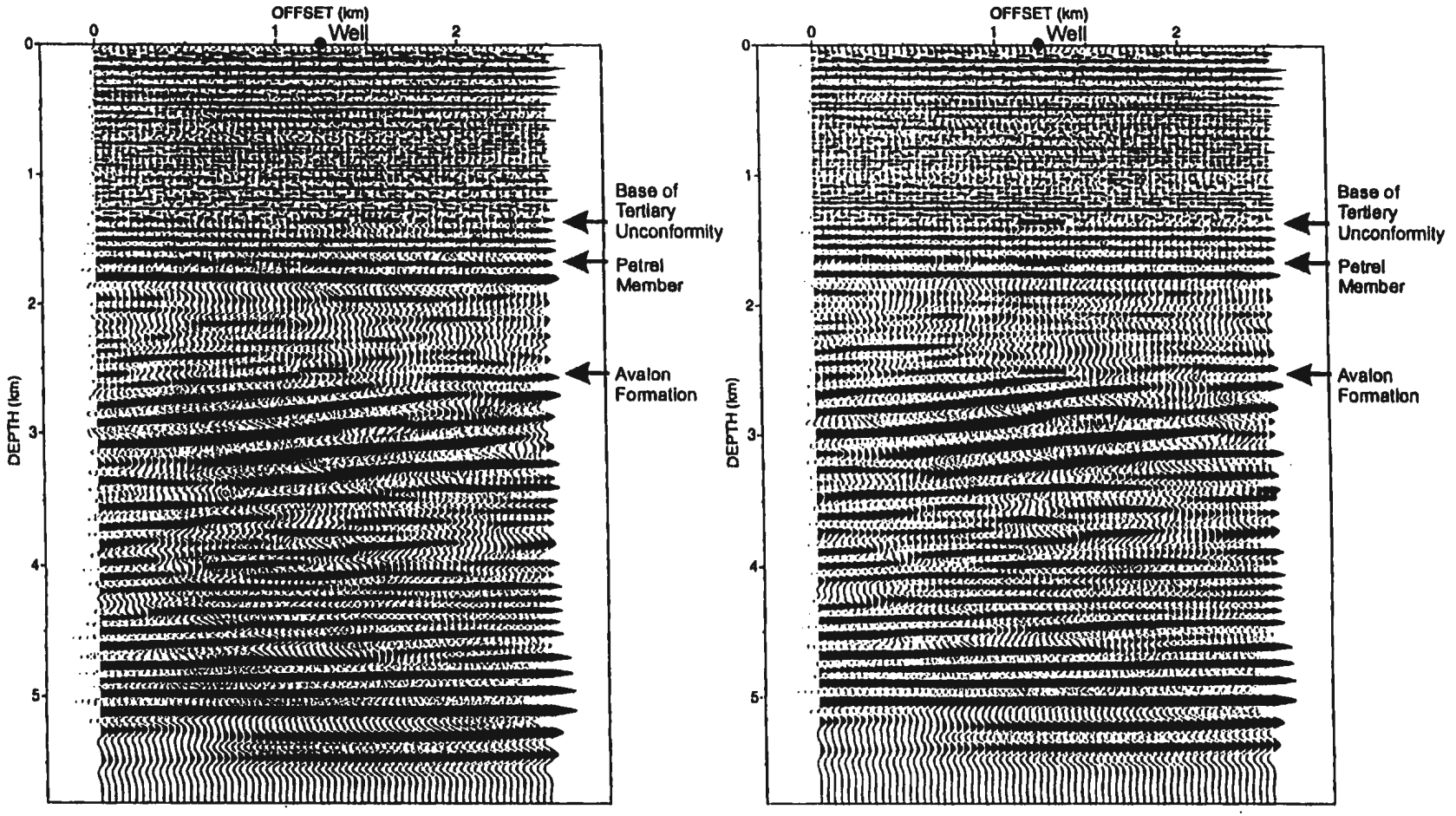

Figures 4.6(a) and (b) are the results, respectively, of the initial migration and the optimized migration of the Hibernia line which passes through the J-34 well. Four iterations of velocity inversion and migration have reduced the average depth misfit of the three well tops from 40 m to 15 m.

where r^2 is the mean squared error of the original solution. σ^2 is the mean squared error of the edge solution, λ_k is the singular value for the Jacobian matrix, and ν_k is the corresponding parameter eigenvector. The largest parameter variations are related to large relaxation of the mean squared error values and small singular values.

Sensitivity analysis of the inversion solution obtained for inline 30 from the three layer model shows that the mean squared error of the original inversion solution is 342 m^2. Assuming an average depth misfit of 25 m for each of the three layers means that a reasonable mean squared error is $\sigma^2 = 625\ m^2$. If these mean squared error values are used in equation 4.11 then edge solutions may be computed in the velocity analysis step. The edge solution for the smallest singular value results in a velocity model which produces the migration result in figure 4.7 . This migration looks visually acceptable, but the velocity in the second layer has an error of nearly 25 per cent from the true velocity. Table 4.7 compares the edge solution velocities to the actual velocities for this section. The large velocity error in the second layer has little result on the depth migration result since it is a thin layer. The Jacobian values depend on transit time, and therefore the amount of variability in the velocity parameter inversion estimates is dependent on the transit time through the layers.

Table 4.7: Edge solution velocity parameter results

Layer	Edge solution velocity	True velocity	Percentage error
1	2167 m/s	2221 m/s	2.4 per cent
2	4447 m/s	3566 m/s	24.7 per cent
3	4008 m/s	4105 m/s	2.4 per cent

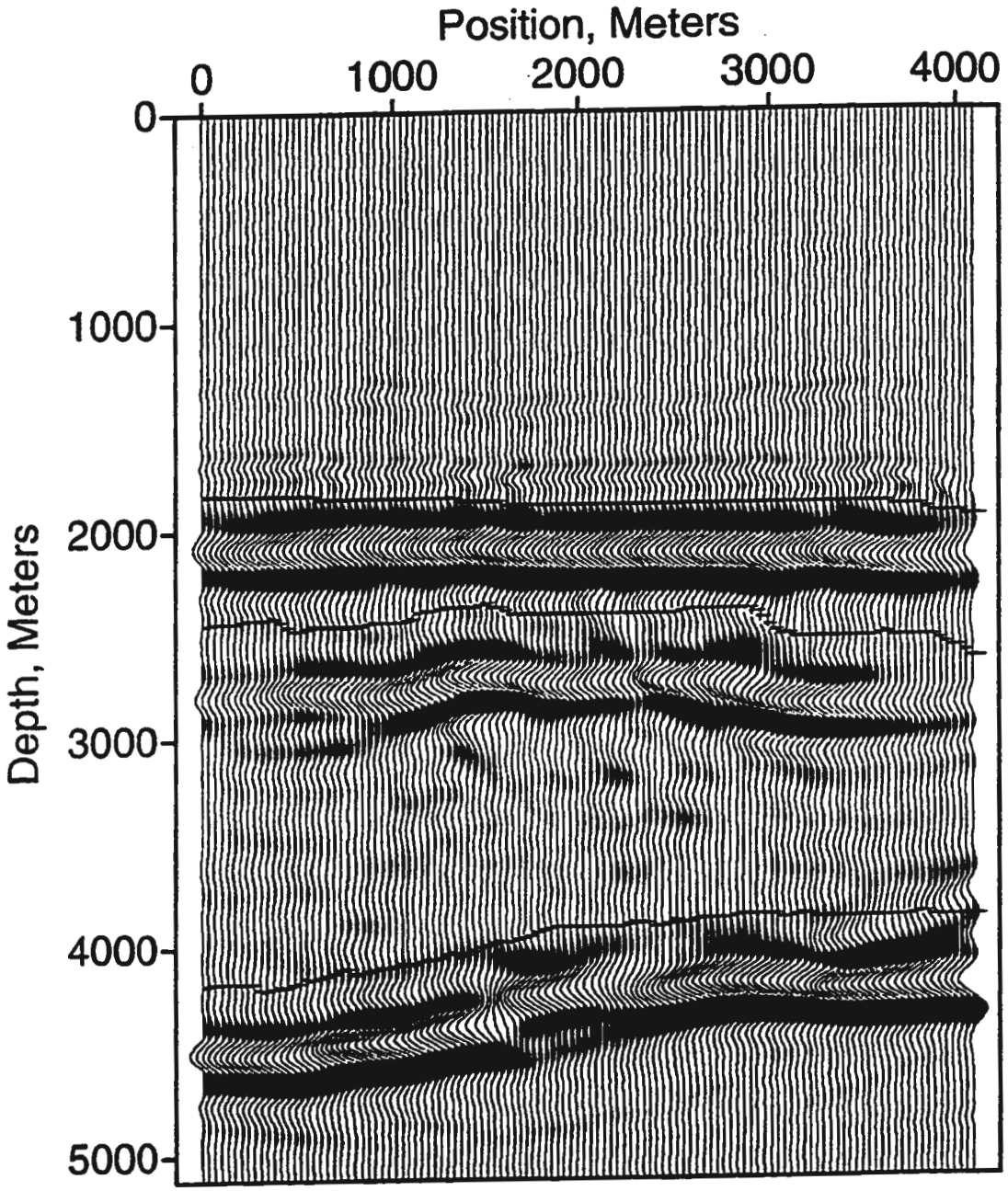

Figure 4.7(a) is the result of the edge solution migration of inline 30 from the first Hibernia model. The solution appears visually acceptable, but there is a velocity error of approximately 25 percent in the thinnest layer.

Chapter 5. Discussion and conclusions

5.1. Three-dimensional finite-difference modeling

Three-dimensional finite-difference modeling produces 3-D synthetic seismic data that may be used in studies of the imaging abilities of 2-D and 3-D poststack migration algorithms. The 3-D finite-difference modeling technique requires that the input velocity model satisfy numerical stability and dispersion criteria. These conditions are dependent upon the order of the finite-difference approximation and the minimum and maximum velocities present in the model. The spatial and temporal sampling intervals are chosen to satisfy the numerical stability and dispersion requirements, and this in turn controls the number of time steps and the total number of grid points. It is also necessary that boundary conditions be included in order to avoid reflections from the sides and base of the finite computer model.

The greatest drawback to the use of 3-D finite-difference modeling is the computer facility required to produce synthetic seismic data for models that have a large number of grid points in a reasonable amount of time. The cpu time required for 3-D finite-difference modeling is not prohibitive, but large arrays in each of the i, j, and k directions can slow down the computations so that the wall clock time may be several times greater than the cpu time. However, this problem may be solved in a variety of ways such as using a more powerful computer with a larger memory, or optimizing the finite-difference modeling algorithm to minimize the search required to find a

particular element within an array. The computation time and the total number of computations may also be reduced by using variable depth steps that would allow larger values of h_z at the deeper portions of the model where the velocities are generally larger than those near the surface (Jastram and Behle, 1992).

5.2. Analysis of poststack migration for Hibernia seismic data

Two-dimensional and three-dimensional poststack migration algorithms were compared on the basis of speed, accuracy, and amount of data preparation required prior to migration. The algorithms were tested using both synthetic seismic data and actual seismic data from the Hibernia oil field. The migrations of the model data showed that the two-dimensional Stolt migration was the fastest and required the least amount of work, but also resulted in the least accurate image. The two-dimensional reverse-time migration was the most accurate of all the 2-D algorithms, but required the most data preparation and the longest run time. The 3-D reverse-time migration algorithm required very large run times due to the small grid spacing required in order to satisfy stability and dispersion conditions. The results from the comparison of these migrations for both the model data in section 3.2, and the example of Wu et al. in section 3.3, showed that 3-D migration is necessary for some areas of the Hibernia field in order to accurately migrate out-of-plane reflection energy.

Three-dimensional poststack reverse-time migration is not currently in widespread use due to the need for a supercomputer in order to migrate a typical 3-D seismic dataset. The methods outlined in the previous section for reducing the computer

requirements and increasing the speed of 3-D finite-difference modeling also apply to 3-D reverse-time migration. In particular, using variable depth steps as described by Jastram and Behle (1992) would greatly reduce the run time for this migration technique.

It is also possible to optimize the results obtained with a two-dimensional post-stack migration algorithm using a least-squares inversion fitting of layer depths to formation tops. This technique requires that layers intersect the well and be easily identifiable on the seismic section. The number of well tops used in the inversion determines the number of layer velocities which may be used in the velocity model. In all tests of both model data and Hibernia seismic data, convergence to a very good solution has been obtained within four iterations. A measure of solution variability may be obtained by calculating the velocity model that would result for a particular depth misfit on all horizons used in the optimization.

References

Abramowitz, M. and Stegun, I.A., 1965. Handbook of mathematical functions. Eds., Dover, New York, New York, p.884.

Alford, R.M., Kelly, K.R., and Boore, D.M., 1974. Accuracy of finite-difference modeling of the acoustic wave equation. Geophysics, 39, 834-842.

Baysal, E., 1982. Modeling and migration by the Fourier transform method. Ph.D. thesis, University of Houston.

Baysal, E., Kosloff, D.D., and Sherwood, W.C., 1983. Reverse time migration. Geophysics, 48, 1514-1524.

Bell, J.S. and Campbell, G.R., 1990. Geology of the continental margin of eastern Canada, in Geology of Canada, No. 2, edited by M.J. Keen and G.L. Williams, 693-704, Geological Society of Canada, Ottawa, Canada.

Benteau, R.I. and Sheppard, M.G., 1982, Hibernia: a petrophysical and geological review, Journal of Canadian Petroleum Technology, 21, 59-72.

Bickel, S.H., 1990. Velocity-depth ambiguity of reflection traveltimes. Geophysics, 55, 266-276.

Bording, R. P., 1995. Wave equation difference engine. Ph.D. thesis, University of Tulsa.

Chang, W.F. and McMechan, G.A., 1989, 3-D acoustic reverse-time migration, Geophysical Prospecting, 37, 243-256.

Chun, J.H. and Jacewitz, C.A., 1980. Fundamentals of frequency domain migration. Geophysics, 46, 717-733.

Claerbout, J.F., 1985. Imaging the earth's interior. Blackwell Scientific Publications, Boston, p.2.

Clayton, R. and Enquist, B., 1977. Absorbing boundary conditions for acoustic and elastic wave equations. Bulletin of the Seismological Society of America, 67, 1529-1540.

C-NOPB (Canada-Newfoundland Offshore Petroleum Board), 1992. Poster Display in Earth Science Building, Memorial University, St. John's, Newfoundland.

Creaney, S. and Allison, B.H., 1987. An organic geochemical model of oil generation in the Avalon/Flemish Pass sub-basins, east coast Canada. Bulletin of Canadian Petroleum Geology, 35, 12-23.

Dablain, M.A., 1986, The application of high-order differencing to the scalar wave equation, Geophysics, 51, 54-66.

French, W.S., 1974, Two-dimensional and three-dimensional migration of model- experiment reflection profiles, Geophysics, 39, 265-277.

Gardner, G.H.F., McDonald, J.A., Watson, T.H., and Kotcher, J.S., 1978, An innovative 3-D marine seismic survey: Presented at the 40th Ann. Eur. Assoc. Explor. Geophys. Mtg.

Gazdag, J., 1978, Wave equation migration with the phase-shift method, Geophysics, 43, 1342-1351.

Gibson, B., Larner, K., and Levin, S., 1983, Efficient 3-D migration in two steps, Geophysical Prospecting, 31, 1-33.

Harris, C.E. and McMechan, G.A., 1992, Using downward continuation to reduce memory requirements in reverse-time migration, Geophysics, 57, 848-853.

Hubral, P., 1977, Time migration - Some ray theoretical aspects, Geophysical Prospecting, 25, 738-745.

Hurley, T.J., Kreisa, R.D., Taylor, G.G., and Yates, W.R.L., 1992, The reservoir geology and geophysics of the Hibernia field, offshore Newfoundland, in Giant oil and gas fields of the decade, AAPG Memoir 54, edited by Michael T. Halbouty, 35-54.

Jackson, D.D., 1976, Most squares inversion, Journal of Geophysical Research, 81, 1027-1030.

Jakubowicz, H. and Levin, S., 1983, A simple exact method of 3-D migration - theory, Geophysical prospecting, 31, 34-56.

Jastram, C. and Behle, A., 1992, Acoustic modeling on a grid of vertically varying spacing, Geophysical Prospecting, 40, 157-170.

Judson, D. R., Lin, J., Schultz, P.S., and Sherwood, J.W.C., 1980, Depth migration after stack, Geophysics, 45, 361-375.

Kelly, K.R., Alford, R.M.,and Whitmore, N.D., 1982, Modeling - The forward method, in Concepts and Techniques in oil and gas exploration, edited by Kamal C. Jain and Rui J. P. deFigueiredo, SEG publication, Tulsa, p.91-114.

Keys, R. G., 1985, Absorbing boundary conditions for acoustic media, Geophysics, 892-902.

Levin, S.A., 1984, Principles of reverse-time migration, Geophysics, 49, 581-583.

Lines, L.R. and Treitel, S., 1984, Tutorial: a review of least-squares inversion and its application to geophysical problems, Geophysical Prospecting, 32, 159-186.

Lines, L.R. and Treitel, S., 1985, Inversion with a grain of salt, Geophysics, 50, 99-109.

Lines, L., 1993a, Ambiguity in analysis of velocity and depth, Geophysics, 58, 596-597.

Lines, L., 1993b, Optimization of seismic migration through the use of well information, Canadian Journal of Exploration Geophysics, 29, 419-428.

Lines, L., Lu, H.X., Wu, W.J., and Langdon, G., 1995, Seismic depth migrations of eastern Canadian offshore data, The Leading Edge, 14, 42-48.

Loewenthal, D., Lu, L., Roberson, R., and Sherwood, J., 1976, The wave equation applied to migration, Geophysical Prospecting, 24, 380-399.

McMechan, G.A., 1983, Migration by extrapolation of time-dependent boundary values, Geophysical Prospecting, 31, 413-420.

Mitchell, A.R., 1969, Computational methods in partial differential equations, New York, John Wiley and Sons, p.34.

Mufti, I.R. and Fou, J., 1989, Interpretation of complex structure by 3-D seismic modeling, The Leading Edge, 8, 20-26.

Mufti, I.R., 1990, Large-scale 3-D seismic models and their interpretive significance, Geophysics, 55, 1166-1182.

Mufti, I.R., Pita, J.A., and Huntley, R.W., 1996, Finite-difference depth migration of exploration scale 3-D seismic data, Geophysics, 61, 776-794.

Myczkowski, J., McCowan, D., and Mufti, I.R., 1991, Finite-difference seismic modeling in real time, The Leading Edge, 10, 49-52.

Reynolds, A. C., 1978, Boundary conditions for the numerical solution of wave propagation problems, Geophysics, 43, 1099-1110.

Robinson, E.A. and Treitel, S., 1980, Geophysical signal analysis, Prentice-Hall, Inc., Toronto.

Sinclair, I. K., 1994, Tectonism and sedimentation in the Jeanne d'Arc basin, Grand Banks of Newfoundland, Ph.D. thesis, University of Aberdeen.

Stolt, R.H., 1978, Migration by Fourier transform, Geophysics, 43, 23-48.

Tankard, A.J. and Welsink, H.J., 1987, Extensional tectonics and stratigraphy of Hibernia oil field, Grand Banks, Newfoundland, AAPG Bulletin, 71, 1210-1232.

Versteeg, R.J., 1995, Limits on depth estimation accuracy, in Seismic depth estima-

tion, Proceedings of the 1995 Spring Symposium of the Geophysical Society of Tulsa. edited by W.S. Harlan. 117-121.

von der Dick, H. and Meloche. J.D.. 1986. Generation. migration. and expulsion of hydrocarbons in the Hibernia field. 1986 CSPG Convention Programs and Abstracts. p.38.

Whitmore. N.D.. 1983. Iterative depth migration by backward time propagation: 53rd Ann. Internat. Mtg.. Soc. Expl. Geophys. Expanded Abstracts. 382-385.

Whitmore. N.D.. Gray, S.H.. and Gersztenkorn. A.. 1988. Two-dimensional post-stack depth migration: a survey of methods. First Break. 6. 189-197.

Wu. W.J.. Lines. L.R.. Lu. H.X.. 1996, Analysis of higher-order finite- difference schemes in 3-D reverse-time migration. Geophysics. 61. 845-856.

Yilmaz. Ozdogan. 1988. Seismic data processing. Investigations in Geophysics series. No.2. edited by Stephen M. Doherty. SEG publication. Tulsa.

Appendix A: Derivation of finite-difference relations

The 3-D acoustic wave equation may be written as follows:

$$\frac{\partial^2 u}{\partial x^2} + \frac{\partial^2 u}{\partial y^2} + \frac{\partial^2 u}{\partial z^2} = \frac{1}{v(x,y,z)^2}\frac{\partial^2 u}{\partial t^2} \tag{A-1}$$

The terms $\frac{\partial^2 u}{\partial x^2}$, $\frac{\partial^2 u}{\partial y^2}$, $\frac{\partial^2 u}{\partial z^2}$, and $\frac{\partial^2 u}{\partial t^2}$ are second-order partial derivatives of u with respect to x, y, z, and t, respectively. The term $\frac{\partial^2 u}{\partial x^2}$ may be expressed using Taylor's series which are accurate to a certain order. Neglecting terms higher than fourth-order, one may use the following relations to determine an expression for $\frac{\partial^2 u}{\partial x^2}$ (Wu et al., 1996).

$$u(h) = u(0) + u'(0)h + \frac{u''(0)h^2}{2!} + \frac{u'''(0)h^3}{3!} + \frac{u^4(0)h^4}{4!} + \ldots \tag{A-2}$$

$$u(-h) = u(0) - u'(0)h + \frac{u''(0)h^2}{2!} - \frac{u'''(0)h^3}{3!} + \frac{u^4(0)h^4}{4!} + \ldots \tag{A-3}$$

$$u(2h) = u(0) + 2u'(0)h + 2u''(0)h^2 + \frac{8u'''(0)h^3}{6} + \frac{16u^4(0)h^4}{24} + \ldots \tag{A-4}$$

$$u(-2h) = u(0) - 2u'(0)h + 2u''(0)h^2 - \frac{8u'''(0)h^3}{6} + \frac{16u^4(0)h^4}{24} + \ldots \tag{A-5}$$

Adding equations (A-2) and (A-3) produces (A-6):

$$u(h) + u(-h) = 2u(0) + u''(0)h^2 + \frac{u^4(0)h^4}{12} \tag{A-6}$$

Adding equations (A-4) and (A-5) produces (A-7):

$$u(2h) + u(-2h) = 2u(0) + 4u''(0)h^2 + \frac{4u^4(0)h^4}{3} \qquad \text{(A-7)}$$

Multiplying (A-6) by 16 and subtracting (A-7) in the following manner produces an expression which may be solved for $u''(0)$.

$$16[u(h) + u(-h)] - [u(2h) + u(-2h)] = 30u(0) + 12u''(0)h^2 \qquad \text{(A-8)}$$

Therefore,

$$u''(0) = \frac{1}{12h^2}[16[u(h) + u(-h)] - [u(2h) + u(-2h)] - 30u(0)] \qquad \text{(A-9)}$$

Here h is defined to be the grid spacing in the x-direction, and $u(0)$ is the value of the function $u(x, y, z)$ at grid point i, j, k, where:

$$\begin{aligned} x &= (i-1)h \qquad & i &= 1, \ldots, I \\ y &= (j-1)h \qquad & j &= 1, \ldots, J \\ z &= (k-1)h \qquad & k &= 1, \ldots, K \\ t &= (n-1)\Delta t \qquad & n &= 1, \ldots, N. \end{aligned} \qquad \text{(A-10)}$$

In practice, the values of i, j, and k must allow for the need to use values of u that are two grid points away in all directions for the calculation of $u(i, j, k)$. Hence, $3 \le i \le I-2$, $3 \le j \le J-2$, $3 \le k \le K-2$. Therefore,

$$\frac{\partial^2 u}{\partial x^2} = \frac{1}{12h^2}\left[16(u^n_{i+1,j,k} + u^n_{i-1,j,k}) - (u^n_{i+2,j,k} + u^n_{i-2,j,k}) - 30u^n_{i,j,k}\right] \qquad \text{(A-11)}$$

Expressions for $\frac{\partial^2 u}{\partial y^2}$ and $\frac{\partial^2 u}{\partial z^2}$ may be obtained in a manner similar to that used for $\frac{\partial^2 u}{\partial x^2}$.

$$\frac{\partial^2 u}{\partial y^2} = \frac{1}{12h^2}\left[16(u^n_{i,j+1,k} + u^n_{i,j-1,k}) - (u^n_{i,j+2,k} + u^n_{i,j-2,k}) - 30u^n_{i,j,k}\right] \qquad \text{(A-12)}$$

$$\frac{\partial^2 u}{\partial z^2} = \frac{1}{12h^2}\left[16(u^n_{i,j,k+1} + u^n_{i,j,k-1}) - (u^n_{i,j,k+2} + u^n_{i,j,k-2}) - 30u^n_{i,j,k}\right] \qquad \text{(A-13)}$$

This method has assumed that the grid spacing is equal in the x-, y-, and z-directions. It is now necessary to determine an expression for $\frac{\partial^2 u}{\partial t^2}$ by considering the derivation of a second-order Taylor expansion for $u(t)$.

$$u(t) = u(0) + u'(0)t + \frac{u''(0)t^2}{2} + \ldots \qquad \text{(A-14)}$$

$$u(t + \Delta t) = u(0) + u'(0)(t + \Delta t) + \frac{u''(0)(t + \Delta t)^2}{2} + \ldots \qquad \text{(A-15)}$$

$$u(t - \Delta t) = u(0) + u'(0)(t - \Delta t) + \frac{u''(0)(t - \Delta t)^2}{2} + \ldots \qquad \text{(A-16)}$$

Adding equations (A-15) and (A-16) together, and simplifying the resulting equation, produces:

$$u(t+\Delta t)+u(t-\Delta t)=2u(0)+2u'(0)t+u''(0)t^2+u''(0)\Delta t^2 \qquad \text{(A-17)}$$

Substituting (A-14) into (A-17) results in (A-18):

$$u(t+\Delta t)+u(t-\Delta t)=2u(t)+u''(0)\Delta t^2 \qquad \text{(A-18)}$$

Taking Δt to be the temporal sampling rate and $u''(0)$ to be the value of $\frac{\partial^2 u}{\partial t^2}$ at the point (i,j,k) and time t produces this expression for $\frac{\partial^2 u}{\partial t^2}$.

$$\frac{\partial^2 u}{\partial t^2}=\frac{1}{\Delta t^2}\left(u^{n+1}_{i,j,k}+u^{n-1}_{i,j,k}-2u^{n}_{i,j,k}\right) \qquad \text{(A-19)}$$

Substituting the expressions for the second-order partial derivatives into equation (A-1), and solving for $u^{n+1}_{i,j,k}$, creates equation (2-3) from chapter 2.

$$\begin{aligned} u^{n+1}_{i,j,k} \;=\; & \frac{v(i,j,k)^2\Delta t^2}{12h^2}\Big[16(u^{n}_{i+1,j,k}+u^{n}_{i,j+1,k}+u^{n}_{i,j,k+1}+u^{n}_{i-1,j,k}+u^{n}_{i,j-1,k} \qquad \text{(A-20)}\\ & +u^{n}_{i,j,k-1}-(u^{n}_{i+2,j,k}+u^{n}_{i,j+2,k}+u^{n}_{i,j,k+2}+u^{n}_{i-2,j,k}+u^{n}_{i,j-2,k}+u^{n}_{i,j,k-2})\\ & -90u^{n}_{i,j,k}\Big]-u^{n-1}_{i,j,k}+2u^{n}_{i,j,k} \end{aligned}$$

If the x and y spacing is taken to be h_x and the z spacing is taken to be h_z, then equations (A-11), (A-12), (A-13), and (A-20) may be rewritten as:

$$\frac{\partial^2 u}{\partial x^2}=\frac{1}{12h_x^2}\left[16(u^{n}_{i+1,j,k}+u^{n}_{i-1,j,k})-(u^{n}_{i+2,j,k}+u^{n}_{i-2,j,k})-30u^{n}_{i,j,k}\right] \qquad \text{(A-21)}$$

$$\frac{\partial^2 u}{\partial y^2} = \frac{1}{12h_x^2}\left[16(u^n_{i,j+1,k} + u^n_{i,j-1,k}) - (u^n_{i,j+2,k} + u^n_{i,j-2,k}) - 30u^n_{i,j,k}\right] \qquad \text{(A-22)}$$

$$\frac{\partial^2 u}{\partial z^2} = \frac{1}{12h_z^2}\left[16(u^n_{i,j,k+1} + u^n_{i,j,k-1}) - (u^n_{i,j,k+2} + u^n_{i,j,k-2}) - 30u^n_{i,j,k}\right] \qquad \text{(A-23)}$$

$$\begin{aligned} u^{n+1}_{i,j,k} \;=\; & \frac{v(i,j,k)^2\Delta t^2}{12h_x^2}\left[16(u^n_{i+1,j,k} + u^n_{i-1,j,k}) - (u^n_{i+2,j,k} + u^n_{i-2,j,k}) + \right. \qquad \text{(A-24)} \\ & 16(u^n_{i,j+1,k} + u^n_{i,j-1,k}) - (u^n_{i,j+2,k} + u^n_{i,j-2,k}) + \frac{16}{R^2}\left(u^n_{i,j,k+1} + u^n_{i,j,k-1}\right) - \\ & \left.(u^n_{i,j,k+2} + u^n_{i,j,k-2})\right] + \left[2 - \left(\frac{v(i,j,k)^2\Delta t^2}{12h_x^2}\left(60 + \frac{30}{R^2}\right)\right)\right] u^n_{i,j,k} - u^{n-1}_{i,j,k} \end{aligned}$$

where $R = \frac{h_z}{h_x}$. Equation (A-24) will calculate future values of the wavefield for a model which has a different grid spacing in the horizontal plane than in the vertical plane.